Urban Area Monitoring and Intraurban Change Detection using SAR Data

Meiqin Che

Advisor: Prof. Paolo Gamba
Department of Electrical, Computer and Biomedical Engineering
University of Pavia

A thesis submitted for the degree of
Doctor of Philosophy

Pavia, September 2019

Abstract

Most human activities are concentrated in urban areas, which cover a small portion of the Earth's surface, but cause planetary-scale issues, such as air and water pollution, land degradation, and heat island phenomena. The increasing availability of fine temporal and spatial resolution SAR (Synthetic Aperture Radar) sensors on board of Earth Observation (EO) satellites provides a new perspective in investigation and monitoring of global and regional human activities. Thanks to the principle of radar imaging and its inherent characteristics, e.g., double-bounce scattering, SAR directly enables to retrieve the urban structure in the horizontal and vertical dimensions. Additionally, the utilization of SAR polarimetry makes it possible to separate mixed backscattering echoes. Finally, exploiting Interferometric SAR (InSAR) technology, more 3D information can be extracted and considered.

In this scenario, although many approaches have been developed to detect urban changes in single-polarization SAR data, few researches have focused on urban change detection using multi-polarization SAR sdata. Moreover, many of the approaches in technical literature map urban extent expansion or intra-urban change locations, but without exploring, in the latter case, detailed change characteristics in terms of their spatial and/or temporal patterns. In this thesis, new approaches are developed to automatically map and explore intra-urban changes using fully polarimetric SAR (Quad-PolSAR), Dual-polarimetric SAR (Dual-PolSAR), as well as temporal sequences of SAR data, even in conjunction with multispectral data. More specifically, this thesis reports about the methods listed as follows.

1. A superpixel-based multi-pattern change detection technique that uses SAR polarimetry. Quad-PolSAR (Radarsat-2) and Dual-PolSAR (Sentinel-1) data are used to map 2D/3D changes inside urban areas. The results confirm the possibility of an effective 2D/3D change detection with fully polarimetric SAR, but show poor performances using dual-polarization data.

2. A temporal change pattern extraction approach that uses coherence in multi-temporal Dual-PolSAR series. Sentinel-1 SAR complex data are used to detect changes in the temporal domain. Due to the weak contribution of polarimetry to change mapping, coherence temporal series are considered to investigate temporal multi-pattern intra-urban changes.
3. An intra-urban change vector analysis exploiting SAR and multispectral data. The use of SAR in conjunction with other optical sensors is a promising yet challenging technique, because of the different spatial resolutions and data modalities. A change vector analysis and visualization approach is proposed to automatically extract changes and enable an easier understanding of the intra-urban changes that are revealed.
4. A hierarchical bi-clustering algorithm for multiple-pattern change investigation. To address temporal pattern analysis in wide urban areas (e.g., megacities or urban clusters) a hierarchical bi-clustering method is introduced to address the unpredicted number of clusters and better discriminate among urban change patterns referring to new constructions, demolitions, and renovations.

All the approaches proposed in this thesis have been applied to monitor urbanization in both developing and developed countries, and have been validated by an extensive comparison with ground truth data in many different areas of the world. Specific focus has been given to the P.R. China and South East Asia, where urban areas are quickly evolving and intra-urban changes can be more easily spotted and recognized.

Acknowledgements

> *If we knew what we were doing, it wouldn't be called research, would it?*
> *Will climb inferiority, since, as too high to achieve success, and therefore the winners must develop equanimity of mind, always focused, this is the point of success*
> *A person must first go through difficulties, and then into the good times, it felt good enough, comfortable*

All the works included in this thesis is result of a persevere endeavor and steadfast faith. Finally I arrive at the top of this mountain, now I would like to take a break to write some testimonials for my PhD journey and thank the people who accompanied me.

Foremost, I would like to thank my supervisor, Prof. Paolo Gamba for faithfully and unconditionally supporting and advising me during the whole of my PhD research. I prettily appreciate your kindness to provided me with opportunities to participate international symposiums. Your knowledge and guidance were beneficial and important to me. I also would like to thank Prof. Fabio Dell'Acqua, Prof. Pietro Savazzi and Lorenzo Favalli for being members of my PhD commitee, Prof. Fabio Del Frate and Dr.Mattia Marconcini for reviewing my PhD thesis.

I would like to thank all the members in Telecommunication & Remote Sensing lab, Gianni, Zik, Daniele, Farzana for supporting my PhD work and life in Pavia.

Thanks to my master's tutor Prof. Du and Dr. Alim Samat for their recommend and help to me

Thank my friends, Hongyang, Chunhui, Zik, Pang ji, Yangyang, Haochen, Hengke, Luosu, Yina for accompanying me three happy years in pavia, also thanks to new friends Dr. Wang, Jinjin, Songrui, Youhua and Hanyang. And thanks to the friends in Munich, Zilu, and Chunping.

As this end of the place, I would like to thank my parent and brother for unconditional and unselfishly support on the other side of the Earth. It is them make the person I become today and who will be in future.

This thesis work has been partially supported by China Scholarship Council, here thanks to my homeland and government. At last let me sang a song at the end of my PhD journey:

Those linger about on the road
via via
Do you wanna go? via via
Fragile but still proud
I used to be just like that
Agitating and boiling ones
Where do you go? via via
Mysterious, so calm down
Are you listening to my story?

Over the rivers and mountains
been through people mountain people sea
everything I used to own
now is gone like smoke
I was lost and so helpless
and disoriented
till I got the answer right found this ordinary path

But you still fancy about
via via
your tomorrow, via via
Is she good? Could it be worse?
It’s just another day for me

I used to ruin my everything
to get away forever
I used to fall into the dark fog
I was struggling, hard to get out
I was like you like him like those wild grass and flowers
helplessly anticipating
cried and laughed being ordinary

moving on just like this, don’t care what you were given
moving on just like this, don’t care what was taken away
moving on just like this, don’t care what will be missing
moving on just like this, don’t care what will...

Over the rivers and mountains
been through people mountain people sea
I used to ask the whole world
but never got any answers
I’m just like you like him
like those wild grass and flowers
fate led me
to this only path I have to go on
Time has no words just let it be
via via
tomorrow is there, via via
Wind passed by it’s still far
Where did your story stop?

Contents

1 Monitoring urban areas using spaceborne remote sensing 1
- 1.1 Why urban remote sensing? . . . 1
- 1.2 Urban monitoring using spaceborne remote sensing imagery . . . 2
  - 1.2.1 Urban area monitoring and change detection using multispectral sensors . . . 2
  - 1.2.2 Urban area monitoring and change detection using radar sensors . . . 4
- 1.3 Challenges and objectives . . . 13
- 1.4 Dissertation organization . . . 14

2 Superpixel-based 2D/3D change detection using SAR polarimetry 16
- 2.1 Introduction . . . 16
- 2.2 Superpixel-wise change detection method for multi-temporal PolSAR images 17
  - 2.2.1 Adaptive distance measure in segmentation . . . 18
  - 2.2.2 Superpixel-wise dissimilarity description to multiple changes . . . 19
  - 2.2.3 Multiple-component change pattern detecting with GMM clustering 21
- 2.3 Experimental results . . . 22
  - 2.3.1 2D/3D change detection using Quad-PolSAR SAR . . . 22
  - 2.3.2 2D/3D change detection using Dual-PolSAR SAR . . . 29
- 2.4 Conclusions . . . 33

3 Urban change patterns using SAR time-series 36
- 3.1 Introduction . . . 36
- 3.2 Change pattern recognition from coherence and intensity series . . . 37
  - 3.2.1 Urban extent series extraction and analysis . . . 40
  - 3.2.2 Interferometric coherence time-series . . . 41
- 3.3 Experimental results . . . 42
  - 3.3.1 Case 1: Changsha, P.R.China . . . 42
  - 3.3.2 Case 2: Hangzhou, P.R.China . . . 48

3.3.3 Case 3: Lombardy Region, Italy 51
3.4 Conclusions 51

4 Multi-pattern change exploration using data from heterogeneous sources 55
4.1 Introduction 55
4.2 Multi-pattern change exploration using heterogeneous data 57
4.2.1 The overall processing chain 58
4.2.2 Change vector analysis: the Nanjing test case 59
4.2.2.1 Validating the Changes 61
4.2.2.2 Comparing the approach with previous techniques 62
4.3 Experimental results : Change detection using Sentinel-1 SAR and night-time lights 66
4.4 Conclusions 72

5 Change pattern exploration at the megacity/urban cluster level 73
5.1 Introduction 73
5.2 Change pattern exploration with hierarchical clustering 74
5.2.1 Hierarchical clustering 75
5.3 Experimental results 76
5.3.1 Case 1: Megalopolis in P.R.China 78
5.3.2 Case 2: Lombardy Region, Italy 80
5.3.3 Case 3: Nigeria and its coastal cities 86
5.4 Conclusions 91

6 Conclusion 92
6.1 Contributions and discussions 92
6.2 Future developments 94

A SAR polarimetry 96

Bibliography 98

List of Figures

1.1 The side-looking nature of SAR systems causes foreshorten, shadow, and layover effects on buildings . . . 6

2.1 Overall workflow of the proposed technique . . . 18
2.2 An example of superpixel and its statistical distribution at t_1, t_2. . . . 20
2.3 Pauli decomposition composite image on March 25, 2013, highlighting in red/blue/white the selected positive/negative change/no change areas in the ground truth. . . . 23
2.4 Pauli decomposition images after applying various de-speckle filters. . . . 24
2.5 The pixel-wise CDs and superpixel-wise CDs . . . 24
2.6 Examples of negative and positive changes . . . 25
2.7 Graphical comparison of the discriminative power of different dissimilarity descriptors in case of three-component changes . . . 26
2.8 Positive and negative changes in Nanjing central urban area, P.R. China, from 2008 to 2013 (positive changes in red, negative changes in blue, no change in white). . . . 28
2.9 ROC curves and AUC values as a function of superpixel scale L. . . . 30
2.10 A Sentinel-1 Dual-PolSAR composite image and manually collected ground truth for the city of Hefei (P.R. China). . . . 31
2.11 Urban extent of Hefei, P.R.China, extracted from S-1 data (in red) superimposed to an S-2 image of the same area. . . . 32
2.12 Hefei (P.R. China): change maps obtained using the dual-polarimetry α parameter without (a) or with (b) the use of a urban mask. . . . 33
2.13 ROC curves and AUC values using polarimetric parameters or temporal coherence: the first row refers to negative changes, the second row to positive changes. . . . 34

3.1 Workflow of the procedure described in this work . . . 38

3.2 Changsha test site: (a) S-1 June 2016 SAR false color image using VV, VH, VV/VH; (b) Optical image in the same period. 43

3.3 Temporal baselines (in days) and perpendicular baselines (in meters) for the S-1 sequence over Changsha, considering the image in Sept. 2017 as a refernce. 44

3.4 Changhsa test site: (a) urban core map; (b) areas that have become urban along the same timeline (the blue to red legend marks less to more recent changes). The area identified by a white rectangle is the one considered for further, more detailed analyses in the next figures. 44

3.5 The portion of the Changsha test site identified by a white rectangle in Fig. 3.4 45

3.6 The trend of the average coherence and backscattering amplitude coefficients for the patches A and B identified in Fig.3.5, to be checked against optical images for validation purposes. The two curves in red and blue refer to the two polarizations of S-1 data. 47

3.7 The trend of the average coherence and backscattering amplitude coefficients for patch C identified in Fig.3.5, to be checked against optical images for validation purposes. The two curves in red and blue refer to the two polarizations of S-1 data. 48

3.8 Hangzhou test site: (a) S-1 June 2016 SAR false color image using VV, VH, VV/VH; (b) Optical data image for the same period. 49

3.9 Hangzhou test site: the urban core area (on the left), a smaller area where clustering results are reported (on the right), inside which three patches (in blue, green and yellow) are identified. 50

3.10 The trend of the average coherence and backscattering amplitude coefficients for the three patches identified in Fig. 3.9 for the Hangzhou test site (the two curves in red and blue refer to the two polarizations of S-1 data). . 50

3.11 Lombardy region: (a) Sentinel-1 composite image; (b) Greater Milan urban area extent. 51

3.12 Time-series analyses of selected patch 1: (a) time-series analyses of backscattering σ_0, difference $\Delta\sigma_0$,coherence γ_c; (b) validation with Google Earth images at timelines marked in black. 52

3.13 Time-series analyses of selected patch 2: (a) time-series analyses of backscattering σ_0, difference $\Delta\sigma_0$,coherence γ_c; (b) validation with Google Earth images at timelines marked in black. 53

4.1 A graphical representation of the processing chain used to analyze the changes at the intra-urban level by combining nighttime lights and Sentinel-1 SAR data. 57
4.2 Intermediate and final results for the proposed processing chain applied to the city of Nanjing and considering the time interval between July 2015 and March 2018 60
4.3 A visual check of the changes/no changes in one selected location in Nanjing using very high-resolution images in 2015 and 2018 available in Google Earth Historical Imagery. 61
4.4 Results for the city of Nanjing, still considering the interval between July 2015 and March 2018, but using ASCAT data instead of S-1 data 63
4.5 Temporal analysis with a time step of one year for the Nanjing urban area using S-1 and nighttime light for volumetric analysis (left) and S-1 alone (at about 20 m spatial resolution) for urban extent growth (center row, changed areas appear in red). The top and bottom row display VHR images (from Google Earth) of two locations selected using the joint nighttime/S-1 clustering and whose different temporal change pattern is captured by the S-1 change maps. 64
4.6 Ground truths for the subregion identified by a rectangle in Fig. 4.2(c) . . . 65
4.7 Experimental results for the Greater Saigon test area: (a) clustering maps using S-1 and nighttime data; (b) two-dimensional change detection for urban extents at 10 m spatial resolution using S-1 urban extent maps in 2015 and 2018; (c) graphical representation of these clusters in the $\Delta\ NT, \Delta\sigma_0$ domain. 67
4.8 Visual analysis of the temporal evolution of the areas highlighted in Fig.4.7 for the Greater Saigon urban area, and corresponding to (top row) a volumetric change as opposed to (bottom row) a built-up area extension. 68

4.9 (a) Different changed pixels identified for the Greater Saigon urban area (see Fig. 4.7): in red changes at 10-m pixel spacing, recognized by comparing urban extents extracted from S-1 data, in green and purple changes at 500-m spatial resolution obtained by clustering the changes in nighttime lights and SAR backscatter coefficients and corresponding to volumetric and area extension changes, respectively (see Fig. 4.8), and finally in white pixels recognized as "unchanged." (b) Ground truth for the white, purple, and green classes, obtained by manually digitizing areas that experienced no change, volumetric changes, and urban extension changes, respectively. (c) Selection of 30 locations marked with red dots in (a) and checked for urban extent changes. 68

4.10 Clustering results for Shanghai, and visual assessment for the area highlighted by the yellow circle, an area that is picked as changed with respect to backscattering coefficient and nighttime light, but that in reality experienced a limited change in both the built-up extents and their volume. 69

4.11 Clustering results for Guangzhou (China) and Vientiane (Laos), with a few examples of temporal patterns that have been extracted and can be recognized. 71

5.1 Workflow of the urban change pattern exploration procedure used in this chapter. 75

5.2 Graphical representation of the hierarchical multi-scale unsupervised clustering. 76

5.3 Geolocation of the studied areas. 77

5.4 Beijing: (a) bi-dimensional scatterplots of the clusters extracted in the first layer of the hierarchical clustering procedure; (b) corresponding spatial extents of these two clusters. 78

5.5 Jingjinji: bi-dimensional scatterplots of the clusters extracted in the second layer of the hierarchical clustering procedure. 79

5.6 Vector analysis for 4-component clusters applied to the Jingjinji and Yangtze River Delta megalopolis: (a, c) plotting a subset of points; (b, d) plotting only cluster centers. 81

5.7 4-component clusters for multiple cities in the Jingjinji megalopolis. 82

5.8 Vector analysis for 8-component clusters for the Jingjinji and Yangtze River Delta megalopolis: (a, c) using a subset of points; (b, d) using only cluster centers. 83

5.9 The spatial location of changes inside and outside urban areas: (a) the 8-component clustering map of (a) the main urban area of Shanghai; (b) small settlements far from it in the island in Yangtze River Delta; (c) the main urban area of Beijing; (d) small settlements far it (the black patch inside the red rectangle is the construction site of Beijing Daxing International Airport). 84
5.10 Validating changes with Google Earth History Images:(a) Gogle Earth History Images of Beijing Daxing International Airport in Fig. 5.9d; (b) Google Earth History Images of the island in the Yangtze River Delta in Fig. 5.9b. . 85
5.11 The 8-components change pattern of the urban cluster in the Lombardy region of Italy 85
5.12 Vector analysis for 8-component clusters for Milan metropolitan area: (a) using a subset of points; (b) using only cluster centers. 87
5.13 The 8-components change patterns for coastal cities in Nigeria. 88
5.14 Google Earth images of selected patches in Nigeria 89
5.15 Vector analysis for 8-component clusters for cities in Nigeria: (a) using a subset of points; (b) using only cluster centers. 90

List of Tables

1.1 Polarimetric decomposition theories and descriptions 8

2.1 Superpixel Change Detection (SCD) via different dissimilarity measures at the superpixel level 21
2.2 Change detection results using different polarimetric parameters 27
2.3 Change detection results using the combination of multiple polarimetric parameters 29
2.4 Change detection results with and without the use of the urban mask for Hefei 32

3.1 The confusion matrix for the object-based validation of urban changes inside urban core of Changsha 46
3.2 The object-based validation on changes of growth over Changsha 46
3.3 The confusion matrix for the object-based validation of urban changes in Hangzhou. 48
3.4 The object-based validation on changes of growth over Hangzhou. 49

4.1 Confusion matrix for the validation of the results in the subregion identified by a rectangle in Fig.4.2(c) with respect to Fig. 4.6(b) 62
4.2 Confusion matrix for the validation of Fig. 4.9(a) with respect to Fig. 4.9(b) 70

5.1 the remotely sensed measurements (also called features) considered in this work 74
5.2 Interpretation of change patterns in the Yangtze River Delta 86
5.3 Interpretation of change patterns in the Jingjinji megalopolis 87
5.4 Quantitative validation indexes for the urban extents and the detected change clusters. 90

Chapter 1

Monitoring urban areas using spaceborne remote sensing

This chapter gives an overview of spaceborne urban remote sensing and its applications for change detection and monitoring using radar and multispectral sensors, especially focusing on intra-urban change detection and urban activities monitoring. It introduces the main motivations and objectives of this thesis and presents its structure and organization.

1.1 Why urban remote sensing?

Urbanization is one of the most concerned global change issues. It refers to planetary-scale changes on the surface of Earth. According to the ”World Urbanization Prospects 2018” report from the UN, until today, 55% of world population lives in urban areas, and this percentage will increase to 68% by 2050. Projections show that another 2.5 billion people will migrate from rural to urban areas by 2050.

It is noteworthy that nearly close to 90% of this increment is taking place in Asia and Africa. Future increments of the world urban population are expected to be highly concentrated in just a few countries (India, China and Nigeria) rather than in the most urbanized regions such as North America, with 82% of its population living in urban areas in 2018, Latin America and the Caribbean (81%), Europe (74%) and Oceania (68%). The level of urbanization in Asia is now approximating 50%. In contrast, Africa remains mostly rural, with 43% of its population living in urban areas. By 2050, it is projected that India will have added 416 million urban dwellers, China 255 million and Nigeria 189 million.

Further expansions of megacities like Tokyo, the largest city with an agglomeration of 37 million inhabitants, followed by New Delhi with 29 million, Shanghai with 26 million, and Mexico City and Sao Paulo, each with around 22 million inhabitants, bring challenges in meeting the needs for housing, transportation, employment, energy systems, microclimate management, and other environmental issues, as well as basic services such as education and health care.

In this context, sustainable urban policies to improve urban and surrounding rural environments are urgently needed, while strengthening the linkages between urban and rural areas. However, reasonable policy decisions should be based on a correct and comprehensive knowledge of current urban environments. Spaceborne remote sensing has been widely used in characterizing urban areas, because it can provide an objective and worldwide homogeneous perspective about urban growth and change.

1.2 Urban monitoring using spaceborne remote sensing imagery

In last few decades, many approaches for urban monitoring using spaceborne remote sensing have been developed, in order to extract urban extents, urban land use, as well as general parameters about the urban environment [1] [2] [3] [4] [5]. All these studies were aimed at discovering the spatiotemporal patterns of dynamic urban change, and exploited many different sensors, from multispectral to radar, from hyperspectral to LiDAR.

1.2.1 Urban area monitoring and change detection using multispectral sensors

Multispectral information has long supported a relatively detailed classification and change detection using post-classification comparison of land covers in urbanized areas, including buildings, grasslands, impervious surface, water bodies and more. For instance, in [6], multitemporal Landsat images were used to identify the spatiotemporal change patterns of built-up, vegetation, and water bodies. Impervious surfaces, one of the important parameters to urban meteorology, water cycle, and thermal environment models are another example of parameter that can be extracted from multispectral data [7] [8], and used as a proxy to urban growth [9].

A special case among multispectral sensors for urban monitoring is taken by the so-called *nighttime lights*. These data sets are a byproduct of the meteorologic mission called Defense Meteorological Program Operational Linescan System (DMSP OLS), which operated from 1992 until 2013, and the Visible Infrared Imaging Radiometer Suite Day/Night Band (VIIRS/DNB), which is its follow up mission, with a finer spatial resolution and more specific filters to collect data from artificial illumination at night (hence the name). These data sets depend on atmospheric conditions and seasonal changes, but, after calibration [10] [11], they are highly correlated to anthropogenic activities and energy consumption.

The first studies using these data were concentrated on spatially mapping urban extent, and inferring population density, greenhouse gas emissions and energy usage [12] [13] [14]. Then, regional comparison and geographical statistics about urban anthropogenic activities extracted from these data, such as the above mentioned urban extents, population, economic indicators, electric power consumption, and carbon emissions, showed that nighttime data are highly correlated with Gross Domestic Product (GDP) and total carbon dioxide (CO2) emissions [13] [15] [16] [17] [18] [19].

Finally, with the availability of long-term series nighttime data, the continuous observation of anthropogenic activities has become possible. allowing the extraction of different temporal patterns of urban changes [20] [21] [22] [23] [24] [25] [26]. Although these data have a rather coarse spatial resolution, the spatial change of urban structures, and their aggregated behavior up to the regional and national level can be extracted. Accordingly, the trajectory of urban centers as hotspot in nighttime light (NTL) time series have been studied in [27]. The same is true in [28] [29],[30], characterizing different temporal patterns of anthropogenic activities, energy utilization, and impervious surface expansion, in line with the general trend of rural-urban migration.

With the usage of temporal analysis technique, NTL time series can be decomposed into annual and seasonal fluctuations [31]. Moreover, the declining trend of NTL values have been observed and analyzed to explain the economic recession in Zimbabwe, and the phenomenon of the so-called “ghost cities” in P.R. China, due to excessive urbanization [32] [33] [34].

NTL and other multispectral sensors have also been used to study the link between land use change and urban areas, e.g. vegetation degradation and urbanization [35], for the estimation of impervious surfaces jointly exploiting MODIS and NTL [36], to add further information about land covers to explain the value-added of agriculture and forestry when measuring economic growth [37].

As for change detection using multispectral sensors, the most frequent techniques for urban monitoring are post-classification comparison, as well as regression simulation of time series of urban geophysical parameters. Sometimes, more specific techniques for change detection (e.g., improved change-vector analysis [38]) have been applied to build the feature space for classification. In [39] spatiotemporal series are regarded as spatial and temporal continuous fields, and from them the magnitude, timing and duration of urban growth are extracted. Similarly, variation information contained in time series can also be extracted by means of time series decomposition to extract trends and seasonal fluctuations [40] [41], possibly applying Mann Kendall trend test to monitor urban dynamics [42].

However, images from multispectral sensors are 2-dimensional representations of the Earth surface, and can provide information about 2D changes in urbanization, and highlight its effects. The change of vertical structures, and in general the characterization of changes involving the third dimension (here in the following referred to as "3D changes") is a very challenging task for spectral sensors. These changes are instead very important for urban planning and design, urban micro-climate, urban population density and others quantitative inversion applications requiring precise urban models [43] [44] [45]. More in general, 3D models are driven by the growing focus on 3D smart cities. The ability to update frequently this information is a promising research and application topic [46].

Compared to 2D change detection, 3D change detection needs to face big challenges due to data and computational costs, as well as the accessibility of accurate 3D data. Satellite platforms can provide high resolution optical images, and generate Digital Surface Models (DSM) from stereo/multi-view images [47] [48]. Alternatively, LiDAR point clouds, probably the more precise modeling method to reconstruct a city in 3D, may be used, but they are expensive both economically and computationally [49]. Indeed, LIDAR has been mostly used in monitoring natural disasters, such like landslide displacement [50], cliff recession [51], and, in urban areas, these phenomena correspond to 3D changes. However, these are sudden changes, while for urban monitoring we would like to have long-term monitoring of relatively slow (days, if not months) changes in the vertical direction. Only a few works use LiDAR for wide-area urban monitoring, due to the high cost of acquisition, whereas, most works are related to urban 3D precise modeling, as in [52] and [53].

Finally, it is important to stress that the primary issue referred to 3D change detection is the data co-registration, especially when heterogeneous sources with different reference systems are used, e.g., subsequent images and LiDAR data captured by mini-UAVs [54], or LiDAR and photogrammetric data [55]. Other examples of 3D change detection based on DSM are available in [56], [57], and [58], with a more general introduction to the topic in [59].

1.2.2 Urban area monitoring and change detection using radar sensors

This lack of an easy way to extract 2-dimensional and 3-dimensional changes in urban areas from multispectral sensors has motivated the focus of this work on time series of radar, and specifically Synthetic Aperture Radar (SAR) systems. The amplitude and polarization of a

SAR image can be used to extract maps of urban land covers like using multispectral data, and to monitor urbanization, too [60] [61] [62].

The mechanism of SAR imaging determines its application in the field of urban remote sensing, and is driven by the facts that SAR is a side-looking sensor, that collects the backscattered electromagnetic wave from a target, possibly at multiple polarizations, and retains both the amplitude and the phase information. Specifically, studying the effect of side-looking imaging of urban targets, and the related single and double-bounce scattering mechanisms, scholars have demonstrated that it is possible to reconstruct the building height and even the 3D model of a single building using very high resolution SAR imagery [63] [64] [65]. Moreover, the induced effects of shadows, overlay and foreshorten are closely related to building 3D structures, as shown in figure 1.1. It is therefore possible to utilize the overlay and shadow to recovery building heights and shapes [66] [67] [68]. Finally, since the backscattered signals may be decomposed into double bounce dihedral, facade, and volume scattering, these results may be used to obtain relatively accurate building footprints [69] [70] [71].

Unfortunately, although these results are theoretically possible for single buildings in specific imaging situations, real backscattered signals are noisy because of the limitations of the parameters of the radar system [72]. Accordingly, extraction results depend on the techniques applied. Examples are height inversion with a optimizing likelihood measure between the projection and the observed image over the height hypothesis space in [73], as well as a combination of a SAR simulator and a matching procedure to estimate the best height of buildings in [74].

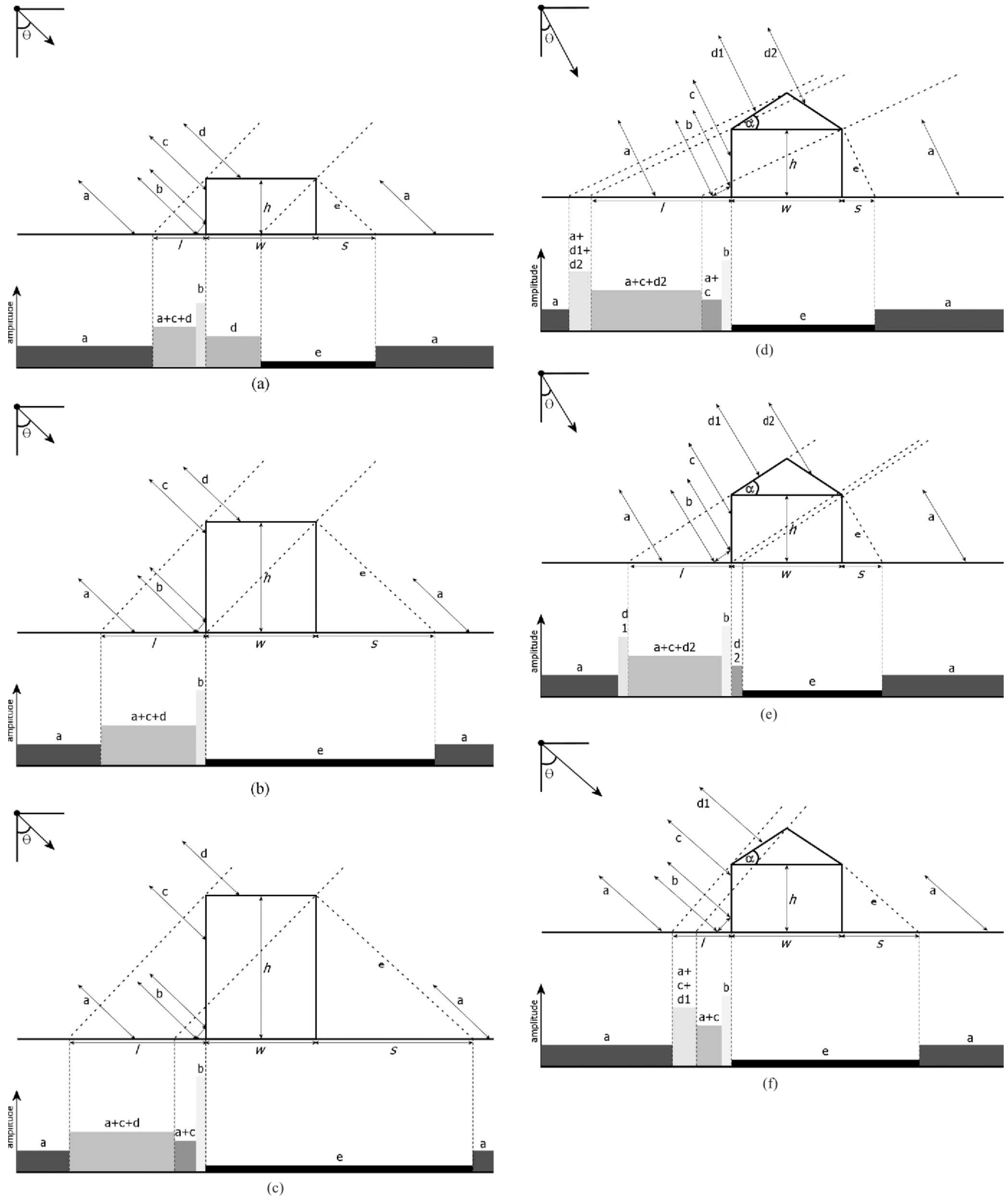

Figure 1.1: The side-looking nature of SAR systems causes foreshorten, shadow, and layover effects on buildings (from [68]). 1) a-c: Backscattering projection of a flat-roof building with width w and different heights h: Ground backscattering of a double-bounce scatterer b, backscattering of vertical wall c, backscattering from roof d, shadow e, length of layover area in ground-projected range l, and length of shadow projected on ground s. The gray level in the backscattering profiles indicate the corresponding intensity. (a) $h < w * tan(\theta)$. (b) $h = w * tan(\theta)$. (c) $h > w * tan(\theta)$. 2) d-f: Backscattering projection of a gable-roof building with roof inclination angle α at various incidence angles. The legends is similar to the one for flat-roof buildings in Fig. 1.1. $d1$ is the scattering from the side of the roof which is oriented toward the sensor, while $d2$ represents the scattering from the part of the roof which faces away from the sensor. The gray values in the backscattering profiles refer to corresponding intensity. (d) $\theta < \alpha$. (e) $\theta = \alpha$. (f) $\theta > \alpha$.

A method to improve urban analysis is to exploit, whenever possible, radar polarimetry. In radar systems, the emitted waves E_s and the backscattered waves E_i may be charactered by the so-called Jones vectors. Using a suitable transformation of these vectors, it is possible to identify the scattering characteristics of different objects by means of the so-called scattering matrix $\mathbf{S}$, where

$$E_s = \frac{e^-jkr}{r} SE_i = \frac{e^{-jkr}}{r} \begin{bmatrix} S_{hh} & S_{hv} \\ S_{vh} & S_{vv} \end{bmatrix} E_i \tag{1.1}$$

The parameters of urban structures, such as buildings' orientation, height and volume, directly impact polarimetric properties. The double-bounce scattering between the walls and the ground, in fact, depends on the building height and orientation [75] [64]. Moreover, the polarization orientation angle shift induced by the variation of the radar look direction with respect to artificial structures has been shown in [76] and [77], and has been successfully applied in recognizing the spatial arrangement of built-up structure, estimating urban density in [78] and [79].

All these effects can be summarized in the use of the polarimetric decompositions, i.e. different ways to decompose the scattering matrix identifying different effects and the corresponding polarimetric contributions. For instance, backscattering can be decomposed into surface scattering, double-bounce scattering, volume scattering and other scattering types as in [70]. There are multiple decompositions, classified in coherent and incoherent ones. The incoherent averaging of the coherency matrix T or covariance C matrices is specified to measure the polarimetric properties of so-called ”distributed targets”, characterizing time-varying targets or nearly equal-size targets in a resolution cell. The difference with respect to the incoherent decomposition is that the coherent measurement with no averaging is for dominant targets in a resolution cell, called point-targets [80]. In the case of monostatic backscattering (i.e., radar systems with co-located transmitter and receiver), the reciprocity constrains the scattering matrix to be symmetrical, that is S_{hv}=S_{vh}. All major decompositions are synthesized in Table 1.1.

In this table, polarimetric parameters derived from polarimetric decomposition models are listed: “Surf” stands for surface scattering, “Dbl” stands for double-bounce scattering, “Vol” stands for volume scattering, and “Hlx” stands for helix scattering. Corner marks indicate the model type. For instance, “v3” stands for the VanZyl decomposition. The separation of the different contributions to the final mixed scattered signal is significant to characterize urban targets, and this approach has been applied in land use classification, object recognition and damage estimation, e.g., in [91], [92], [60], and [93].

In addition to what has been introduced in the previous paragraphs, when multiple SAR images are available other extraction methods for 3D information can be used. For instance,

Table 1.1: Polarimetric decomposition theories and descriptions

Decomposition type	Decomposition theories	Equation	Decomposed parameters
Huynen type decomposition	Phenomenological Huynen Decomposition [81]	$\mathbf{T3} = \begin{bmatrix} \langle 2A_0\rangle & \langle C\rangle - j\langle D\rangle & \langle H\rangle + j\langle G\rangle \\ \langle C\rangle + j\langle D\rangle & \langle B_0\rangle + \langle B\rangle & \langle E\rangle + j\langle F\rangle \\ \langle H\rangle - j\langle G\rangle & \langle E\rangle - j\langle F\rangle & \langle B_0\rangle - \langle B\rangle \end{bmatrix} = \mathbf{T}_0 + \mathbf{T}_N$	$T11_{hu} = 2A_0 \; T22_{hu} = B_{0T} + B_T \; T33_{hu} = B_{0T} + B_T$
	Barnes-Holm Decomposition [82]	$\mathrm{T}(\theta)q = 0$	$T11_{ba} = \frac{(\langle C\rangle - \langle G\rangle)^2 + (\langle H\rangle - \langle D\rangle)^2}{2(\langle B_0\rangle - \langle F\rangle)} \; T22_{ba} = \frac{(\langle B_0\rangle + \langle B\rangle - \langle F\rangle)^2 + \langle E\rangle^2}{2(\langle B_0\rangle - \langle F\rangle)} \; T33_{ba} = \frac{(\langle B_0\rangle - \langle B\rangle - \langle F\rangle)^2 + \langle E\rangle^2}{2(\langle B_0\rangle - \langle F\rangle)}$
Eigenvalue-based decomposition	Cloude decomposition [80]	$\mathbf{T3} = \sum_{i=1}^{3} \lambda_i u_i u_i^{*T} = T_1 + T_2 + T_3 \; T_1 = \lambda_1 u_1 u_1^{*T}$	$T11_{cl} = 2A_0, T22_{cl} = B_0 + B \; , T33_{cl} = B_0 - B$
	Holm decomposition [83]	$\sum = \begin{bmatrix} \lambda_1 & 0 & 0 \\ 0 & \lambda_2 & 0 \\ 0 & 0 & \lambda_3 \end{bmatrix} = \sum_1 + \sum_2 + \sum_3 = \begin{bmatrix} \lambda_1 - \lambda_2 & 0 & 0 \\ 0 & 0 & 0 \\ 0 & 0 & 0 \end{bmatrix} + \begin{bmatrix} \lambda_2 - \lambda_3 & 0 & 0 \\ 0 & \lambda_2 - \lambda_3 & 0 \\ 0 & 0 & 0 \end{bmatrix} + \begin{bmatrix} \lambda_3 & 0 & 0 \\ 0 & \lambda_3 & 0 \\ 0 & 0 & \lambda_3 \end{bmatrix}$ $\mathbf{T3} = \mathbf{U_3} \sum_{\mathbf{i}} \mathbf{U_3^{*T}} = \mathbf{T_1} + \mathbf{T_2} + \mathbf{T_3}$	$T11_{cl} = 2A_0, T22_{cl} = B_0 + B \; , T33_{cl} = B_0 - B$
	VanZyl decomposition [84]	$\mathbf{C3} = \alpha \begin{bmatrix} 1 & 0 & \rho \\ 0 & \mu & 0 \\ \rho^* & 0 & \mu \end{bmatrix} = \Lambda_1 \begin{bmatrix} \alpha^2 & 0 & \alpha \\ 0 & 0 & 0 \\ \alpha^* & 0 & 1 \end{bmatrix} + \Lambda_2 \begin{bmatrix} \beta^2 & 0 & \beta \\ 0 & 0 & 0 \\ \beta^* & 0 & 1 \end{bmatrix} + \Lambda_3 \begin{bmatrix} 0 & 0 & 0 \\ 0 & 1 & 0 \\ 0 & 0 & 0 \end{bmatrix}$	$Surf_{v3} = \Lambda_1, Dbl_{v3} = \Lambda_2, Vol_{v3} = \Lambda_3$
	TSVM decomposition [85]		
Scattering-models-based decomposition	Freeman two-component decomposition [86]	$Span = P_{surf} + P_{vol}$	$Surf_{f2}, Vol_{f2}$
	Freeman three-component decomposition [87]	$Span = P_{surf} + P_{dbl} + P_{vol}$	$Surf_{f3} = f_s(1 + \lvert \beta \rvert^2), Dbl_{f3} = f_s(1 + \lvert \beta \rvert^2), Vol_{f3} = f_s(1 + \lvert \beta \rvert^2)$=
	Yamaguchi four-componentdecomposition [88]	$Span = P_{surf} + P_{dbl} + P_{helx} + P_{vol}$	$Surf_{y4} = f_s(1 + \lvert \beta \rvert^2), Dbl_{y4} = f_s(1 + \lvert \alpha \rvert^2), Hlx_{y4} = f_c, Vol_{y4} = f_v$
Coherent decomposition	Pauli decomposition [80]	$\mathbf{S} = \begin{bmatrix} S_{hh} & S_{hv} \\ S_{vh} & S_{vv} \end{bmatrix} = \frac{a}{\sqrt{2}} \begin{bmatrix} 1 & 0 \\ 0 & 1 \end{bmatrix} + \frac{b}{\sqrt{2}} \begin{bmatrix} 1 & 0 \\ 0 & -1 \end{bmatrix} + \frac{c}{\sqrt{2}} \begin{bmatrix} 0 & 1 \\ 1 & 0 \end{bmatrix} + \frac{d}{\sqrt{2}} \begin{bmatrix} 0 & -j \\ j & 0 \end{bmatrix}$	$Surf_{p3} = \frac{S_{hh} + S_{vv}}{\sqrt{2}}, Dbl_{p3} = \frac{S_{hh} - S_{vv}}{\sqrt{2}}, Vol_{p3} = \frac{S_{hv} + S_{vh}}{\sqrt{2}}, Asym_{p3} = j\frac{S_{hv} - S_{vh}}{\sqrt{2}}$
	Krogager decomposition [89]	$S(R,L) = \begin{bmatrix} S_{RR} & S_{RL} \\ S_{LR} & S_{LL} \end{bmatrix} = e^{j\theta} \left\{ e^{j\theta_surf} k_{surf} \begin{bmatrix} 0 & j \\ j & 0 \end{bmatrix} + k_{dbl} \begin{bmatrix} e^{j2\theta} & 0 \\ 0 & -e^{-j2\theta} \end{bmatrix} + k_{hlx} \begin{bmatrix} e^{j2\theta} & 0 \\ 0 & 0 \end{bmatrix} \right\}$	$k_{surf}, k_{dbl}, k_{hlx}$
	Cameron decomposition [90]	$\mathbf{S} = a \left\{ cos\theta_{rec} \left\{ cos\tau_{sym} S_{sym}^{max} + sin\tau_{sym} S_{sym}^{max} \right\} + sin\theta_{rec} S_{nonrec} \right\}$	$a = Span, \tau_{sym}$

one option is the fusion of ascending and descending imaging data sets. Indeed, while the drawback of side-looking imaging on buildings is that only one side of the building can be retrieved, spaceborne SAR sensors pass over the same location in both ascending and a descending mode. The ascending mode is when the satellite circles from South to North. On the contrary, the descending mode is when the satellite travels from the North to the South pole. The combination of ascending and descending observation can compensate the loss of information and reconstruct both sides of a building. This results has been widely applied to extract 3-D building models from images taken from opposite directions, orthogonal viewing directions, even from four-aspect SAR images, as in [94], [95], [96], and [97].

Finally, the unique advantage of SAR is that differential SAR Interferometry is a very effective technique for 3D change characterization, and has been already applied to urban areas [98] [99] [100] thanks to techniques like the persistent scatterer interferometry (PSI) [101], the Small BAseline Subset (SBAS) approach [102], SAR tomography (TomoSAR) or Differential TomoSAR inversion. All of these techniques can be used for 3D reconstruction in urban areas [103] ,[104], [105], [106].

Specifically, the task of retrieving building parameters using InSAR is based on the recognition of the different elements of a building, such as its roof and facade, exploiting the above-mentioned phenomena of layover, shadow and dominant scattering at building dihedral caused by the side-looking configuration of SAR systems. The combined effect of amplitude values, due to the projection of the building facade, and phase, related to the building height, has been proven in [107], [108], and [109]. To include 3D information, InSAR techniques, such as the above-mentioned PSI can detect stable points in a stack of several interferograms and retrieve their height based on their phase values [110]. InSAR results, however, are limited by their inherent noisy nature. Even with very high-resolution SAR and multi-aspect observations, the achieved 3D model is still not comparable to the results from LiDAR [108].

Instead, SAR tomography, using multiple SAR images acquired from slightly different looking angles, allows separating multiple scatterers layovered and situated in the same resolution cell (e.g., ground and wall scatterers) [111]. This approach has been used to retrieve the vertical structure of buildings in [105]. Eventually, point cloud fusion from multi-aspect TomoSAR data sets may be exploited to complete the 3D-building models as in [112].

Generic SAR change detection techniques

As for using SAR for urban monitoring in time, in the last decades successful techniques for change detection from SAR images, unsupervised and supervised, have been developed and simultaneously proved to be effective. The supervised approaches can be categorized as change detection after the classification of pre- and post-images [113] or directly from difference images [114].

Among unsupervised approaches, the general detecting procedure for SAR images can be implemented in three steps:

1. *Co-registration and speckle filtering*. Previously to any change detection, especially in per pixel approaches involving VHR SAR images, co-registration is necessary to ensure the consistency of pixel geolocation. Additionally, a denoising (despeckling) filtering procedure aims at increasing the signal to noise ratio (SNR) of the pre-event and post-event images, while preserving as many as possible textural details. Among the filters suitable to multiplicative speckle, the refined Lee filter [115], the sigma filter [115], and especially the non-local mean filter [116] have proved to be the most effective.

2. *Image dissimilarity computation.* To compare two images, simple and very often used per-pixel dissimilarity metrics are the difference and the ratio. Among these measures, the ratio operation has proved to be the most suitable for high-resolution SAR images regardless of the intensity level [117]. Alternatively, dissimilarity measures based on local statistics can be used to take into account any change in texture information. To this aim, Probability Density Functions (pdfs) in a variable-scale window are estimated with probabilistic inference, e.g., maximum-likelihood estimators (MLE) [118], log-cumulant estimators [119], or kernel density estimators [120]. Then, the dissimilarity between distributions for the same pixel neighborhood in different time instant is computed by means of the Kullback-Leiber (KL) divergence, the expectation of the logarithmic difference between the probabilities P and Q [121], or the Mutual Information (MI). The KL distance performance relies on a priori information on the local pdfs. In [118] [122] [120] and [123], pdf models like normal , Gamma , Rayleigh , G_0 , and complex Wishart distributions are considered. Information-based similarity measures, instead, including distance to independence, mutual information, cluster reward, Woods criterion, and correlation ratio, were compared in [124] and [123]. The results show that Mutual Information is more efficient than other measures. More recently, the mixed information has been introduced in

[125], unifying mutual information and variational information by means of a tradeoff parameter.

The limitation of classical detectors based on the pixel-wise ratio is due to the degradation of image quality induced by speckle. Although the local-homogeneity based strategies of neighborhood-averaging [126], Markov Random Field (MRF) [127] [128] and Conditional Random Field (CRF) [129] have been used to model the spatial correlation among neighboring pixels and to reduce the uncertainty induced by noise, it is still hard to determinate the appropriate scale tradeoff between smoothing and preserving texture information. Novel techniques recently introduced to deal with this dilemma include temporal filtering [130] and non-local similarity measurement [131] [132] [133].

In fact, change detection with consistency operation is only effective for first-order statistics and comparison of SAR images. The texture is assumed as a zero-mean multiplicative contribution. Consequently, texture changes that preserve the zero-mean go undetected with first-order indicators. In [120] [134], the ”ordered-change” are defined and tested with first-, second- and third-order-based statistics, which confirmed the effectiveness of Log-cumulants and mutual information for higher-order changes.

Noteworthily, the fact is that the increasing availability of multidimensional SAR data leads to even greater challenges. For SAR images collected by PolSAR sensors or at multiple radar frequencies, the complex Wishart distribution and its extension have been widely used, provided the spatial resolution is the same [135] [136] [137] [138]. Whenever the resolution is not the same, prevailing techniques are those focusing on a multiscale representation of either the change image or the pre- and post-event pairs [139] [140] [141]. For instance, the undecimated discrete wavelet transform allows decomposing a log-ratio image into a pyramid of new images at multiple scales. Change detection is then applied to this pyramid, for instance, in a hierarchical way, from coarser to finer scales [142] [143]. Other transform-domain methods applied to multi-scale representation are seldom used, an example is the contourlet transform in [144].

3. *Change area extraction.* Once the dissimilarity measures are computed, the most direct method to extract the changes is to threshold these vales. Many thresholding techniques have been proposed. In [145] a mixed distribution model was introduced for thresholding the change image under the assumption that both changed

and unchanged pixels follow a generalized Gaussian distribution, whose parameters are estimated through an expectation-maximization (EM) algorithm. In [126] and [146] the Kittler and Illingworth thresholding (GKIT) algorithm is applied to neighborhood-based ratio images. It must be noted, however, that the selection of the threshold(s) is not trivial in case of multidimensional changes. The decision on the multidimensional difference image can be regarded as a clustering (e.g., by fuzzy clustering [147]) or hypothesis test (e.g., by the generalized likelihood ratio test [148]). Likelihood ratio test (LRT) comprises no change hypothesis, the so-called null hypothesis, and an alternative change hypothesis, and the rejection or acceptance of the null hypothesis depends on the desired confidence level, to avoid falsely classifying low-SNR regions as changes [149] [150] [151] [138].

SAR change detection in urban areas

More specifically, change detection using SAR images over urban areas has been used for multiple applications, from urbanization to urban flood mapping, from earthquake damage extraction to building recognition. Given the multiple geographical scales of urban change, in the following the focus will be on urban change detection and monitoring using SAR and InSAR at the building, block, city and regional/global scale.

In very high resolution (VHR) SAR images, like SpotLight TerraSAR-X and Cosmo-Skymed data sets the contextual information presents detailed geometric structures of single buildings. It enables, too, the determination of the position or change of building elements, not just the change of a building itself. However, the building projection on VHR SAR is sensitive to the radar incidence and azimuth angles. To reduce this problem, it has been proposed to simulate the building appearance in VHR SAR images and detect geometric projection change [152] [153]. Other methods include the use of textural information, such as the detection of changes using an edge-preserving model in [154], or the discrimination of individual building damage class using gray-level co-occurrence matrix (GLCM).

SAR data sets with spatial resolution coarser than 1 meter do not allow to discriminate individual building and its parts. Hence, this kind of SAR data is used to observe block or city-level changes and dynamic phenomena, exploiting the SAR width-swath acquisition and all-weather capabilities. For instance, ALOS/PALSAR and Sentinel-1 SAR were used to detect earthquake-induced changes in the built-up area according to a change in the scattering mechanism [155] [156] [157] [158] [159]. Natural disasters, e.g., floodwater and anthropogenic disasters, e.g., wars and conflicts, can be detected using Sentinel-1 InSAR coherence images [160] [161], as well as by using harmonic analysis with multitemporal ENVISAT ASAR time series with a spatial resolution of 150 m [162].

Finally, investigation of the global and regional changes in the Earth system is of great importance to systematically understand and solve planetary-scale human issues, like urbanization. It is undoubtedly efficient and effective to utilize remote sensing as the global observation instrument. In order to explore the urbanization patterns, coarse resolution active remotely sensed data have been mosaicked to map urbanized areas and their growing change. For example, in [163] data from two spaceborne sensors, backscatter power from NASA SeaWinds microwave scatterometer with a spatial resolution of 0.05°, and nighttime lights with a resolution of 1 kilometer, are used to report large increases in built-up infrastructure stock worldwide and show that cities are expanding both outward and upward. The urban and suburban environments studies with scatterometers suggest that its signatures correspond to buildings and infrastructures density, allowing the possibility of a global survey on urban and suburban environments and their changes [164]. QuikSCAT data were processed via Dense Sampling Method (DSM) to reveals urban growth in the 2000-2009 period with a focus on the expansion of major urban areas in the US Great Plains in [165]. Further studies in this direction have shown complementary results for global urban urban extent mapping using high resolution SAR data on [166] [167].

1.3 Challenges and objectives

According to this review about 2D and 3D change detection in urban areas, it is possible to extract a few open challenges.

- First of all, it is clear that a simple and binary change/no change detection is not sufficient to support research on dynamic urban phenomena. Most previous attempts fall into change mapping rather than change pattern research. Indeed, multiple changes and deeper mining into change characteristics (e.g., change direction and amplitude) is scarce and urgently required. In this thesis, novel approaches are designed to search for and visualize multiple change patterns, leading to a more comprehensive understanding of global, regional and single-city-level urban growth and development processes.

- The Integration of heterogeneous sensors has great potential in the investigation of urban growing and development patterns, but it leads to additional issues with respect to processing and analyzing the merged data. On the one hand, the usage of heterogeneous source data sets leads to challenges in fusing multi-resolution, multichannel and multimodality data, because previous probabilistic models based on data collected by the same sensor are not suitable to this new kind of “combined” data. On the other hand, the information collected from diverse sensors contributes to more interesting discoveries.

- Since previous urban change studies are mainly based on spatial domain analysis, change patterns in time-domain deserves more substantive exploration. In this work, time series analysis by spatial pre-filtering and temporal clustering are introduced to understand urban construction activities for both developed and developing metropolis worldwide.

1.4 Dissertation organization

As mentioned above, the increasing availability of multi-polarization SAR, as well as the possibility to access data from temporal series of heterogeneous sensors with multi-resolution and multimodality, motivates this thesis to exploit them all and extract patterns of urbanization activities in various test areas worldwide. Accordingly, this thesis is structured into 6 Chapters.

The current chapter has introduced the aims of the thesis and provided a short review of previous techniques in the field of change detection in urban areas, with focus on using SAR data.

Chapter 2 is aimed at introducing a superpixel method to detect changes from polarimetric multitemporal SAR (PolSAR) data, with particular emphasis on the selection of the most suitable polarization decomposition for urban area characterization, and its application to 2D/3D urban growth mapping. The experiments introduced in this chapter assess the performance of Quad and Dual-PolSAR data for intra-urban as well as urban extent change detection.

Chapter 3 improves the results of the previous chapter by focusing on change analysis using short yet dense time series. Specifically, time series of SAR intensity and coherence data from Sentinel-1 (with a revisit time close to 12 days) are used to monitor urban change patterns, and discriminate among building maintenance, construction, demolition or reconstruction, as well as among change patterns with (very) different durations along the timeline.

Chapter 4 introduces instead a technique based on heterogeneous source data sets to map multi-type changes inside urban extents (e.g., intra-urban 2D/3D changes). By considering data sets at the beginning and end of a time period (in this work, one to three years), and comparing the original situation with the changes in the appearance of urban areas in both radar and multispectral (nighttime) images, we prove that it is possible to recognize different types of changes inside the human settlements, and to discriminate those that mostly refer to urban expansion/contraction (2D changes) from those that imply a change in the height or structure of the urban built-up elements (3D changes).

To generalize from cities to geographical regions or nations, in Chapter 5, a few metropolis in different geographical locations are analyzed in both the space and the time domain. Exploiting the previously presented approaches, improved by means of a novel hierarchical clustering technique, urban changes are mapped in terms of multiple spatiotemporal patterns, generated by vectorized change describers and exploiting the combination of SAR and multispectral data.

Finally, Chapter 6 provides a comprehensive review of the research carried out in these years and concludes the thesis by summarizing the novel achievements and highlighting possible future research paths.

Chapter 2

Superpixel-based 2D/3D change detection using SAR polarimetry

2.1 Introduction

As mentioned in the introduction, it is possible to find scientific literature where geometric and electromagnetic models are used to retrieve building height and shape from single very high resolution (VHR) SAR imagery but the height information can be obtained only for isolated buildings either from double-scattering or shadows. Unfortunately, due to the side-looking imaging of SAR, an accurate reconstruction of 3-D features for buildings needs multiple SAR images, and this type of acquisition is expensive. Instead, by considering polarimetric decomposition theory, backscattered signals from buildings can be separated into surface-scattering, double-scattering, volume-scattering, and helix-scattering components. This decomposition suggests that it may be possible to distinguish among different scattering phenomena from walls, roofs, and ground. By this way, even without actually reconstructing the building 2D/3D structure, it could be possible to understand whether a change has occurred, and which type of change as well.

Still, due to the complexity of the urban landscape, at a VHR spatial resolution, the multiple reflections by walls, roofs, and artificial and natural surfaces impair the capability to easily extract meaningful semantic representations. This issue may be solved by adding neighborhood constraints, like in Markov random field models [168] . Another option, explored in this chapter, is to exploit superpixels, i.e., groups of pixels with similar intensity, texture, and contextual information[169]. This idea has been explored in the context of change detection in [170]and [171], but in a preliminary way and without considering polarimetric features.

Accordingly, in this chapter, an unsupervised 2-D and 3-D urban change detection scheme is proposed exploiting Quad-PolSAR and Dual-PolSAR data. Changes are extracted by segmenting the PolSAR image into superpixels, to enhance the balance among change components and increase estimability of prior distributions. Positive and negative change components for built-up areas, in both the horizontal and the vertical directions, are properly extracted by assuming a multivariate Gaussian mixed model applied to a subset of polarimetric parameters at the superpixel level. To examine the performance on exploring 2D/3D changes, we tested Radarsat-2 Quad-PolSAR and Sentinel-1 Dual-PolSAR (VV/VH) images over cities in P.R.China and Latin America.[1]

2.2 Superpixel-wise change detection method for multi-temporal PolSAR images

The procedure applied in this work is based on the idea to apply superpixel segmentation to the change image, and detect changes in a subspace composed by a selection of polarimetric decomposition features, as opposed to the original data. The idea is to select specific features that are more affected by changes in the 2D and 3D structure of the building distributions. Subsequently, statistical measures of the selected features are computed for the multitemporal data sets in each superpixel, and eventually, their distribution automatically segmented into positive, negative, and no-change classes. The overall structure of the method is presented in Fig. 2.1

To keep the boundary consistence, here we operate the segmentation directly on the change image rather than the original multi-temporal images. Then, the superpixel boundaries will be applied, as mentioned, to multi-temporal polarimetric features. Let's start from two accurately co-registered SAR images $X_1 = \{x_1(m,n) > 0 | 1 < m < M, 1 < n < N\}$ and $X_2 = \{x_2(m,n) > 0 | 1 < m < M, 1 < n < N\}$, where M and N are the rows and columns of the SAR images. As proved in [117], ratio difference is one of the most suitable measure to describe change of polarimetri SAR. Therefore, the single-channel change image *CD* is calculated as follows

$$CD(m,n) = \log\left(\frac{x_2(m,n)}{x_1(m,n)}\right) \tag{2.1}$$

Considering the statistical distribution of a SAR intensity image, the segmentation algorithm is often applied to the log-ratio image as opposed to the difference image. Then, the superpixel segmentation is operated on the CDs and generates the superpixel image

---

[1] This chapter is based on the work: M. Che, P. Gamba, "2- and 3-Dimensional Urban Change Detection with Quad-PolSAR data", IEEE Geoscience and Remote Sens. Lett., vol. 15, no.1, pp. 68-72, Jan. 2018, and M. Che and P. Gamba, "Possibilities and Limits of Urban Change Detection Using Polarimetric SAR Data", Proc. of IGARSS'18, Valencia (Spain), July 22-27, 2018, pp. 6079-6082.

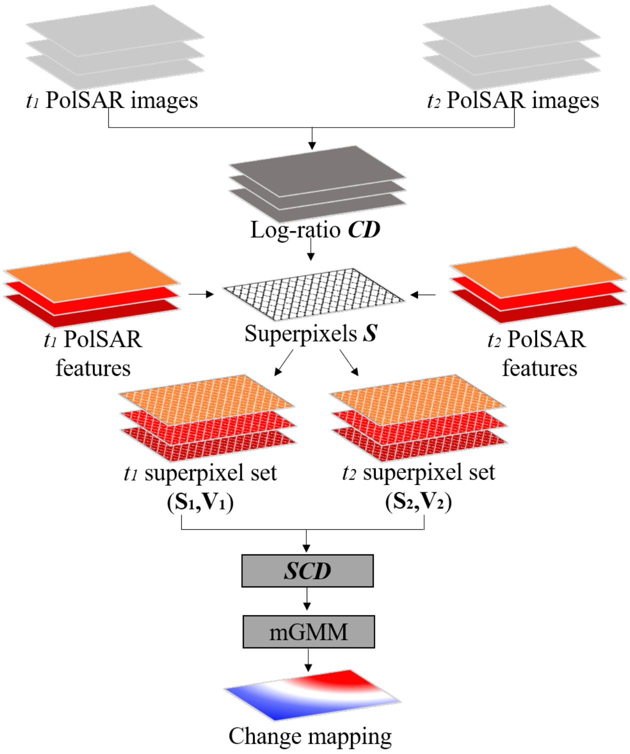

Figure 2.1: Overall workflow of the proposed technique.

$S = \{s_i | i = 1, 2, 3, \ldots, J\}$, where s_i is the i-th segment and J is the number of superpixels in the segmented image.

2.2.1 Adaptive distance measure in segmentation

The critical step of the proposed approach is the generation of the superpixels. To segment wide-area change images *CDs* a fast scheme is required. In this paper the algorithm called Simple Linear Iterative Clustering (SLIC) [172] is implemented to segment *CDs* into superpixel images. SLIC operates a k-means clustering on a limited window rather than on the whole image, and thus efficiently decomposes an image into homogeneous regions. Similar to the mean shift or quick shift, each pixel is associated with a feature vector that contains the pixel location and pixel value. SLIC can control the number of superpixels by means of two parameters: the nominal scale of the superpixels L, defined as the square root of a superpixel area A ($L = \sqrt{A}$), which in turn decides the width of the window for local clustering by k-means. and the strength of the spatial regularization, which influences the compactness of each superpixel. The larger the space regularization value, the better the compactness.

The algorithm works by first subdividing the original image into a grid, initializing the clustering center for each grid region. Then, k-means clustering is applied to each element of the grid by means of the standard Loyd algorithm, alternating the assignment of pixels to the closest center to the computation of updated cluster centers [173]. The distance measure to local centers in SLIC comprises two components, namely the spatial distance and the Euclidean distance in feature space. Considering co-registered multichannel SAR images $X_1 = \{x_1(m,n,d) > 0|1 < m < M, 1 < n < N, 1 < d < D\}$ and $X_2 = \{x_2(m,n,d) > 0|1 < m < M, 1 < n < N, 1 < d < D\}$, where M and N are the number rows and columns of the SAR images, respectively, and d is the index of the channel of the SAR image, the multichannel distance measure can be calculated as the sum of the two contributions:

$$D_s(i,j) = \sqrt{(m_i - m_j)^2 + (n_i - n_j)^2} \tag{2.2}$$

$$D_f(i,j) = \sqrt{\sum_{d=1}^{D} (x_d^i - x_d^j)} \tag{2.3}$$

hence by means of

$$D(i,j) = D_s(i,j) + D_f(i,j) \tag{2.4}$$

where the i,j are two different pixels at different locations.

In this formulas both distances are computed as standard Euclidean distances. For polarimetric images, however, previous researches confirmed better performances when using the Wishart distance for the D_f term:[137]

$$D_f(i,j) = D_w(i,j) = \frac{1}{2} tr(\mathbf{C}_j \mathbf{C}_i^{-1} + \mathbf{C}_i \mathbf{C}_j^{-1}) - q, \tag{2.5}$$

where $tr(\cdot)$ stands for the trace of a matrix, the $^{-1}$ is the inverse symbol, $\mathbf{C}_i$ is coherency matrix or covariance matrix, and q is dimension of matrices.

2.2.2 Superpixel-wise dissimilarity description to multiple changes

Once the original image has been segmented into homogeneous patches, pixel values inside each superpixel still follow a specific statistical distribution, e.g., a Rayleigh distribution, or aChi-square distribution (see Fig. 2.2). Accordingly,for each superpixel polarimetric features are represented by a few statistical descriptors. Specifically, several statistical moments (mean, variance, skewness, and kurtosis) and the covariance matrix are used. Eventually, the set $(\mathbf{S}, \mathbf{V}) = \{(s_i, \mathbf{v}_i)|i = 1, 2, 3, \ldots, J\}$ is built, where $\mathbf{S}_i$ is the i-th superpixel, and $\mathbf{v}_i$ its corresponding set of statistical descriptors.

Once the superpixels are obtained, and polarimetric features are represented by statistical descriptors in each superpixel, a strategy to measure the dissimilarity between superpixels in multitemporal images is required. Apart from the Euclidean distance, we tested

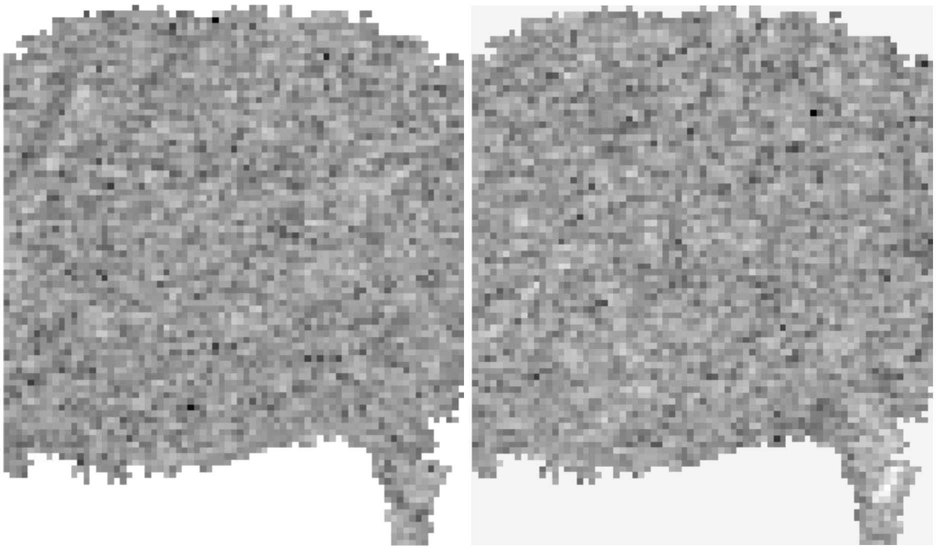

(a) A superpixel at t_1 (b) A superpixel at t_2

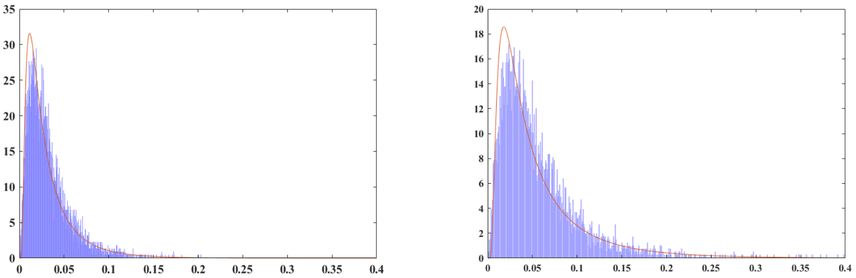

(c) Histogram of pixels in the superpixel at t_1 (d) Histogram of pixels in the superpixel at t_2

Figure 2.2: An example of superpixel and its statistical distribution at t_1, t_2.

dissimilarity measures based on the covariance of the moment-based descriptor sets, and specifically the Bartlett distance [174] and the Wishart distance [175]. Table I lists the equations to compute these dissimilarity indexes for the i-th superpixel and build the so-called superpixel change detection data set (SCD). In Table I EVD, BD, WD, and ECD stand for Euclidean vector difference, Bartlett difference, Wishart difference, and Euclidean covariance difference, respectively, C_{2i} and C_{1i} represent the covariance matrices of the moment-based descriptor sets from two SAR images and the same i-th superpixel, $|C|$ represents the determinant of C, tr() is the trace, and d is the dimension of the feature vectors. It must be noted that EVD is a vector of differences, while BD, WD and ECD are scalars.

Table 2.1: Superpixel Change Detection (SCD) via different dissimilarity measures at the superpixel level

Method	Equation
EVD	$\text{SCD}_i = \mathbf{v}_{2i} - \mathbf{v}_{1i}$
BD	$\text{SCD}_i = \ln(\frac{\|C_{2i} + C_{1i}\|^2}{\|C_{2i}\|\|C_{1i}\|}) - 2d * \ln 2$
WD	$\text{SCD}_i = \ln \frac{\|C_{2i}\|}{\|C_{1i}\|} - \text{tr}(\frac{C_{1i}}{C_{2i}}) - d$
ECD	$\text{SCD}_i = \|C_{2i} - C_{1i}\|$

2.2.3 Multiple-component change pattern detecting with GMM clustering

Once the SCD has been extracted, changes can be detected in an unsupervised manner by applying a clustering technique. In this work we consider a three-component multivariate Gaussian mixed model (mGMM) [176] to discriminate among negative change ω_{neg}, positive change ω_{pos} and no-change ω_{non} components, automatically selecting two thresholds (λ_1 and λ_2). According to the total probability theorem, the probability distribution of the superpixel change image is given by

$$p(s_i) = \sum_{i=1}^{3} w_i p(s_i|(\mu_i, \epsilon_i)) \tag{2.6}$$

where w_i is proportion or prior probability of each component. The thresholds λ_1 and λ_2

are decided by the observation posterior probability

$$p(w_i\ z) = \frac{w_i p(z|(\mu_i, \epsilon_i))}{\sum_{i=1}^{3} w_i p(z|(\mu_i, \epsilon_i))} \quad i = 1, 2, 3 \tag{2.7}$$

under the conditions

$$p(\omega_{neg}|\lambda_1) = p(\omega_{non}|\lambda_1), \quad p(\omega_{non}|\lambda_2) = p(\omega_{pos}|\lambda_2). \tag{2.8}$$

In order to accurately estimate the parameters $(\omega_i, \mu_i, \epsilon_i)$ for each component, a standard Expectation Maximization (EM) algorithm is applied.

2.3 Experimental results

2.3.1 2D/3D change detection using Quad-PolSAR SAR

To test the approach and discuss the usefulness of different polarimetric features, in this work two Radarsat-2 Quad-PolSAR images are used as a test set, both acquired over Nanjing, P.R. China, on March 27, 2008 and March 25, 2013, respectively. The pre-processing for PolSAR images includes calibration, speckle denoising, co-registration and geocoding. Most importantly, the denoising greatly impacts the outcome of superpixel segmenting. Therefore, here several most widely used speckle filters are introduced, such like Refined Lee Filter (RLF), Improved Lee Sigma Filter (ILSF), Non-Local denoising for (Pol)(In)SAR (NL-SAR) [177] [115] [116]. Apparently, in figure 2.4 the NL-SAR filter shows the best denoising result.

To both images polarimetric transformations, using Pauli, VanZyl , Freeman-Durden, and Yamaguchi decomposition techniques (see [80]), were applied. Ground truth areas (see Fig.2.2) were manually selected using freely available VHR images of selected urban locations in the two selected years. Positive changes (shown in red) refer to urbanization (e.g., new built-up areas), but also to low-rise buildings turning into high-rise buildings. Conversely, negative changes (shown in blue) represent phenomena of urban area degradation (e.g., abandoned or dismantled industrial areas), but also high-rise buildings turning into low-rise buildings. The non-change areas are shown in white color. In order to verify our hypothesis, this pixel-based ground truth is converted into a superpixel-based ground truth. Specifically, when the number of pixels labeled with the same change/no change class is more than half the total pixel number, the superpixel is assigned that label.

In this example, the superpixel average size is 621 pixels, and 27 positive change, 22 negative change, and 19 no-change superpixels are obtained by this procedure from the areas highlighted in Fig.2.3.

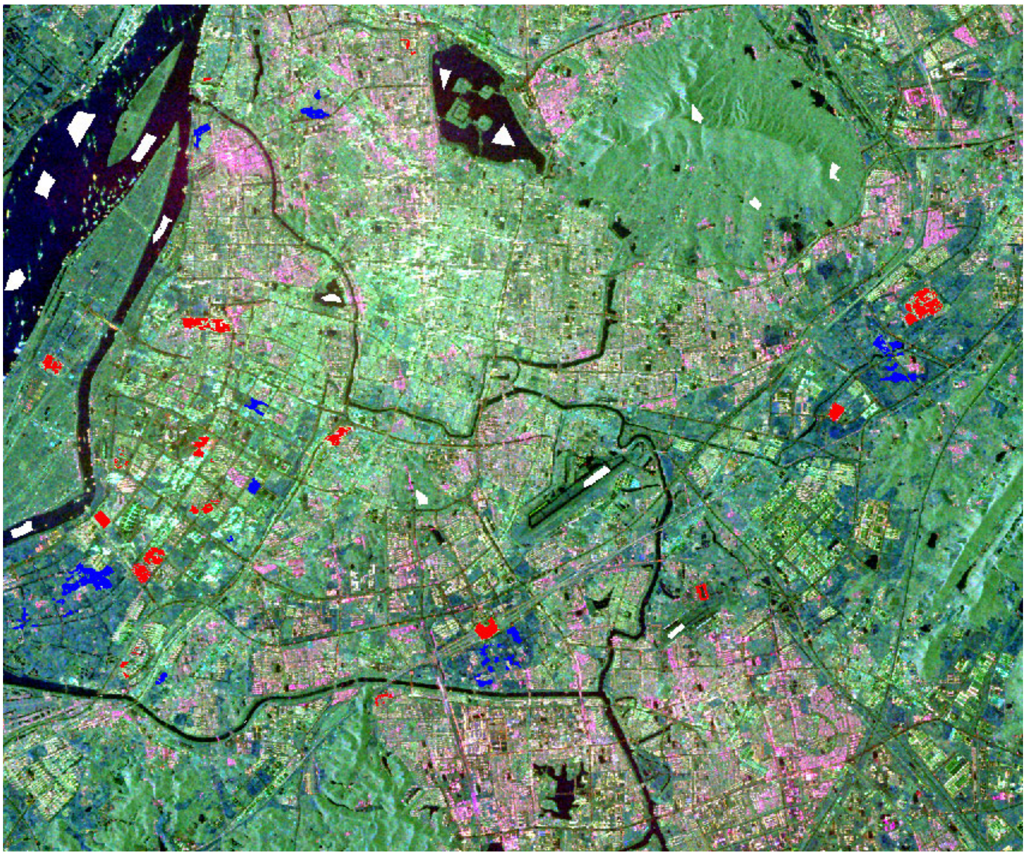

Figure 2.3: Pauli decomposition composite image on March 25, 2013, highlighting in red/blue/white the selected positive/negative change/no change areas in the ground truth.

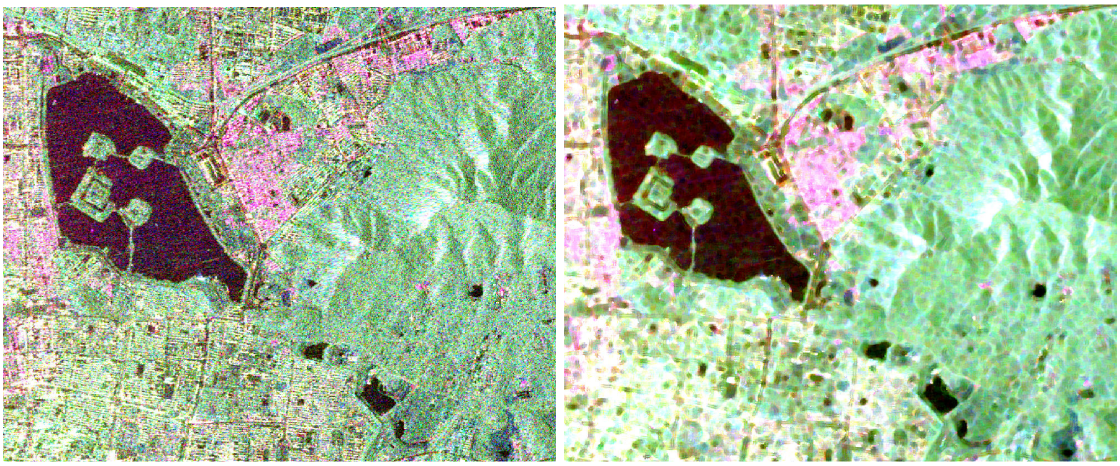

(a) Non filtered composite image (b) 7 × 7 Refined Lee filtered

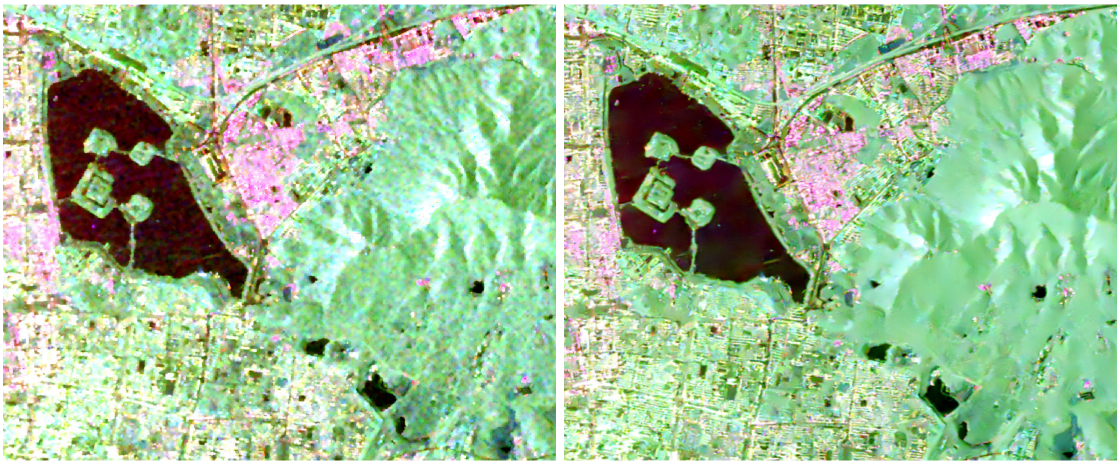

(c) 7 × 7 Improved Lee Sigma filtered (d) NL-SAR filtered

Figure 2.4: Pauli decomposition images after applying various de-speckle filters.

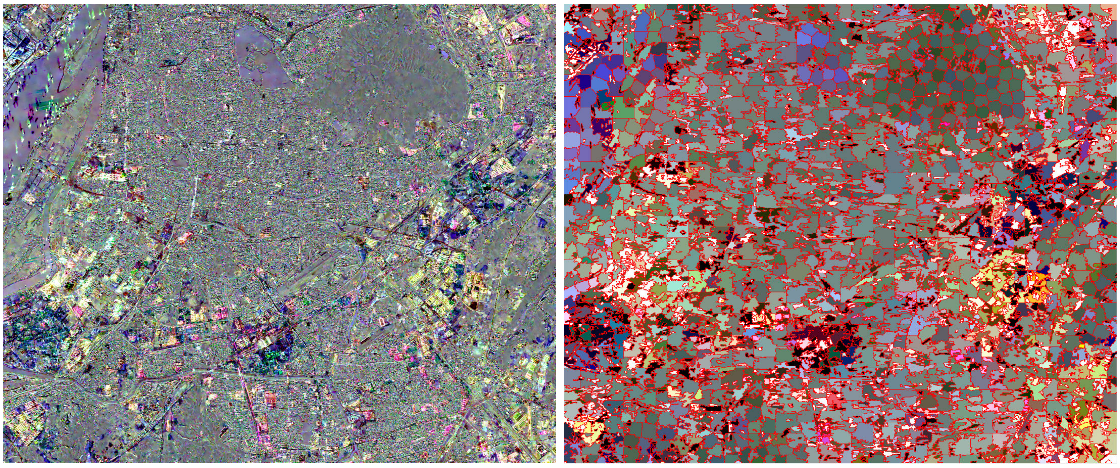

(a) The Pauli CDs after denoising with NL-SAR filter (b) The superpixel CDs after segmentation and averaging in each surperpixel.

Figure 2.5: The pixel-wise CDs and superpixel-wise CDs

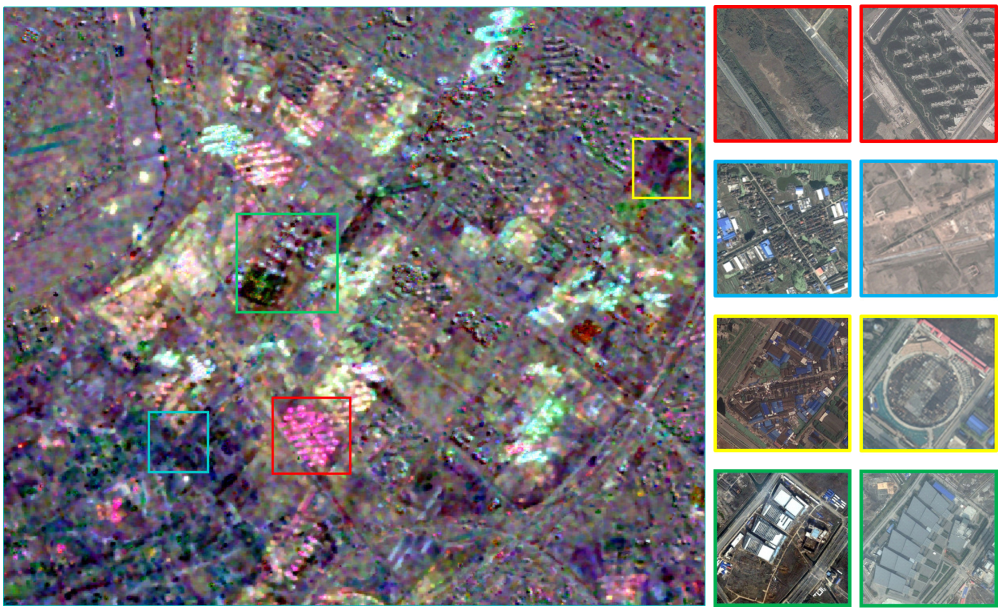
(a) (b) (c)

Figure 2.6: Examples of negative and positive changes: (a) False color change picture obtained using Pauli decomposition applied to a small portion of the Radarsat-2 2008 and 2013 images, with snapshots of (b) 2008 and (c) 2013 optical images of selected locations, highlighted with different colors.

Table 2.2 lists the superpixel-based and pixel-based validation of the detected change for a superpixel mean size of 621 pixels, as mentioned above, using single polarimetric feature, and always EVD as the difference measure applied to a 3-dimensional vector (mean, median and second central moment). The details of these parameters are given in table 1.1. Indeed, in Fig.2.7 histograms for the tested dissimilarity measures and for all the ground truth superpixels show large differences in the discriminative power of each of them. Specifically, notwithstanding what is reported in [174], the covariance-based descriptor BD is apparently unfit to discriminate between positive and negative changes in our case.

From Table 2.2 it is clear that, as somehow expected, the volume-scattering components (Freeman volume scattering Vol_{f3} and Yamaguchi volume scattering Vol_{y4}), the double or even-bounce scattering oriented at $0°$, Dbl_{p3} $(10\log|S_{hh} - S_{vv}|)$, and the double or even-bounce scattering oriented at $45°$ or volume scattering, Vol_{p3} $(10\log|S_{hv} + S_{vh}|)$ are the features most capable to catch the positive and negative changes in building height and density.

Another factor that impacts the result is the speckle noise. Thanks to the NL-SAR filter, better denoising on CDs enable to improve the compactness of superpixels, which

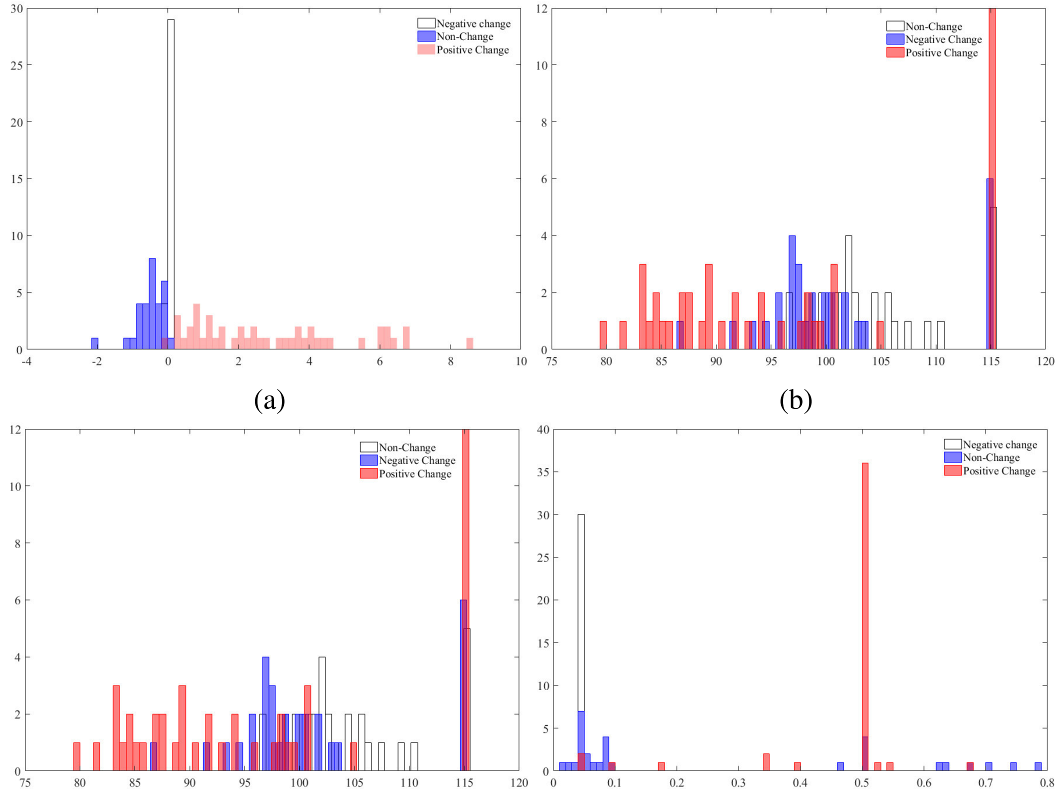

(a) (b)

(c) (d)

Figure 2.7: Graphical comparison of the discriminative power of different dissimilarity descriptors in case of three-component changes: histograms of (a) EVD (1^{st} component), (b) ECD, (c) BD, and (d) WD values for all the ground truth superpixels, colored according to their class of change. x-axis indicates the distance calculated, y-axis means the statistical frequences.

contribute less debris in change mapping (2.8b) compared to the result of Refined Lee Filter (RLF). Simultaneously, For Quad-PolSAR images, the SNR level is higher in primary polarimetric vectors and second order statistical matrix representations, while the parameters derived from model-based decompositions, like the Freeman-Durden and Yamaguchi decompositions, produce secondary noise because of the scattering diversity in a resolution cell. Accordingly, the Freeman double-bounce scattering and the Yamaguchi double-bounce scattering components provide a lower accuracy than the Pauli double-bounce scattering component. This can be addressed by using a better denoising filter. In table 2.2, the detected results of Freeman double-bounce scattering Dbl_{f3} and VanZyl double-bounce scattering Dbl_{v3} have been greatly improved with NL-SAR filter. However, the performance of the VanZyl volume scattering Vol_{v3} and Yamaguchi volume scattering Vol_{y4} decreased.

Table 2.2: Change detection results using different polarimetric parameters

Parameters	Refined Lee filter(RLF)				Non local denoising (NL-SAR)			
	Superpixel Level		Pixel Level		Superpixel Level		Pixel Level	
	OA/%	Kappa	OA/%	Kappa	OA/%	Kappa	OA/%	Kappa
Dbl$_{f3}$	65,67	47,50	62,69	42,86	**83,58**	**75,43**	**83,65**	**75,45**
Surf$_{f3}$	64,18	45,55	59,45	37,94	80,60	70,41	73,95	60,56
Vol$_{f3}$	**95,52**	**93,24**	**92,26**	**88,33**	**97,01**	**95,50**	**93,95**	**90,89**
Surf$_{p3}$	83,58	75,12	84,49	76,65	85,07	77,27	84,25	76,24
Dbl$_{p3}$	**97,01**	**95,50**	**94,82**	**92,20**	**97,01**	**95,50**	**94,88**	**92,29**
Vol$_{p3}$	**95,52**	**93,24**	**92,26**	**88,33**	**98,51**	**97,75**	**94,11**	**91,13**
Dbl$_{v3}$	53,73	29,35	52,86	28,25	**95,52**	**93,23**	**94,19**	**91,24**
Surf$_{v3}$	80,60	70,53	80,19	70,21	65,67	46,81	69,04	53,62
Vol$_{v3}$	**95,52**	**93,26**	**92,68**	**88,97**	**89,55**	**84,11**	**86,05**	**79,03**
Surf$_{y4}$	62,69	43,30	59,30	37,66	59,70	38,11	58,09	35,56
Dbl$_{y4}$	58,21	38,19	55,20	32,66	70,15	53,31	66,98	49,72
Vol$_{y4}$	**97,01**	**95,49**	**92,49**	**88,69**	**88,06**	**82,06**	**87,28**	**80,84**
Hix$_{y4}$	71,64	58,08	69,46	54,70	83,58	74,79	80,90	71,09

Going forward, Table 2.3 lists change detection results considering multiple parameters. It is apparent that the combination of more parameters increases the change detection accuracy, as compared to the use of a single feature. The largest superpixel-based overall accuracy (97.06%) is obtained by jointly considering the Dbl_{p3} ($10 \log |S_{hh} - S_{vv}|$), the Vol_{f3} (volume-scattering component of Freeman-Durden 3-component decomposition), and the Vol_{y4} (volume-scattering component of the Yamaguchi 4-component decomposition) parameters. The corresponding change detection results for the whole Nanjing area are shown in Fig.2.8a.

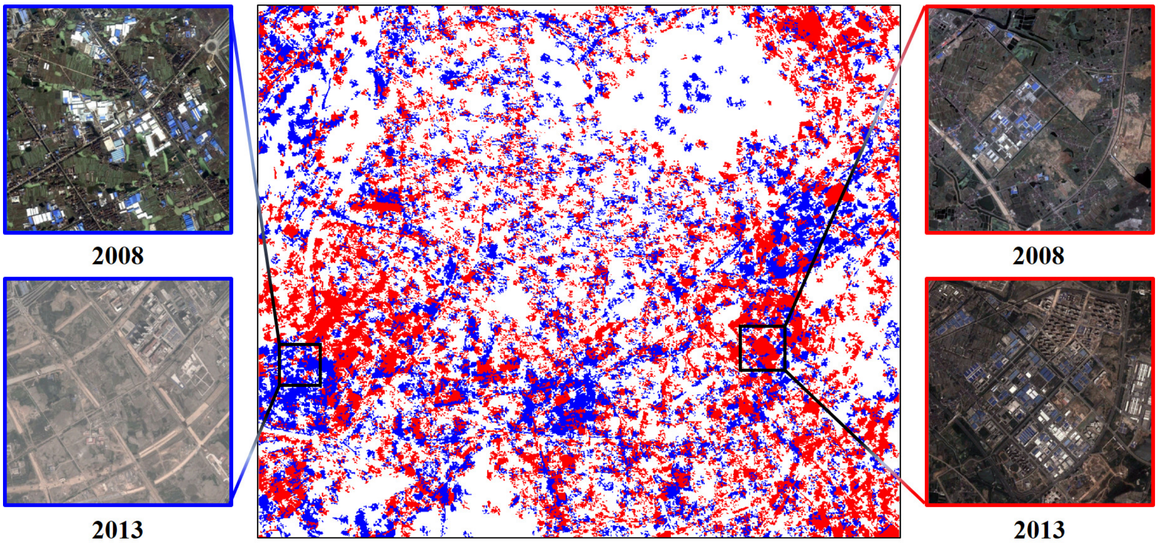

(a) Change mapping results using the Refined Lee despeckling filter: total change map with a couple of magnified samples.

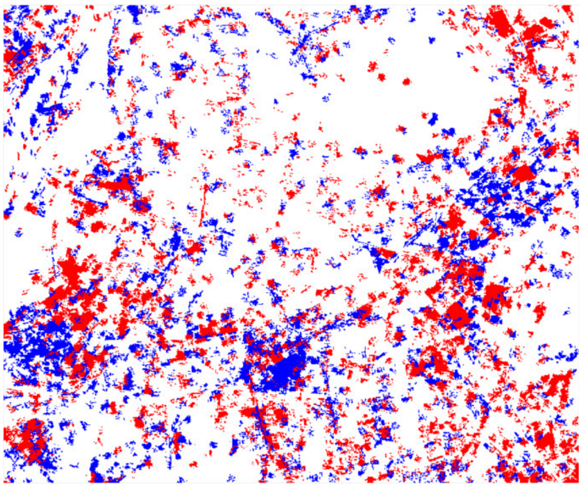

(b) Change mapping results using the NonLocal despeckling filter.

Figure 2.8: Positive and negative changes in Nanjing central urban area, P.R. China, from 2008 to 2013 (positive changes in red, negative changes in blue, no change in white).

Table 2.3: Change detection results using the combination of multiple polarimetric parameters

Grouped Parameters	Superpixel Level		Pixel Level	
	OA/%	Kappa/%	OA/%	Kappa/%
$Surf_{p3}, Dbl_{p3}, Vol_{p3}$	94,03	90,97	93,76	90,62
$Surf_{f3}, Dbl_{f3}, Vol_{f3}$	**97,01**	**95,49**	**94,50**	**91,71**
$Surf_{v3}, Dbl_{v3}, Vol_{v3}$	95,52	93,23	94,18	91,24
$Surf_{y4}, Dbl_{y4}, Vol_{y4}, Hlx_{y4}$	74,63	61,92	75,42	62,93
Vol_{f3}, Vol_{y4}	88,06	81,98	89,73	84,52
$Dbl_{p3}, Vol_{f3}, Vol_{y4}$	**97,01**	**95,49**	**95,22**	**92,81**
$Vol_{v3}, Vol_{f3}, Vol_{y4}$	91,04	86,51	91,60	87,35
Vol_{p3}, Vol_{f3}	92,54	88,73	91,78	87,61
$Surf_{p3}, Dbl_{p3}, Vol_{p3}, Vol_{f3}, Vol_{y4}$	95,52	93,22	93,89	90,80
$Dbl_{p3}, Vol_{f3}, Vol_{v3}$	95,52	93,22	94,27	91,38

In order to understand the impact of the superpixel scale L on the proposed superpixel-based method, a series of ROC (Receiver Operating Characteristics) curves and AUC (Area Under Curve) values have been computed by varying L, separately considering the ability to detect negative and positive changes.

According to the curves in figure 2.9, the most suitable superpixel scale range varies from 20 to 30. The AUC values increase until a scale value of 20. When using larger scale values, e.g., bigger than 40, the AUC values for both positive and negative changes show increasing uncertainties and decreasing performances. This fact confirms that the use of superpixels allows a more accurate charcaterization of local features in SAR images than 4-pixels or 8-pixels neighbourhoods.

2.3.2 2D/3D change detection using Dual-PolSAR SAR

In order to extend the application of the proposed approach, it was tested on dual-polarization SAR data as well. The main reason for this additional test, besides scientific curiosity, is that dual-polarization SAR data (e.g., those by Sentinel-1) are available to the public for free, and already widely used for more standard change analysis.

Unfortunately, not all of the polarimetric parameters that characterize a fully polarized system are available in case of a dual-polarized one. As a result, we analyzed what the performances of the same approach described in the previous paragraphs are, but considering only possible combinations of dual-pol parameters α/entropy/anisotropy (α/H/A) [178].

To this aim, a test case made by a sequence of 4 Sentinel-1 images over the town of Hefei (Anhui province, P.R. China), two of which recorded in 2015, and two in 2017, was

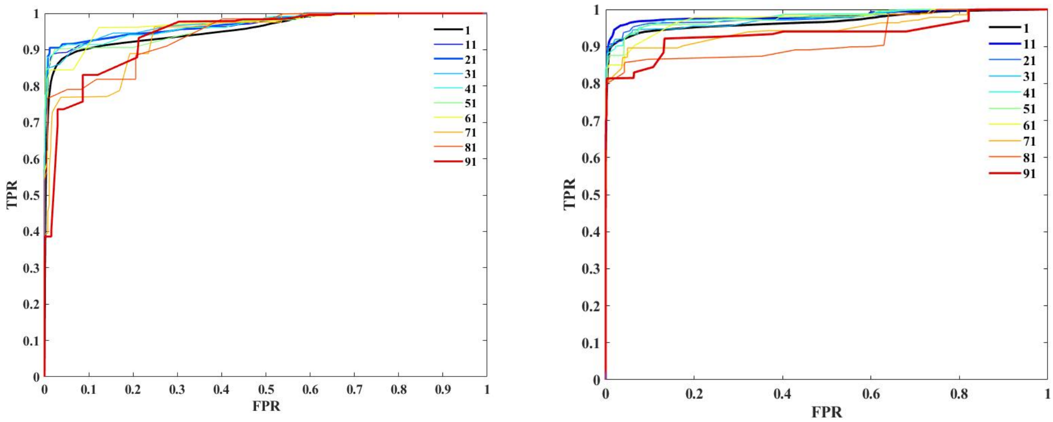

(a) ROC curve for the detection of negative changes (b) ROC curve for the detection of positive changes

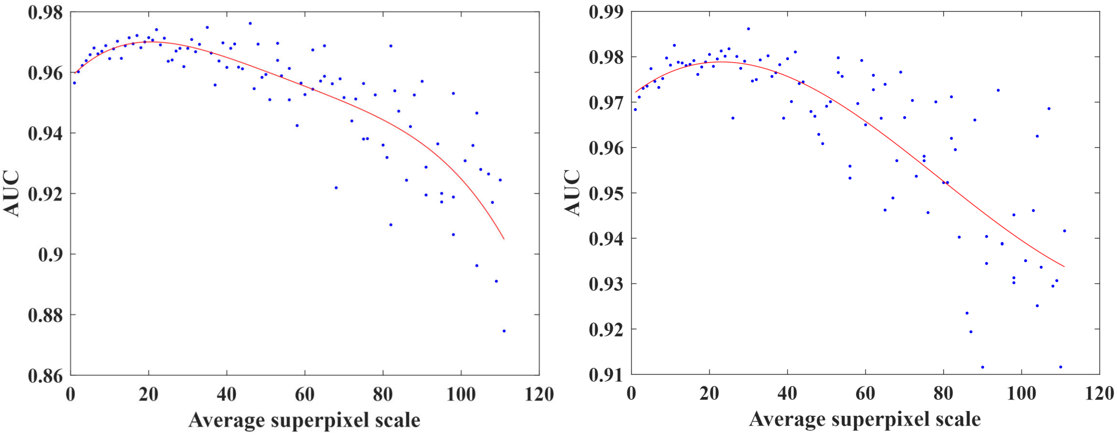

(c) AUC values for the detection of negative changes (d) AUC values for the detection of positive changes

Figure 2.9: ROC curves and AUC values as a function of superpixel scale L.

considered. The adjacent image-pair is used to generate coherence γ data sets, assuming that buildings have not changed in a short time interval. A false-color composition of the VV, VH and VV/VH bands of one of the SAR images, as well as the manually extracted positive/negative/no change ground truth polygons, are shown in Fig. 2.10.

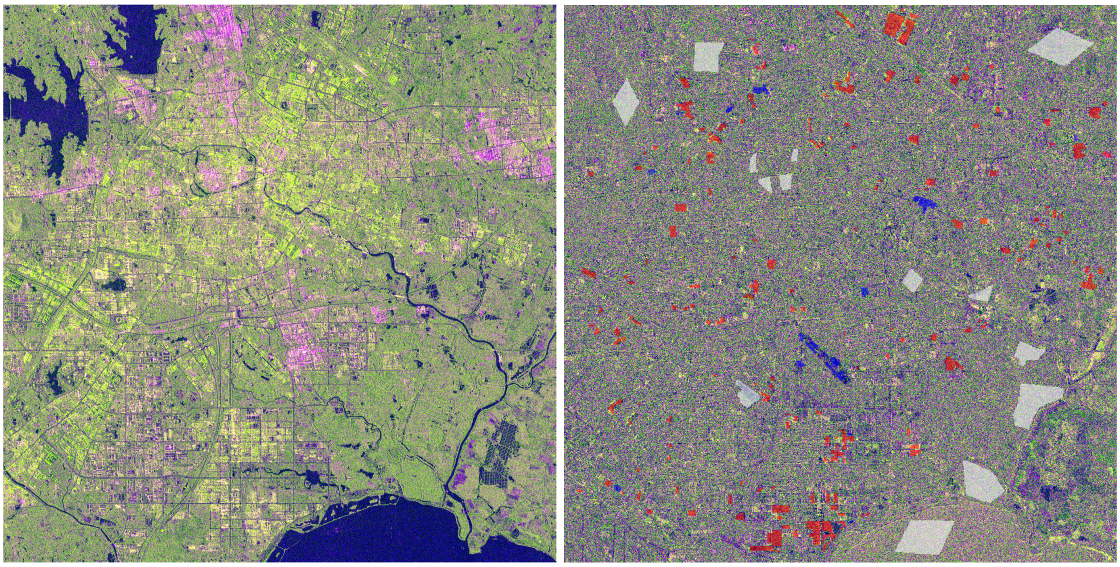

(a) Heifei Sentinel-1 composite SAR image in 2015

(b) Ground truth (Red:positive change, White:no change, Blue:negative change

Figure 2.10: A Sentinel-1 Dual-PolSAR composite image and manually collected ground truth for the city of Hefei (P.R. China).

Because of the reduced polarization information to support polarimetric decomposition, the result is definitely worse than those obtained using a Quad-PolSAR images. The overall accuracy and kappa values obtained by applying the proposed approach to different combinations of polarimetric parameters are shown in Table 2.4, where numbers for results obtained considering a method to mask out non-urban areas are also presented. Specifically, since we found out in the fully polarized case that it makes sense to limit our focus area to human settlements and their surrounding before looking for changes, the second set of results is obtained by masking non-urban areas detected by means of the interferometric coherence computed using the two pairs of images (one in 2015 and one in 2017), and computing a logical OR of the urban area extents extracted from the coherence data for the two dates (Fig. 2.11).

Table 2.4 shows the unsatisfying performance of dual-polarization parameters in detecting 2D/3D building changes even with the use of the “urban mask.”, i.e. by limiting the change detection to the urban area extents in Fig.2.11.

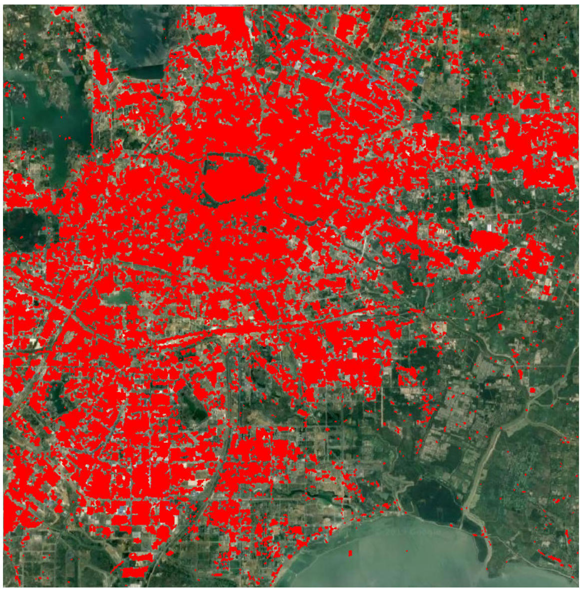

Figure 2.11: Urban extent of Hefei, P.R.China, extracted from S-1 data (in red) superimposed to an S-2 image of the same area.

Table 2.4: Change detection results with and without the use of the urban mask for Hefei

	No urban mask		With urban mask	
Parameter	OA/%	Kappa/%	OA/%	Kappa/%
α	62.61	24.07	72.17	41.26
A	58.26	14.95	70.43	43.13
H	65.65	31.53	72.83	44.76
α,A,H	50.10	23.93	51.20	24.25
I_{vh}	70.87	43.94	78.26	58.78
I_{vv}	59.13	32.4	75.87	57.44
$I_{vv} - I_{vh}$	74.57	46.63	74.57	46.63
$I_{vv} * I_{vh}$	38.48	1.52	57.61	27.15
$I_{vv} + I_{vh}$	58.26	31.19	75	56.06
I_{vv}/I_{vh}	63.7	22.59	70.22	47.25
γ_{vh}	91.54	83.51	91.54	83.46
γ_{vv}	91.79	84.04	92.31	84.94

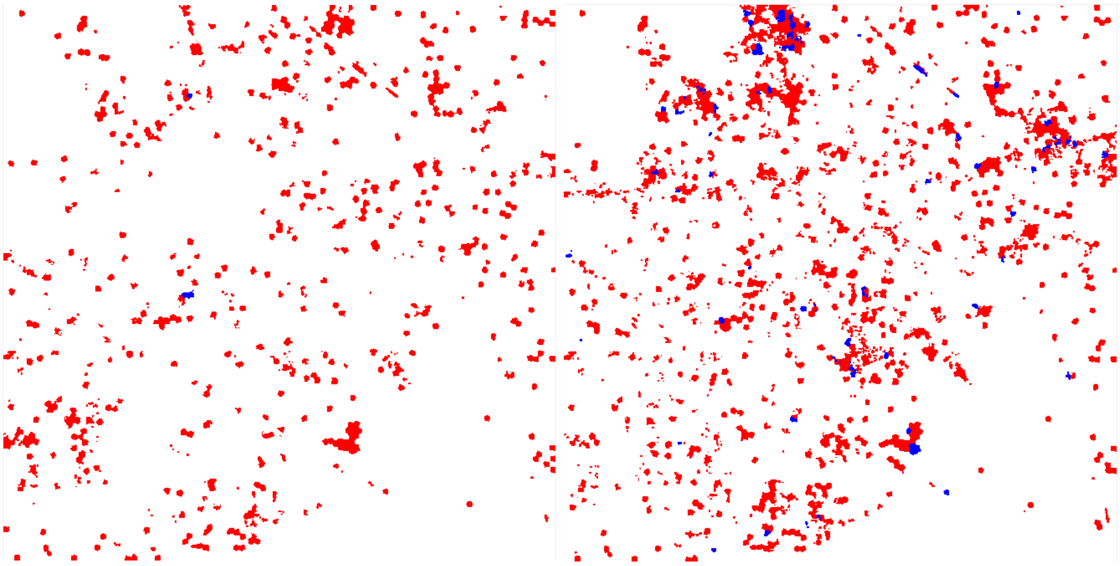

(a) (b)

Figure 2.12: Hefei (P.R. China): change maps obtained using the dual-polarimetry α parameter without (a) or with (b) the use of a urban mask.

The numbers in Tables 2.3 and 2.4 show the dramatic difference between dual and fully polarized images. As a matter of fact, since no parameter directly related to double-bounce scattering mechanisms is available in dual-polarized data, the overall accuracy values are significantly lower for the Hefei test case than for the Radarsat-2 results for Nanjing in [179]. Moreover, it is worth noting that the results in Fig.2.9a, considering only the α parameters, are not able to highlight correctly negative changes. It is also important to stress that the combination of multiple polarimetric parameters (see Table 2.4) does not significantly improve the results. In fact, the overall accuracy values are lower than using a single parameter. Instead, In Table 2.4 and 2.13 the best results are obtained considering temporal coherence γ_{vh} and γ_{vv}, i.e. totally neglecting any feedback from polarimetry.

2.4 Conclusions

In this chapter, an effective and general 2D and 3D urban change detection scheme based on superpixel representation and multivariate GMM is proposed. The proposed method shows the effectiveness of full-polarization features at the superpixel level to describe changes to building density and heights. Therefore, positive and negative changes are easily obtained using a superpixel-wise clustering of selected polarimetric features extracted via polarimetric decomposition. The use of superpixels successfully solves the problematic imbalance between change and no-change components and limits the impact of speckle when measur-

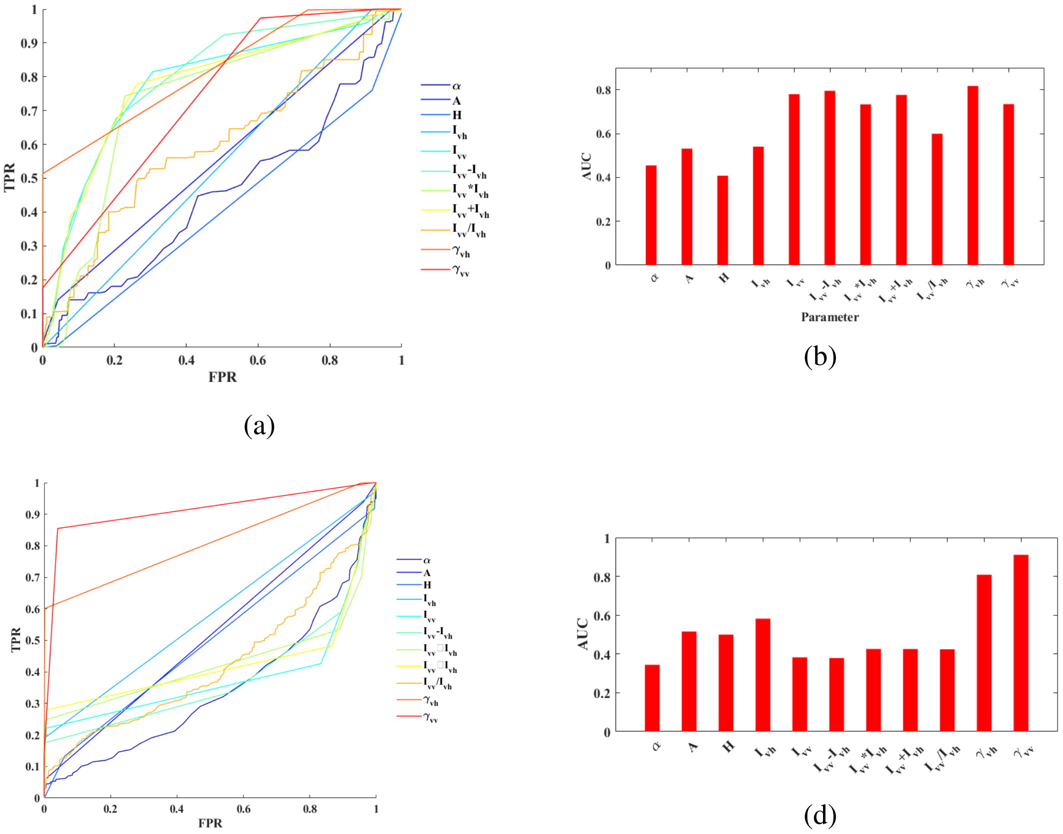

(a)

(b)

(c)

(d)

Figure 2.13: ROC curves and AUC values using polarimetric parameters or temporal coherence: the first row refers to negative changes, the second row to positive changes.

ing the distance between superpixel at different time point. The selection of the superpixel scale is important in ensuring the stability of the segmentation and a more accurate aggregation of locally homogeneous pixels into superpixels.

Unfortunately, the very good results obtained by using double scattering polarimetric parameters are not possible when using dual-polarized data, especially in case of the combination of one cross-polarization channel and one co-polarization channel, because in this case we cannot extract the above mentioned best-performing parameters for urban structural change detection. For dual-polarized images, our preliminary results show that there is no advantage in using polarimetric features as opposed to considering only changes using intensity values of the different polarizations.

In spite of these worse performances using polarimetric features, we found that the joint use of interferometric parameters (i.e., the temporal coherence) and polarimetric or intensity values improves the results. Although at this point we used coherence to limit the change monitoring procedure to the urban extents, these results suggest that the missing features in dual-polarized SAR systems may be substituted by considering temporal information by interferometric processing to detect 2D and 3D changes in urban areas.

Chapter 3

Urban change patterns using SAR time-series

After change pattern exploration in spatial domain using SAR polarimetry proposed in the previous chapter, this chapter turns into time-domain investigations using time-series mining techniques and Dual-PolSAR. It aims at improving the relatively poor results obtained with DualPol data using short yet dense time series. Specifically, time series of SAR intensity and coherence data from Sentinel-1 (with a revisit time close to 12 days) are used to monitor urban change patterns, and discriminate among building maintenance, construction, demolition or reconstruction, as well as among change patterns with (very) different durations along the timeline[1].

3.1 Introduction

Urban areas are constantly changing, and monitoring this change is one of the most important tasks to understand the interaction between humans and the environment. In this sense, change detection and change tracking using temporal sequences of remotely sensed images is becoming essential to keep pace with this task. Indeed, remote sensing allows monitoring urban areas in any place of the world with an unprecedented revisit frequency and spatial resolution, thanks to new satellite platform that provide open and free data sets, such as the Sentinel constellation by the European Space Agency (ESA).

To understand and explain activities affecting urban areas, however, it is necessary to design data analysis techniques capable to recognize a large number of possible transformations, corresponding to different temporal patterns with respect to the spectral and spatial

---

[1] This chapter is based on the work: M. Che, P. Gamba, “Multidimensional Urban Change Detection using Sentinel-1 Temporal Series”, submitted to Geoinfomatica, accepted.

characteristics of human settlements. For instance, for exposure and risk mapping involving human population, it is increasingly important to map urban growth and changes to the urban-rural fringe [165]. However, to understand urban density and discriminate among different land uses, it is also interesting to detect block refurbishments in urban cores [180], as well as urban densification in residential areas [181]. As a matter of fact, there is a recent trend in urban remote sensing to try and detect not only two-dimensional changes, but also three-dimensional ones, because megacities are developing not only by expanding, but also by substituting low-rise buildings with high-rise ones inside urban extent.

With respect to urban monitoring on urban dynamic expansion and urbanization activities, the use of multi-temporal Earth Observation data (e.g., multi-temporal DMSP/OLS [182], Landsat satellite series [183] [184] [185]) makes it possible to have an objective and physically-based approach to recognize urban growth stages and patterns. However, SAR time-series is mostly used to monitor 2D/3D deformation, crustal deformation, subsidence by using techniques of persistent scatterer interferometry (PSI), Small Baseline Subset (SBAS), SAR tomography (TomoSAR) or D-TomoSAR inversion [98] [99] [100] [103] [104]. Together with optical images, SAR amplitude and polarization have been exploited to improve the accuracy of urban landcover classification, and further understand land cover change due to urbanization [60] [61] [62]. However, few researches have been conducted to investigate the trend or change pattern of urban structures using SAR time-series. Up to now, most works are dedicated only to estimate changes caused by sudden-onset disasters.

Accordingly, here we design a novel technique to automatically and contemporarily detect in S-1 repeat-pass data series both the changes to the urban extents, and those inside the urban core due to construction, demolition or completion of built-up structures. This technique provides a complete analysis of the evolution of different portions of urban areas, a basic input to modeling tools for urban meteorology, hydrology, micro-climatology, and citizen health.

3.2 Change pattern recognition from coherence and intensity series

To cope with the objectives described above, the procedure proposed in this chapter comprises two different parts, each one realized by a specific processing chain and more accurately described in the following subsections. Indeed, a procedure trying and solving the overall problem of urban change detection, and able to discriminate among different change patterns, should be on the one side able to track changes to the urban extents, and on the other side to understand changes due to upgrades of the built-up/recreational areas

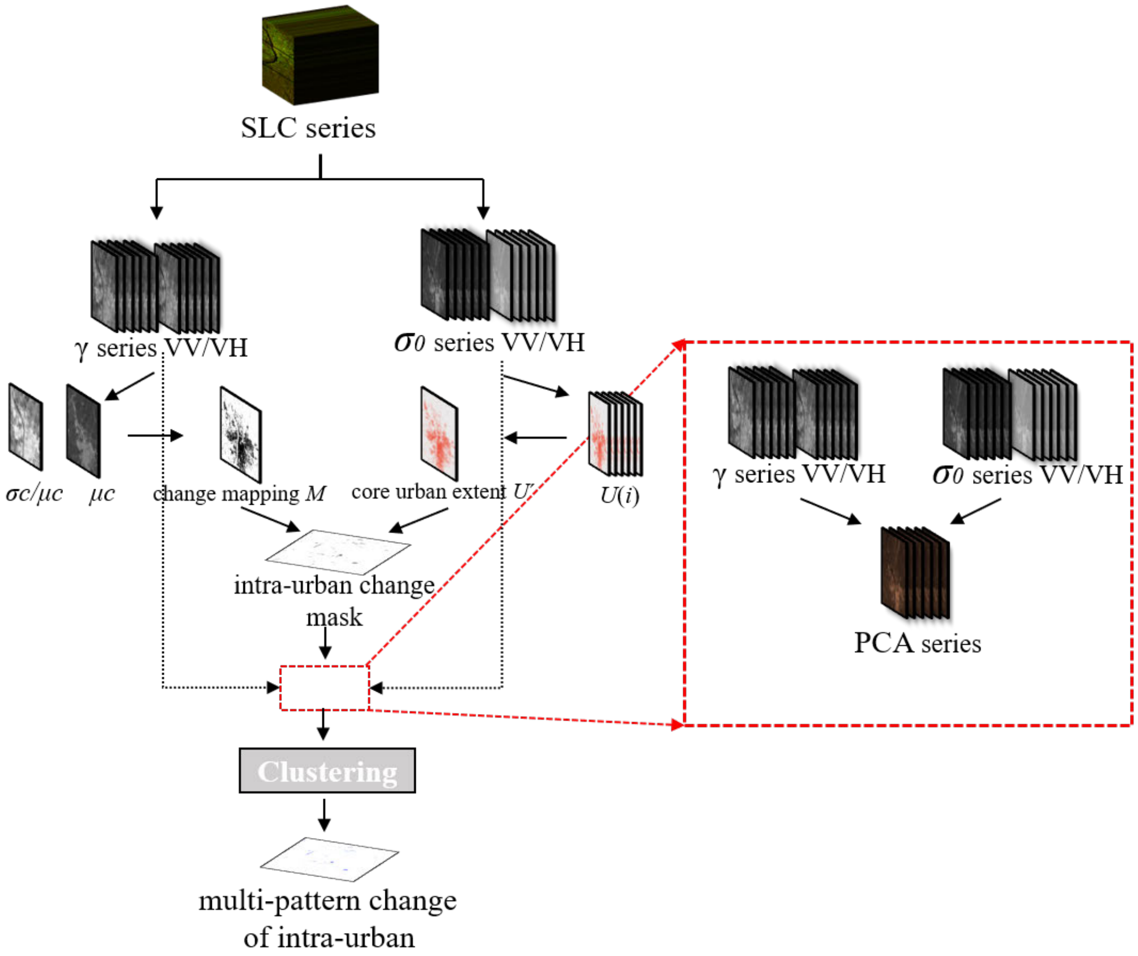

Figure 3.1: A graphical representation of the overall workflow of the procedure described in this work, highlighting the two main parts of the approach, i.e. the mapping of urban extents using SAR amplitude, as well as the detection of change patterns at the urban fringe and inside the urban core using both SAR amplitude σ_o and InSAR coherence γ.

(e.g., because of roof reconstruction for old buildings), as well as the enlargement or upgrade of specific built-up elements. Examples are the change in the number of floors for a single building, or the change of a residential area block from traditional to more modern buildings. The approach presented in [186] has been specifically developed to map urban area extents from S-1 data, with encouraging results. It can be thus used to map, image by image and time frame by time frame, the urban area extents, as well as to compute the changes from one date to the following one.

To discriminate among different change patterns, a mask consisting of the areas consistently mapped as "urban" is obtained by a logical AND among the urban extents extracted from the temporal series of SAR amplitude data $\Sigma^P = \{\sigma_1^P, \sigma_2^P, \sigma_3^P, ..., \sigma_n^P\}$, while the rest of these urban masks is aggregated into a map of locations that, at some point during the analyzed period, have transitioned from a "non-urban" to the "urban" class. While the former map identifies areas consistently within the urban core, the latter one allows a temporal reconstruction of the outbound dynamics and growth of the whole urban area.

The second part of the procedure aims at a better understanding of the dynamics of the urban core, recognizing that, as mentioned in the introduction, there are a number of changes that do not result into a change in the urban extents, but rather in a difference in the backscattered electromagnetic field. It is reasonable to guess that this change can be detected looking at the temporal series of amplitude values, but a different, and possibly more sensitive, measure of the same effect may be achieved by using a temporal series of the interferometric coherence between two temporally adjacent images. The interferometric coherence value is stable in areas with artificial structures that do not change [187], while it undergoes strong variations in case of a change in built-up structures [188]. The standard deviation σ_c of the sequence of coherence values along time for each pixel is an indicator of its temporal stability or change at the corresponding location in the scene. Accordingly, σ_c may be used to discriminate between urban blocks that did not change and those that were subject to constructions, demolitions or renovations. The latter group can subsequently be better characterized by looking at the temporal patterns of the average coherence values in each block. These patterns are clustered in three classes, expecting to catch the above-mentioned three types of changes, e.g. an increase in coherence due to constructions, a decrease due to demolitions, and a more variable pattern in case of renovations or transformations.

A graphic representation of the overall procedure is provided in Fig. 3.1, where the area with a large standard deviation in the temporal coherence is labeled as "change mask", while its intersection with the area that is consistently mapped as "urban" using the amplitude image is labelled as "image change map'.

3.2.1 Urban extent series extraction and analysis

As mentioned above, once the Single Look Complex (SLC) SAR series $Z = \{z_i | i = t1, t2, ..., tn\}$ has been collected, the method reported in [167] is used to extract urban extents, labeled $U_i, i = 1, \ldots, N$, where N is the number of intensity of the stack, generated from Z. The approach is based on the backscattering effect of built-up structures, the so called "double bounce effect", which makes the amount of power backscattered from built-up areas particularly large. More specifically, and referring the interested reader to [167] for all the details, the main processing is structured in three steps after speckle denoising with a Lee filter.

1. **Seed extraction**: starting from the averaged backscattering coefficient in the SAR sequence, a limited number of points with very high backscattered power are selected, assuming that they correspond to very strong backscatterers due to artificial structures. This step is performed using a threshold that depends on the number of SAR images in the stack.
2. **Pixel aggregation**: other strong scatterers that are spatially close (in all directions) to the seeds are iteratively aggregated to the clusters, growing them into a more and more refined approximation of the urban extents. This step is performed considering a second lower threshold, that depends on the average backscattering value in a large area around the seeds.
3. **Post-processing**: the extracted extents are refined considering a digital terrain model (e.g., the SRTM DTM). Specifically, seeds and urban extents in areas with steep slopes are discarded.

Although this approach has already proved to be accurate enough for most applications, has been refined to be used for S-1 [186], and works irrespectively of the geographical location of the urban area under analysis, it is still subject to errors due to the noise, as well as in the changes in the viewing angle of the sensor. To reduce these negative effects, and taking into consideration the fact that there is a sequence that can be exploited, two types of temporal filters are applied to the urban extent masks. The first filter is based on majority principle, and validates an urban or non-urban pixel by looking at its value in the current urban extent mask and the two temporally adjacent masks. The second filter assumes that urbanization is irreversible along the timeline and validates the "urban" label only if it is confirmed by previously assigned urban labels in the same location.

After extraction and post-processing, the urban area extents $U_i, i = 1, \ldots, N$ are aggregated into two different maps. The first one, obtained by means of a logical AND among all maps in the temporal series, identifies the "urban core", i.e. the area that, in the considered period, is always classified as urban. The second one includes the complementary information, i.e. areas that have been gradually added to the urban core along time. This map depicts, with different colors according to the date, the changes in the urban-rural fringe, providing a quantitative and visual description of the urban growth and its direction(s). An example of these two maps for the city of Changsha, P.R. China, is presented in Fig. 3.4.

3.2.2 Interferometric coherence time-series

As mentioned above, although an analysis based on amplitude values and their spatial patterns is able to detect urban area extents, the use of temporal SAR series allows considering interferometric processing, too. As a result, and following what has been considered in technical literature since quite a few years [187], interferometric coherence maps are computed and eventually utilized to include additional information for change detection. In this chapter, once all the images of the temporal series are co-registered with one master image like for the usual interferometric processing, only adjacent co-registered interferometric pairs are processed to generate a series of coherence values. Specifically, coherence γ_c between t_1 and t_2 is computed in a $m \times n$ window according to the following formula:

$$\gamma_c(x,y) = \frac{\left|\sum_{i=1}^{m}\sum_{j=1}^{n} Z_{t_1}(x_i,y_j) Z_{t_2}^{*}(x_i,y_j)\right|}{\sqrt{\sum_{i=1}^{m}\sum_{j=1}^{n} \left|Z_{t_1}(x_i,y_j)^2\right| \sum_{i=1}^{m}\sum_{j=1}^{n} \left|Z_{t_2}(x_i,y_j)^2\right|}} \tag{3.1}$$

where $Z_{t_1}(x_i, y_j)$ and $Z_{t_2}(x_i, y_j)$ are the master and slave Single Look Complex (SLC) values recorded at time t_1 and t_2, respectively. The series of coherence values for each polarization is given by $\Gamma^P = \{\gamma_1^P, \gamma_1^P, \gamma_1^P, ..., \gamma_n^P\}$, where P is the polarization ($P = \{vv, vh\}$). As proved in [189], any source of decorrelation decreases the coherence between an image pair. More specifically, decorrelation may be due to the time difference (e.g., changes in the spatial distribution of scatterers or their electrical characteristics along time), the difference in the geometry acquisitions (e.g., changes in the viewing angle), a change in the surface (e.g., because of deformations), or the difference in atmospheric contents. By computing the coherence only between two temporally adjacent repeat-pass images, the intent is to constrain the effect of temporal and geometry decorrelation to single out as much as possible the component caused by human activities.

To this aim, the average value μ_c and standard deviation σ_c of the sequence of coherence values along time are computed. Then, a stack composed of the ratio σ_c/μ_c and the μ_c value is used to discriminate, using the Otsu threshold method on either band and a logical AND, between areas with small and areas with large variations of the coherence in time with respect to its average value. The pixels belonging to the latter class most likely correspond to areas that underwent a significant change during the period of interest. If they are located inside the“urban core” a, they presumably identify changes in the built-up. The remaining part of the urban core map, instead, is labeled the “urban unchanged map”, and contains locations that are stable both in terms of the SAR amplitude (because they belong to the urban area for all the dates there were analyzed) and of coherence.

The final processing step is a clustering analysis within the changed portion of the urban core, performed by a simple combination of the PCA and K-means algorithms applied to the coherence and amplitude sequences together. Specifically, the two series of coherence values for the VH and VV polarizations, as well as the two series backscattering coefficient σ_0 for both the same polarizations, are reduced into one univariate series by PCA, which is dedicated to solve the curse of dimensionality [190], and whose outputs are set as inputs to the clustering procedure performed by K-means. The idea is to cluster urban locations with respect to the temporal patterns of both coherence and amplitude. The final identification step, that assigns these clusters to peculiar changes that affected the urban core, is performed manually, by visually analyzing these patterns in locations that have been assigned to each cluster.

3.3 Experimental results

The above- mentioned approach has been tested using S-1 data sets over the two cities of Changsha and Hangzhou in P.R. China and one metropolis, Lombardy Region in Italy. The main reason for the selecting of two cities is in the fast growing status of these two cities, which produces both a wide expansion of the urban extents, and a renovation of several portions of the inner core of both urban areas. We expected these two cities to provide enough examples of different behaviors with respect to changes in amplitude and coherence to allow understanding the advantages and describing the shortcomings of the proposed technique. And the selection of Lombardy is aiming to validate our approach in most developed areas of very low, even stagnant urbanization.

3.3.1 Case 1: Changsha, P.R.China

The city of Changsha is located in the Hunan Province of the P.R. China. Being the core area of Changsha-Zhuzhou-Xiangtan urban agglomeration, Changsha is a typical inland city experiencing a rapid urbanization. Specifically, the urbanization level has reached 64% at the end of 2015 [191]. To study this area, 30 IW Interferometric Wide Swath mode (IW) single look complex (SLC) SAR images, from May 2016 to October 2018, were considered. Coherence and backscattering coefficient series for both the VH and VV polarization were extracted. No digital terrain model was used to improve the urban extent extraction because the test site is in a flat area. A false color S-1 image for Changsha is shown in Fig. 3.2, together with an optical image at a close date.

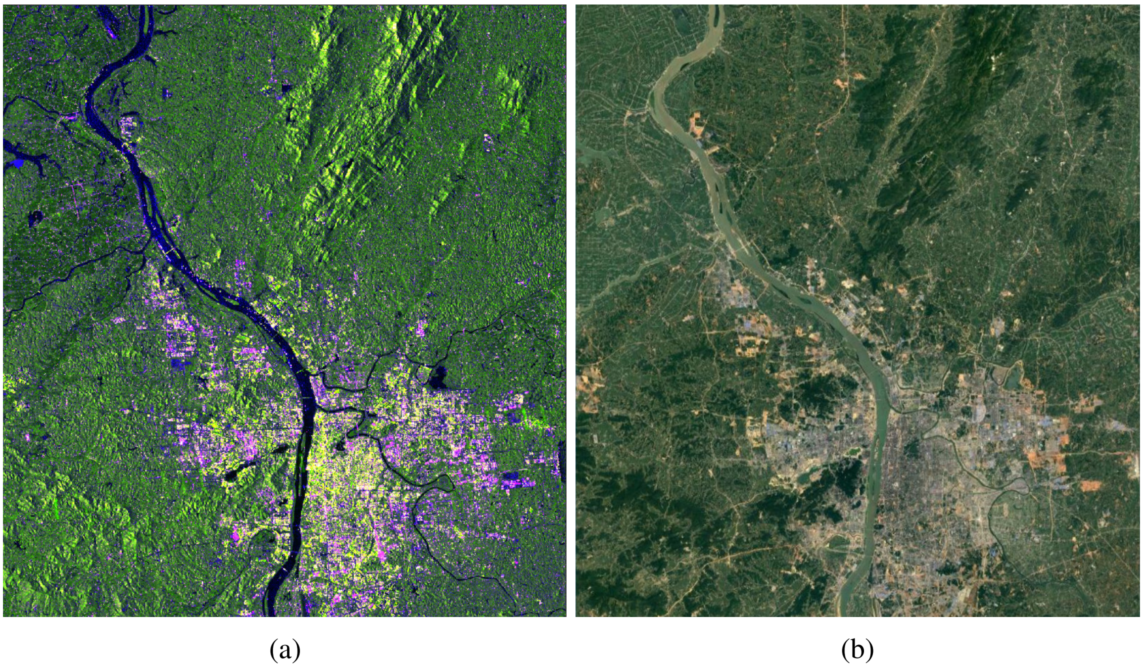
(a) (b)

Figure 3.2: Changsha test site: (a) S-1 June 2016 SAR false color image using VV, VH, VV/VH; (b) Optical image in the same period.

The interferometric processing for the whole SAR data series was performed considering the image in Sept. 2017 as the master, and the temporal and perpendicular baselines [192] are reported in Fig. 3.3. Note that the master image selection is selected in order to minimize the effect of geometry decorrelation.

As mentioned above, the first part of the procedure is meant to extract the urban extents from each of the 30 images in the S-1 sequence, which are subsequently edited using the two temporal filters mentioned in the previous section. Eventually, the series of urban extents are merged into a map of the human settlement which has been always mapped as such in all images, and a map of the temporal changes along the considered timeline, both reported in Fig. 3.4.

Following the proposed algorithm, inside the area identified as the urban core by the amplitude analysis, an additional binary discrimination is performed using the coherence time series (29 coherence images) to detect portions that underwent a large coherence variation, hence suggesting that some kind of changes has been experienced. The results, for the portion of Changsha highlighted by a white rectangle in Fig. 3.4, are reported in Fig. 3.5(b),

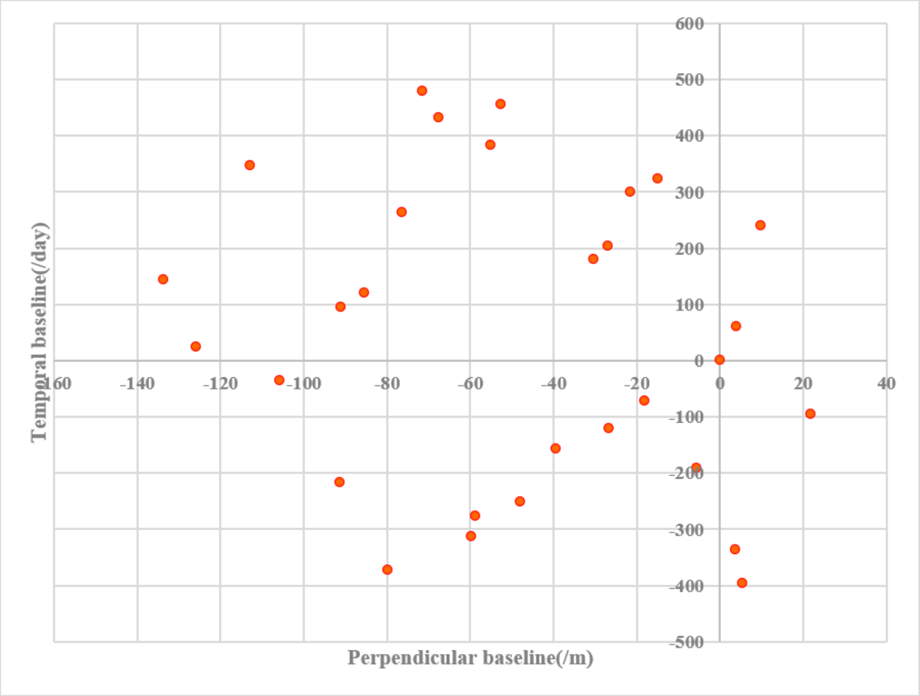

Figure 3.3: Temporal baselines (in days) and perpendicular baselines (in meters) for the S-1 sequence over Changsha, considering the image in Sept. 2017 as a refernce.

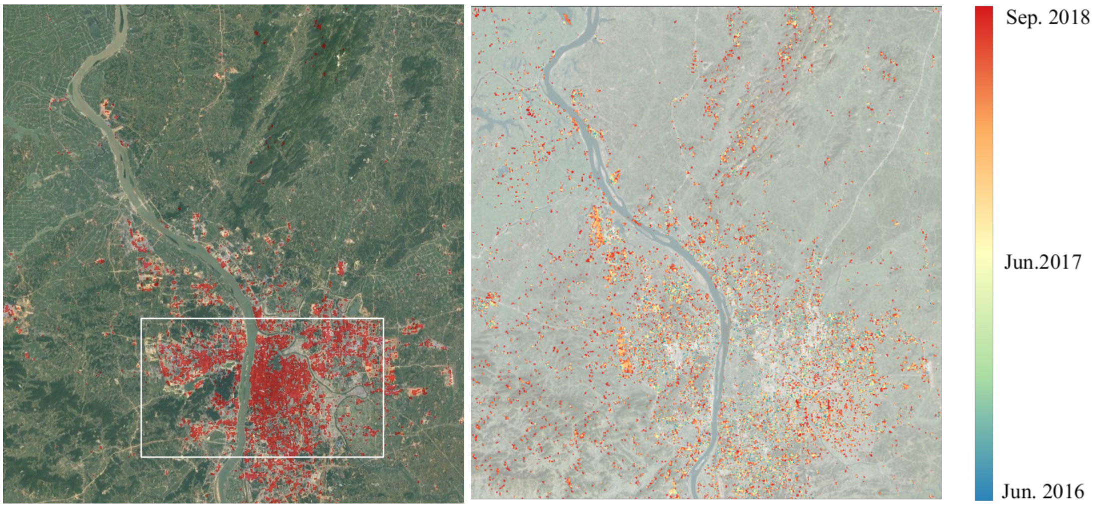

(a)

(b)

Figure 3.4: Changhsa test site: (a) urban core map; (b) areas that have become urban along the same timeline (the blue to red legend marks less to more recent changes). The area identified by a white rectangle is the one considered for further, more detailed analyses in the next figures.

while Fig. 3.5(a) shows the input data to this binarization, i.e. the ratio between the standard deviation and the average of the coherence in time for each location. To validate the changes inside this area, the change map is transformed into object patches and checked versus a visually extracted ground truth (see Table 3.1). The reported overall accuracy is 80.85%, with a $\hat{\kappa}$ of 0.617.

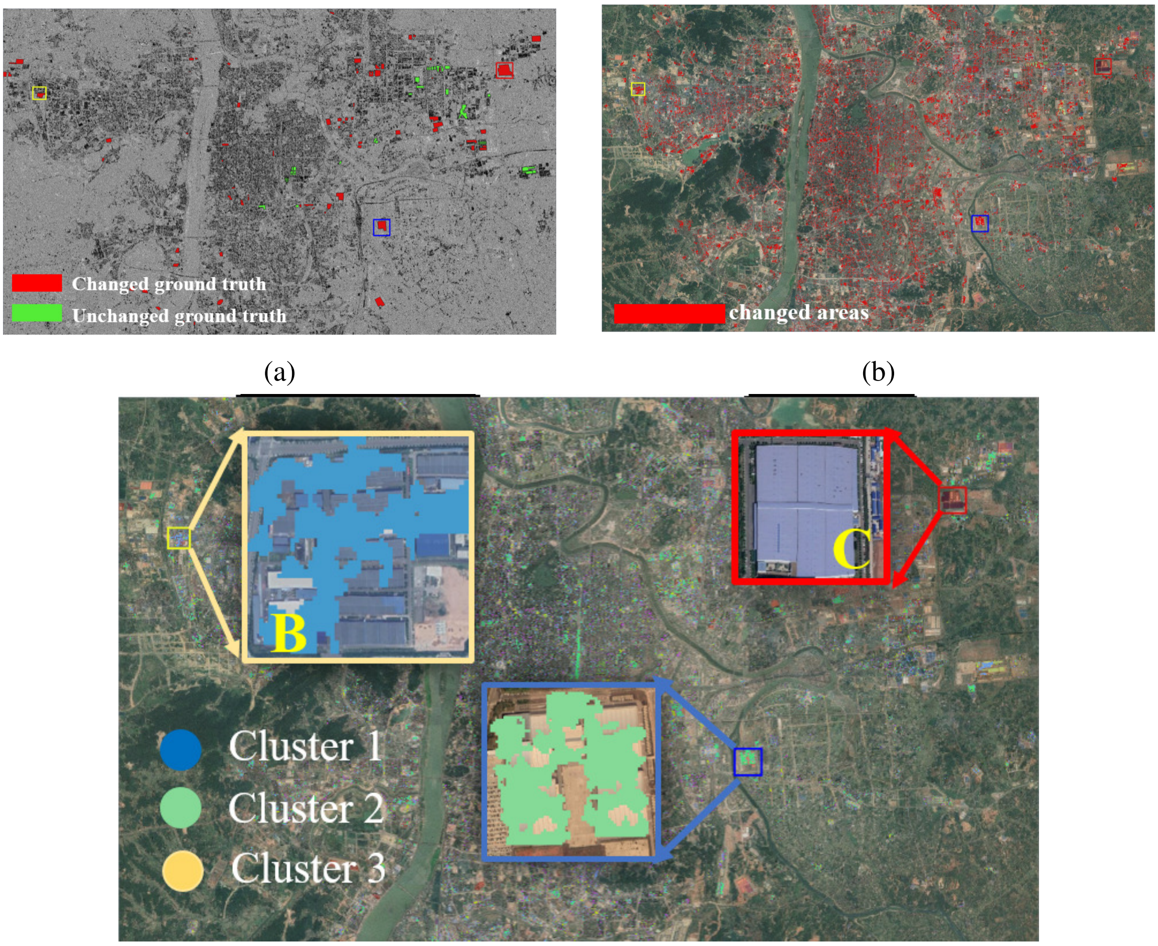

(a) (b)

(c)

Figure 3.5: The portion of the Changsha test site identified by a white rectangle in Fig. 3.4: (a) ratio of standard deviation to the average value of the coherence stack; (b) areas identified as changed areas inside the urban core; (c) results of the temporal clustering. The resulting three clusters are identified by the blue, yellow and green colors.

Eventually, temporal clustering is implemented on the coherence time series for this area. The results of this clustering analysis, performed considering three classes, are provided in Fig.3.5(c), where three patches, two of them selected to represent changed areas, and one an area that did not change, are identified by differently colored squares and by the letters **A**, **B** and **C**, respectively.

Table 3.1: The confusion matrix for the object-based validation of urban changes inside urban core of Changsha

		Ground truth		
		Changed	Unchanged	Producer accuracy (%)
Classifier results	Changed	80	13	86.0
	Unchanged	23	72	75.8
	User accuracy (%)	77.7	84.7	

Table 3.2: The object-based validation on changes of growth over Changsha

		Ground truth		
		Changed	Unchanged	Producer accuracy (%)
Classifier results	Changed	26	4	86.67

To understand the semantic meaning of the clusters, the temporal behaviors of the coherence and amplitude average values for the selected patches are reported in Fig. 3.6 and 3.7. Patch **A** identifies an area where partially completed constructions were initially located, but these buildings were completed during the selected time frame. Patch **B** presents a similar construction project, while patch **C** is an unchanged building. As visible in the graphs reported in Fig. 3.6, for the first patch a significant change of the coherence series is clear, because of the building under construction and unfinished, while this is absolutely unapparent while observing the backscattering amplitude series. The same comment is valid for the second patch, where changes can be detected by looking at the coherence but not to the amplitude series. Finally, the third patch proves that, in case of an unchanged building, both the coherence and amplitude values remain stable and large. For validation purposes, three multispectral images, at the beginning, the end and in the middle of the time period, respectively, are provided for each of the test sites in Fig. 3.6(c,f) and Fig. 3.7(c).

As a comment, in the Changsha case study it is found that the coherence is more sensitive than the backscattering coefficient to changes to the 3D structure of urban elements. The amplitude sequences, instead, do not allow to understand the changes, and present a significant difference in the scattering level between the VV and the VH polarization. This result stresses the fact that combining coherence and amplitude information unearth more change patterns, because coherence reflects deformations, (re)constructions, and 3D changes, while the amplitude depends on the spatial (i.e. 2D) configuration of the dihedral structures.

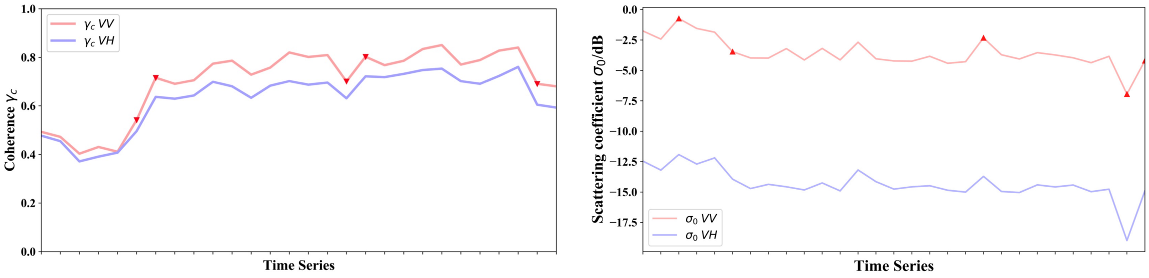

(a) Patch **A**: Coherence Series (b) Patch **A**: Amplitude Series

(c) The temporal evolution of patch **A**

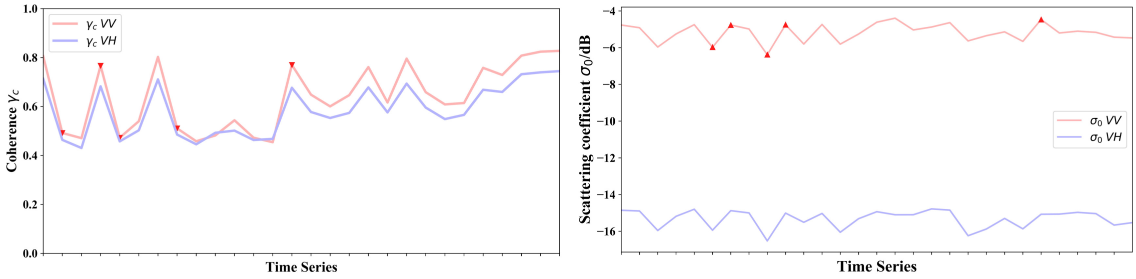

(d) Patch **B**: Coherence Series (e) Patch **B**: Amplitude Series

(f) The temporal evolution of patch **B**

Figure 3.6: The trend of the average coherence and backscattering amplitude coefficients for the patches A and B identified in Fig.3.5, to be checked against optical images for validation purposes. The two curves in red and blue refer to the two polarizations of S-1 data.

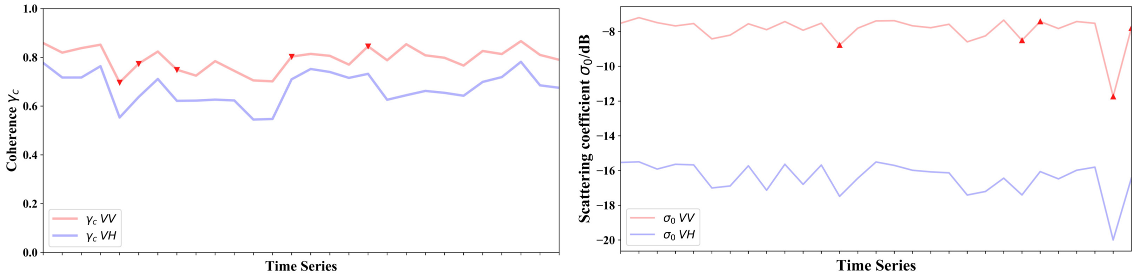

(a) Patch **C**: Coherence Series (b) Patch **C**: Amplitude Series

(c) The temporal evolution of patch **C**

Figure 3.7: The trend of the average coherence and backscattering amplitude coefficients for patch C identified in Fig.3.5, to be checked against optical images for validation purposes. The two curves in red and blue refer to the two polarizations of S-1 data.

3.3.2 Case 2: Hangzhou, P.R.China

The second test site is the city of Hangzhou. Located in the eastern coastal region of P.R. China, Hangzhou is the capital of the Zhejiang Province, and expanded by 5 times from 1986 to 2001 [193]. 74 IW SLC SAR images from November 2015 to October 2018 were selected and considered for this test area. The first one in the sequence of S-1 images used in this work is depicted in Fig. 3.8, together with an optical image for the same period. Like for the previous test case, no digital terrain model was used to improve the urban extent extraction because the test site is in a flat area.

Table 3.3: The confusion matrix for the object-based validation of urban changes in Hangzhou.

		Ground truth		
		Changed	Unchanged	Producer accuracy (%
Classifier results	Changed	131	11	92.3
	Unchanged	28	85	75.2
	User accuracy (%)	82.4	88.5	

The Hangzhou urban core area, with highlighted the results of the clustering procedure after using the temporal series, is depicted in Fig. 3.9, where three patches, like for the pre-

(a) (b)

Figure 3.8: Hangzhou test site: (a) S-1 June 2016 SAR false color image using VV, VH, VV/VH; (b) Optical data image for the same period.

Table 3.4: The object-based validation on changes of growth over Hangzhou.

		Ground truth		
		Changed	Unchanged	Producer accuracy (%)
Classifier results	Changed	27	3	90.0

vious test site, have been extracted. The corresponding coherence and amplitude time series are reported in Fig. 3.10, showing that the first (blue) patch is an area subject to demolition of old buildings, as visible from the decrease in the temporal series of the coherence and the amplitude values, the second (green) patch is a construction site with buildings that were originally partially built and the third (yellow) one is a totally new construction site. The difference between the last two patches is clear looking at the amplitude series, that does not present any significant trend in the first case, while it shows an increasing trend in the second one.

Like for Changsha, a validation was performed. The results are shown in Table 3.4 with an overall accuracy of 84.71% and a $\hat{kappa}$ of 0.685. Erroneous identifications correspond to areas where the coherence temporal pattern is not significantly different from the "no change" case. This problem may be reduced by using more clusters than just three as in our tests. These misclassifications are also dependent on the extension of the changed area, as the analysis is performed on the average coherence and amplitude patterns in an identified patch.

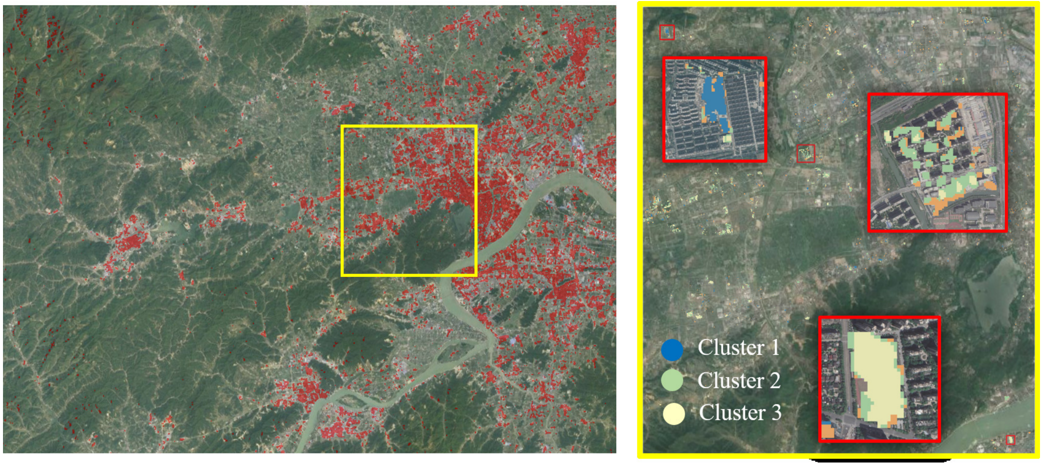

Figure 3.9: Hangzhou test site: the urban core area (on the left), a smaller area where clustering results are reported (on the right), inside which three patches (in blue, green and yellow) are identified.

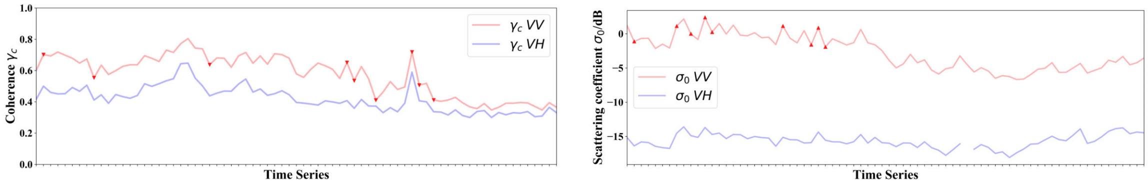

(a) Blue patch: Coherence Series (b) Blue patch: Amplitude Series

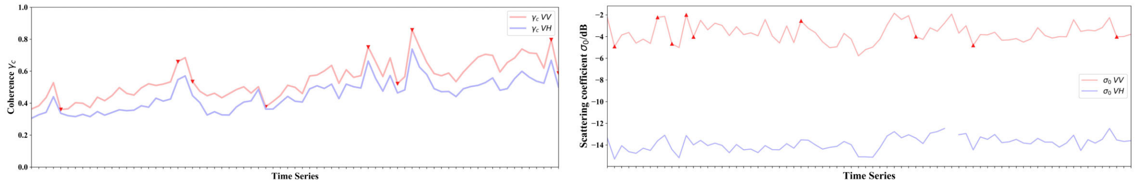

(c) Green patch: Coherence Series (d) Green patch: Amplitude Series

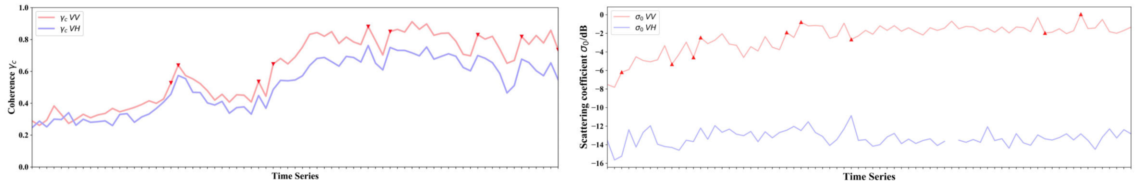

(e) Yellow patch: Coherence Series (f) Yellow patch: Amplitude Series

Figure 3.10: The trend of the average coherence and backscattering amplitude coefficients for the three patches identified in Fig. 3.9 for the Hangzhou test site (the two curves in red and blue refer to the two polarizations of S-1 data).

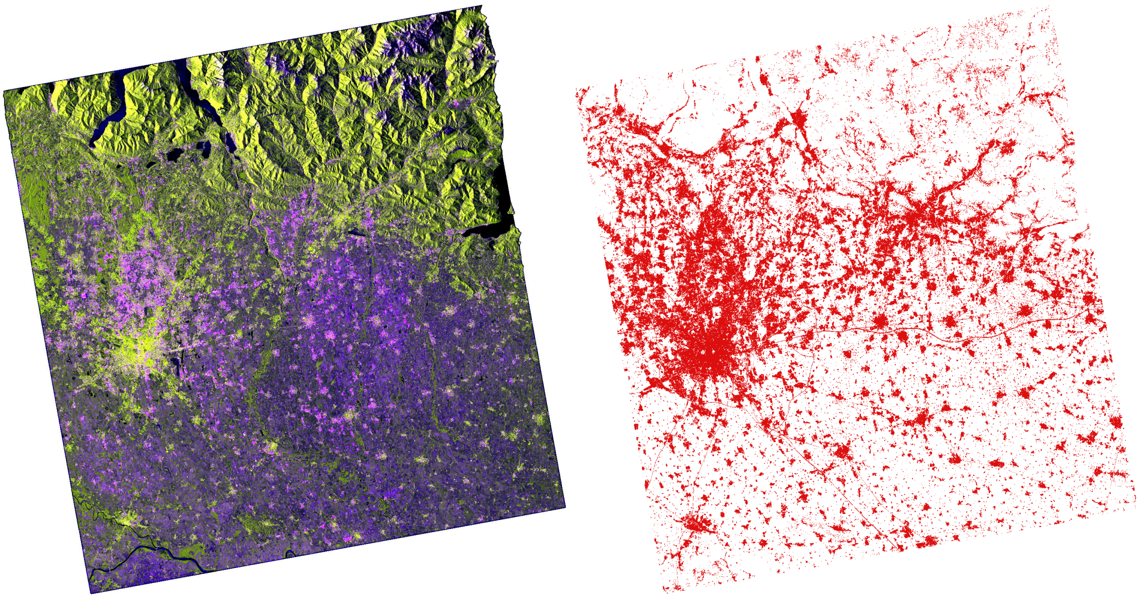

(a) (b)

Figure 3.11: Lombardy region: (a) Sentinel-1 composite image; (b) Greater Milan urban area extent.

3.3.3 Case 3: Lombardy Region, Italy

Lombardy is most developed area in Italy, with a population of about 10 million and urbanization of above 70.4% in 2018. This area is selected to know if the approach is valid to highly urbanized areas. Therefore, 47 IW Interferometric Wide Swath mode (IW)single look complex (SLC) SAR images, from May 2017 to November 2018, were collected. Coherence γ_c and backscattering coefficient σ_0 series for both the VH and VV polarizationswere extracted.

Eventhough few changes can hardly be mapped in this highly-urbanized areas, certain locations of commercial and corporate building blocks still are detected as shown in 3.12 and 3.13. Both patches present a complete process of buildings being under construction with the same time series trends: increasing backscattering coefficient and low coherence (below 0.5).

3.4 Conclusions

This chapter describes a technique to exploit temporal sequences of S-1 data, and extract information about changes around and inside urban area. Specifically, the proposed approach is able to catch the urban growth by mapping accurately the changes to urban extents. It

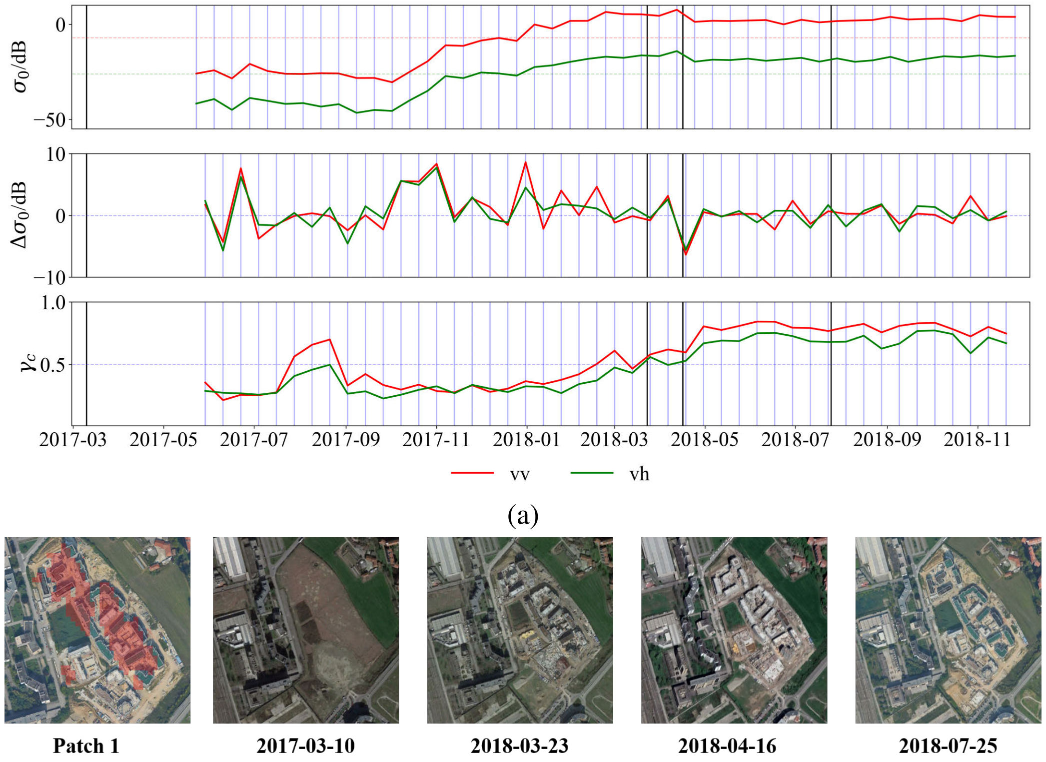

(a)

(b)

Figure 3.12: Time-series analyses of selected patch 1: (a) time-series analyses of backscattering σ_0, difference $\Delta\sigma_0$,coherence γ_c; (b) validation with Google Earth images at timelines marked in black.

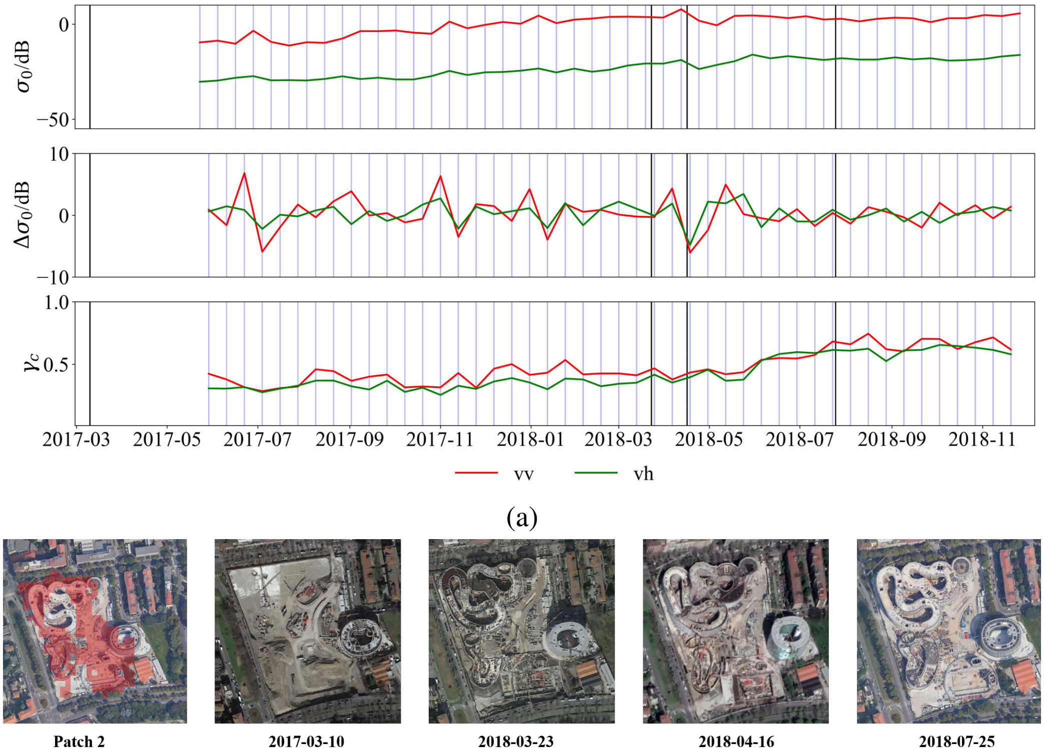

(a)

(b)

Figure 3.13: Time-series analyses of selected patch 2: (a) time-series analyses of backscattering σ_0, difference $\Delta\sigma_0$,coherence γ_c; (b) validation with Google Earth images at timelines marked in black.

is also capable of detecting changes due to constructions, renovations and demolitions exploiting the temporal series of interferometric coherence values, eventually resulting in a more accurate understanding of the changing urban landscape.

With respect to the change or trend recognition, the results in all test sites confirm that there are differences between the coherence and the backscattering coefficient patterns, but minor distinction between VV and VH polarization. The coherence series provides a far better temporal characterization than the amplitude series, but the high correlation between coherence values for VV and VH polarizations makes them somehow redundant. Accordingly, as far as this research, the benefit from the use of multiple polarization is limited.

The approach has been validated considering two fast growing cities in P.R. China, that are experiencing many different urban change patterns, captured by the short revisit time rand the fine spatial resolution of S-1 data and the much more stable area of Lombardy, northern Italy. Our tests have proved that:

- the proposed approach allows characterizing purely two-dimensional effects, such as the growth of urban extents and mixed two- and three-dimensional changes insider the inner part of human settlements;
- by jointly exploiting amplitude and coherence data from high temporal and spatial resolution S-1 data sets it is possible to recognize and discriminate among more types of changes in the inner core of urban areas.

A possible future line of research could be the (semi)automatic selection of semantic labels for the change patterns that are obtained as output of this approach, as well as the combination of this approach with other 2D/3D change detection technique based on scatterometer and nighttime data.

Chapter 4

Multi-pattern change exploration using data from heterogeneous sources

The second part of this thesis is devoted to detect and visualize intraurban changes by jointly exploiting Sentinel-1 (S-1) SAR data and nighttime light data, in the form of change vector analysis. By extracting urban extents and urban density maps from SAR data, changes in nighttime lights intensity can be used to detect changes related to the level of activity in a specific portion of each urban areas. At the same time, changes in radar backscattering are prone to reveal changes in the two- and three-dimensional structures of the built-up. The combination of these multimodal datasets has already proved to be useful to discriminate urban change patterns at the city level. In this chapter, further and different intra-urban changes are extracted. Experimental results focus on fast-growing (mega) cities in East Asia, allowing us to understand in a more detailed way how they are changing and evolving in all three dimensions. Examples for Nanjing, Shanghai, and Guangzhou (China), Saigon (Vietnam), and Vientiane (Laos) are discussed to prove this statement[1].

4.1 Introduction

The urgent need to monitor urbanization at the global level, but especially in South and East Asia, is the main driver for the recent advances in urban extent mapping from earth observation, initially performed at a single point in time, and more recently at multiple dates. This need is the main reason, for instance, for the multi-temporal global human settlement layer [194], [195], as well as the recent additions to the global urban footprint dataset [196], both focusing on the extraction of urban extents by means of multispectral

---

[1] This chapter is based on the work: M. Che, P. Gamba, “Intra-urban change analysis using Sentinel-1 and nighttime light data”, IEEE J. of Selected Topics in Applied Earth Observation and Remote Sensing, vol. 12, no. 4, pp. 1134-1142, April 2019.

sensors for past years, and multispectral and/or radar sensors for the more recent ones. In this sense, the future looks bright, thanks to the availability for free of multispectral and radar datasets by the Sentinel constellation, already considered in many papers applied to urban remote-sensing applications

In this chapter, the stress is on the possibility to further exploit the Sentinel datasets, in conjunction with other data that have been traditionally used for urban remote sensing, i.e., the nighttime lights [197]. Urban extent layers and sophisticated approaches for urban extent extraction using SAR Sentinel-1 (S-1) [186] or multispectral Sentinel-2 (S-2) [198] data are already available. This paper aims at making a step further, and understand which changes would be possible to detect and recognize inside these urban extents, i.e., at the intra-urban level. Accordingly, "intra-urban changes" correspond to changes to the urban structure that happen in locations that are classified as "urban" for the whole analyzed time period.

Indeed, although in the last years there have been papers devoted to urban extent monitoring, only recently more attention has been dedicated to detecting the changes in the two- and three-dimensional structure occurring inside urban areas around the world. The works in [199] and [200], for instance, describe the patterns due to the change of the power of return by microwave scatterometers in urban (and suburban) areas, extracting hints about the spatial patterns and structural features of different urban environments. A similar approach has been applied in [201], adding to the power of return changes the nighttime light intensity changes, to recognize temporal patterns in 100 cities around the world. However, since scatterometer data allow to analyze trends in volumetric changes, but do not have enough spatial resolution to map the expansion of human settlement, fusion of information from other sensors is still required to map urban areas "up and out." For instance, this issue is solved in [202] by using multispectral data, in addition to scatterometer and nighttime light measures.

In this chapter, we focus on an integrated approach to map changes in urban areas exploiting dual-polarization S-1 radar data, extending the limited results of our previous research [203]. S-1 data are used here to achieve a temporally and spatially fine analysis of the changes occurring in fast-growing megacities located in East Asia. We show that the approach using S-1 instead of scatterometer data does not degrade the ability to discriminate among temporal growth patterns. On the contrary, it provides finer spatial and temporal details and allows to focus on the built-up area automatically, as opposed to manually preselecting a few points close to a predefined geographical position, as in [201], or to averaging data using administrative boundaries, as in [202]. Therefore this research shows that, by the use of S-1 data, it is possible to further differentiate the spatial and temporal change patterns of urban areas that, as a whole, experience the same reflectivity and nighttime light change pattern. As a matter of fact, this is possible thanks to the better delineation of urban contours and internal block subdivisions obtainable with S-1 data.

This chapter is organized as follows. Section 4.2 introduces the proposed methodology, considering the city of Nanjing as an example. Section 4.3 reports and discusses the analysis results for the Greater Saigon and Shanghai, showing peculiar change patterns for these two megalopoleis. Finally, results for Guangzhou and Vientiane are provided to prove the robustness of the proposed approach with respect to cities of very different geographical extension. Eventually, Section 4.4 summarizes the main findings and proposes some ideas about future research steps.

4.2 Multi-pattern change exploration using heterogeneous data

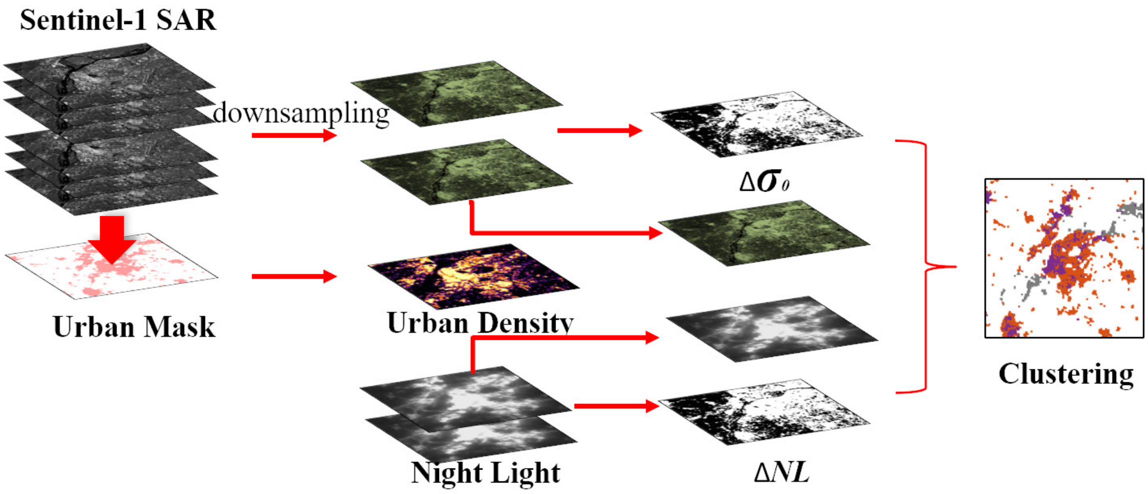

Figure 4.1: A graphical representation of the processing chain used to analyze the changes at the intra-urban level by combining nighttime lights and Sentinel-1 SAR data.

The core of the approach is based on the idea, first presented in [201], that changes in urban areas may be captured by both the change in the backscattered power by an active microwave sensor and the change in emitted lights at night, as captured by a passive optical sensor. Since active microwave sensors are more sensitive to spatial patterns, whereas nighttime data are more sensitive to population and economic activity density, the combination of the two factors highlights different changes affecting urban areas. As a matter of fact, the work in [201] proves the existence of a so-called global fingerprint of macro-scale changes. It well outlines what is possible to obtain from the point of view of urban studies, but it cannot be implemented in a semi-automatic processing chain, because it does not allow us to automatically focus the analysis on the urban area. The coarse spatial resolution of scatterometer data limits the analysis to the detection and categorization of the overall macro-scale changes of each urban area as a whole, if no geospatial ancillary data are available about urban extents and/or built-up density.

The free distribution of S-1 data and the previous studies about the possibility to exploit them for urban extent extraction and urban density analysis [204] highlight the possibility to move the original approach to the next level, by implementing a processing chain able to be applied to any specific urban area, and to improve the ability of the original technique to detect intra-urban temporal change patterns, as opposed to one single temporal patter per city. In a way, the new procedure allows to refine the temporal analysis at the second level of nomenclature, by further discriminating spatio-temporal patterns at the nominal resolution of the coarser data set, i.e.nighttime lights. The overall block structure of the processing chain is presented in Fig.4.1, and described in more detail in the next section. As an example, we used Sentinel-1 and nighttime light data recorded in 2015 and 2018 about the city of Nanjing (P.R. China).

4.2.1 The overall processing chain

The blocks in Fig. 4.1 graphically represent the processing chain by highlighting its steps.

1. **Urban extent extraction**: It has already proved in [204] that single or, better, multiple Sentinel-1 images on the same test site can be combined and processed to obtain a map of built-up areas, and eventually urban area extents. For the Nanjing test case, three Sentinel-1 images in July 2015 and three in March 2018 have been separately combined, the urban extent for these two years has been extracted and combined through a logical boolean OR operation, and the final urban extent map is shown in Fig. 4.2(a), superimposed to a 2018 Sentinel-2 multispectral image.

2. **Sentinel-1 data upscaling and change analysis**: To combine Sentinel-1 Ground Range detected data and nighttime light data, the original SAR data is first converted into the backscatter coefficient σ_0, and then spatially filtered by means of a Gaussian low-pass filter and down-sampled or resampled to the spatial resolution of the nighttime data (nearly 500 m for the Visible Infrared Imaging Radiometer Suite -VIIRS- data set. In this thesis, the monthly temporal averaging product of Version 1 VIIRS Day/Night Band Nighttime Lights is used). The upsampled S-1 data for 2015 and

2018 are then combined to obtain the $\Delta\sigma_0$, i.e. the change in backscattering characteristics of the urban area at the nighttime coarse spatial scale.

3. **Change pattern computation**: After computing the nighttime light change values ΔNT, ΔNT and $\Delta\sigma_0$ are combined to obtain the change vector analysis in this two-dimensional (2-D) space, whose results are graphically shown for Nanjing in Fig. 4.2(d) with a color legend referring to the built-up area density, a sub-product of the built-up area extraction in step 1 from SAR data at 10-m posting, which allows us to obtain the density information at the coarse spatial resolution of the change vector analysis without the need to refer to an external data set [see Fig. 4.2(b)]. This sub-product is obtained by computing the percentage of built-up area pixels extracted at 10 m inside the coarser spatial resolution (500 m) used for the following joint SAR-nighttime data clustering.

4. **Clustering of the temporal change patterns**: Eventually, the upsampled S-1 σ_0 , the nighttime data at the starting date and the change vector are clustered to discriminate among different temporal change patterns and initial conditions. Considering an arbitrary number of four clusters, the final clustering result for Nanjing is presented in Fig. 4.2(c). In this chapter, the Mixed Gaussian Model is used to classify multi-change-pattern. More flexible unsupervised classifier will be considered in Chapter 5.

4.2.2 Change vector analysis: the Nanjing test case

Change vectors enable to jointly represent the initial state and the corresponding variation of any change. This combination further deepens the understanding of change. The length and orientation of a change vector indicate change magnitude and change direction (increase or decrease). According to the characteristics of change vectors, multi-pattern changes can be explored through clustering. In comparison to change analysis after supervised classification, this data-driven scheme completely relies on the data and their underlying models.

Thanks to the accuracy of urban extent extraction from SAR data, the results in Fig. 4.2 basically highlights a main cluster within Nanjing. This cluster, depicted in orange, corresponds to areas with very little change. Indeed, the orange cluster groups change vectors with small modules. The real changes are concentrated in a few areas that belong to the blue and purple clusters, the latter one being composed by only locations experiencing a dramatic increase in nighttime level starting from an initial situation in July of 2015

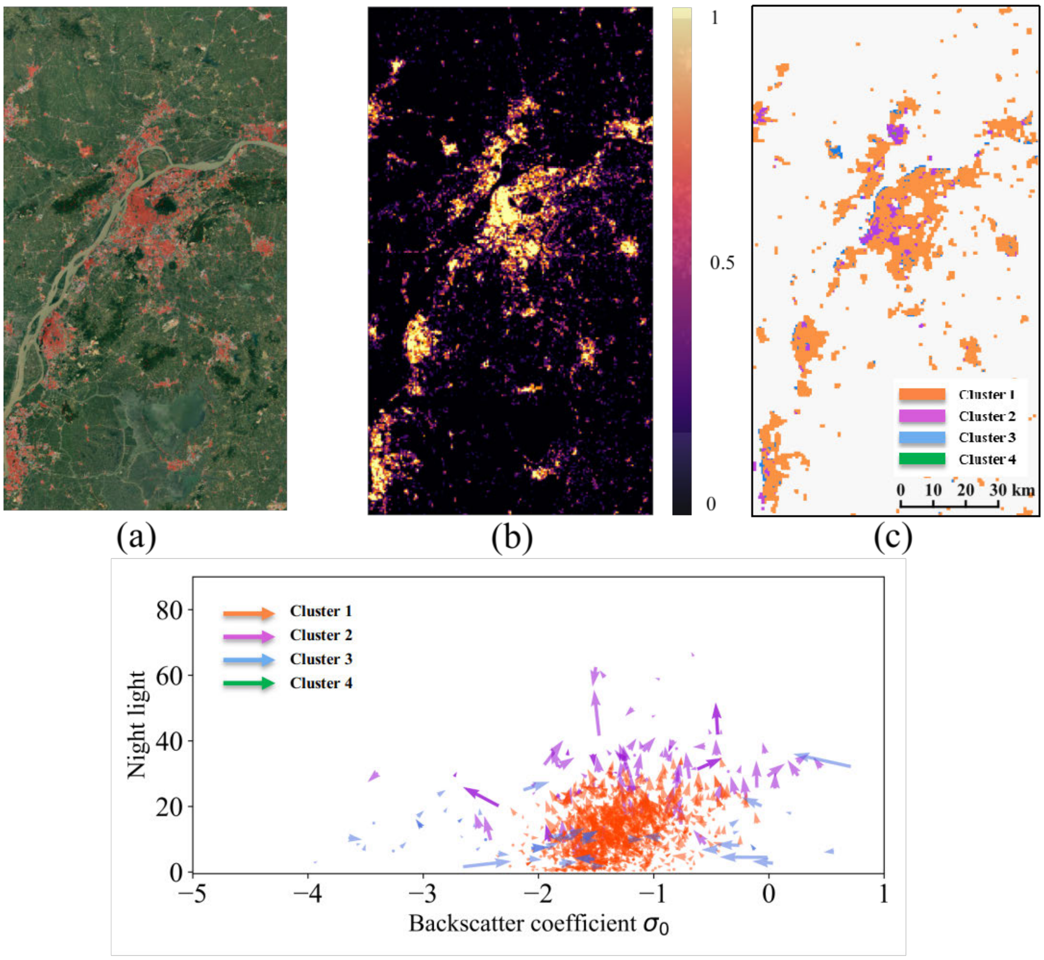

Figure 4.2: Intermediate and final results for the proposed processing chain applied to the city of Nanjing and considering the time interval between July 2015 and March 2018: (a) the urban extent combined from those extracted from S-1 data in 2015 and 2018 at about 20 m spatial resolution(10 pixel spacing); (b) the urban density map at nighttime spatial resolution (nearly 500 m); (c) the clustering analysis considering ΔNT and $\Delta\sigma_0$, as well as nighttime and radar data in 2015; (d) the change vector analysis using ΔNT and $\Delta\sigma_0$.

already showing large nighttime and backscatter values (monthly averaging on a collection of Level-1 Ground Range Detected (GRD) Sentinel-1 SAR and directly the monthly product of Version 1 VIIRS Day/Night Band Nighttime Lights are used). The blue cluster, instead, corresponds to areas that experience a significant but not so strong change. A check using freely available optical very high resolution imagery shows that the areas in the blue cluster are residential blocks where more and more buildings were added to the landscape, whereas the areas in the purple cluster correspond to more dense neighborhoods where there has been a significant change, such as the addition of new buildings/shopping malls, as in the example shown in Fig.4.3.

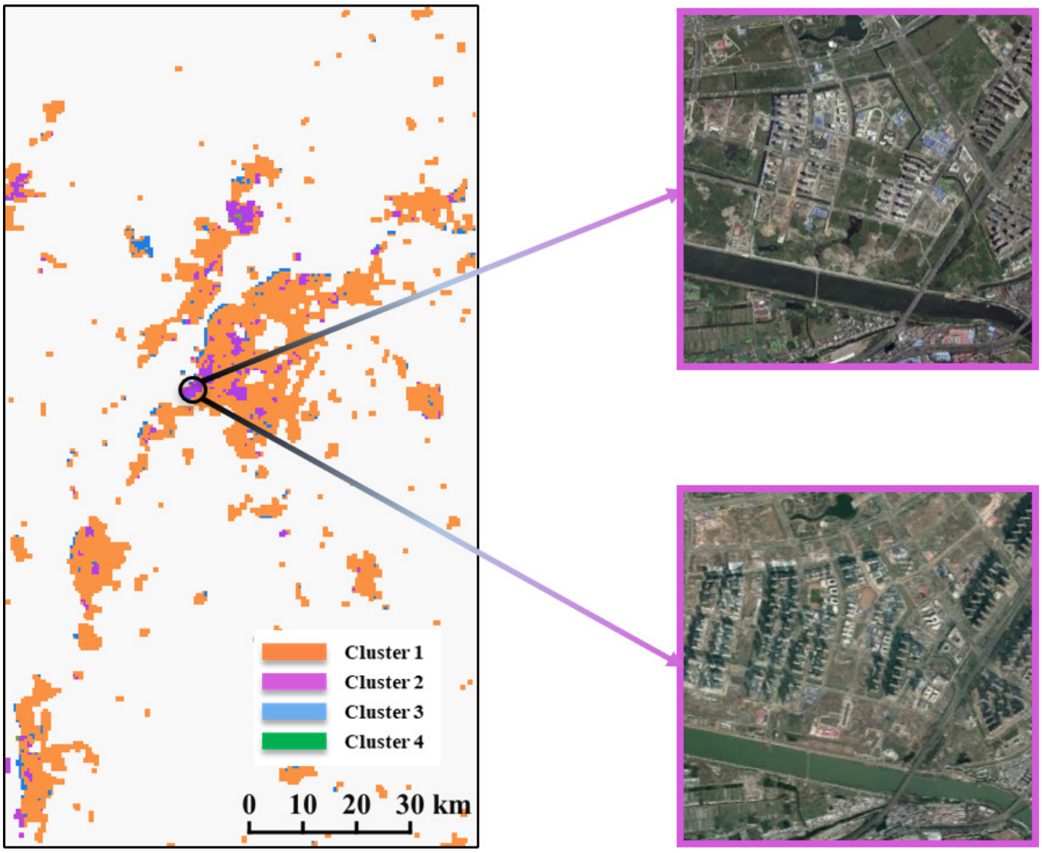

Figure 4.3: A visual check of the changes/no changes in one selected location in Nanjing using very high-resolution images in 2015 and 2018 available in Google Earth Historical Imagery.

4.2.2.1 Validating the Changes

The results of the proposed analysis are twofold. On one side, the extraction of the urban extents from S-1 data at fine spatial resolution allows detecting urban extent changes,

Table 4.1: Confusion matrix for the validation of the results in the subregion identified by a rectangle in Fig.4.2(c) with respect to Fig. 4.6(b)

Class		Ground truth		
		Blue	Purple	White
Predicted	Blue	26	37	7
	Purple	2	105	75
	White	0	0	38

mostly at the urban-rural fringe. On the other side, the clustering analysis applied to the change vectors discriminates between areas inside the urban extents that did not change and areas that experienced a change, with the possibility to further recognize which was that peculiar change. In order to validate these results, therefore, two different checks have been realized.

First of all, the urban extent changes have been validated, by selecting randomly 30 locations that the approach labels as changed, and checking whether that was a real change. The rationale for this check is that , thanks to previous experience [186], we expect a larger commission error, as opposed to omission error, due to the small mistakes in the urban area recognition approach. As a matter of fact, 28 of these areas include a recognizable change, accounting for an estimated commission error slightly lower than 7%. The second level of validation has been obtained by discriminating between areas inside the city extent that belong to clusters with very small change vector modules [represented in Fig.4.6a) in white], and those with larger ones [i.e., the purple and blue clusters in Fig.4.2 (d)], again in a binary way. By looking at the numbers in Table 4.1, the overall accuracy is 75.8%, and is reduced to 64.4% if the purple and blue clusters are considered separately. All in all, the approach provides a reasonable accuracy level, and opens the door to future routine monitoring tasks looking for different types of changes within urban areas.

4.2.2.2 Comparing the approach with previous techniques

Finally, to prove that the technique offers change patterns consistent with the original idea of using scatterometer (as opposed to SAR) data, in Fig.4.4(a) the same clustering results as in Fig.4.2(c) are provided, using the same processing chain except that upsampled Advanced Scatterometer (ASCAT) data (freely accessible at EUMETSAT [205]) are used instead of upsampled S-1 data. The meaning of the different clusters is accessible by looking at Fig. 4.4(b), where change vectors are colored according to the clusters. A comparison between Fig.4.4(b) and 4.2(d) shows that the orange cluster of the analysis using S-1 is split into the orange and green ones using scatterometer data, and the local changes that are available using S-1 are only very partially recognized (due to the coarse spatial resolution) using ASCAT.

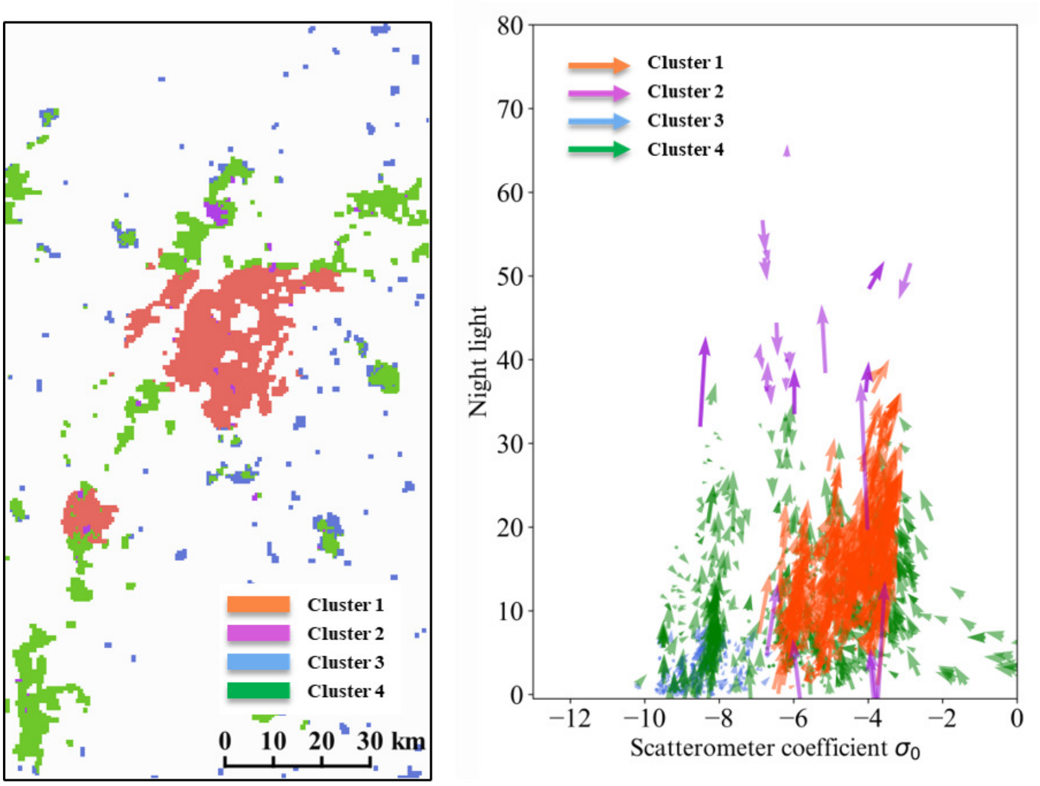

(a) (b)

Figure 4.4: Results for the city of Nanjing, still considering the interval between July 2015 and March 2018, but using ASCAT data instead of S-1 data: (a) the change vector analysis using $\Delta\ NT$ and $\Delta\sigma_0$; (b) the clustering analysis considering $\Delta\ NT$ and $\Delta\sigma_0$, as well as nighttime and ASCAT data in 2015.

By comparing the spatial locations of the clusters and their position in the change vector space, it is possible to state that the overall temporal patterns recognized using either S-1 or ASCAT data are very similar. The spatial distribution of the clusters reveals some differences, as expected, because the level of detail provided by S-1 is orders of magnitude finer than the one by ASCAT. It must be stressed, however, that the results shown in Fig. 4.4 make use of S-1 data to focus the clustering and change vector analysis only to the area with urban density higher than 18%. This value corresponds to the minimum density of built-up in an ”urban” pixel at the spatial resolution of the nighttime lights computed by considering the much finer map extracted from S-1 imagery.

Accordingly, on one side these results show that, on a relatively long temporal interval (three years, from 2015 to 2018), the main changes in urban features can be tracked efficiently using scatterometer data, provided some sort of focusing on the urban area extent is exploited. On the other side, they also reveal that using S-1 data, it is possible to obtain more details in space. To further stress the improved performances of the proposed approach, it has been eventually applied to the same test area with a temporal span of one year only, i.e., considering 2015/2016, 2016/2017, and 2017/2018. The urban extent changes obtained by comparing the urban extents extracted by S-1 at the original 10-m spatial resolution are shown in Fig. 4.5, where red (small) areas correspond to changes in the overall 2-D structure of the city, shown in white. Two examples of changes detected by the clustering results are also reported, enlarging the corresponding portion of the change

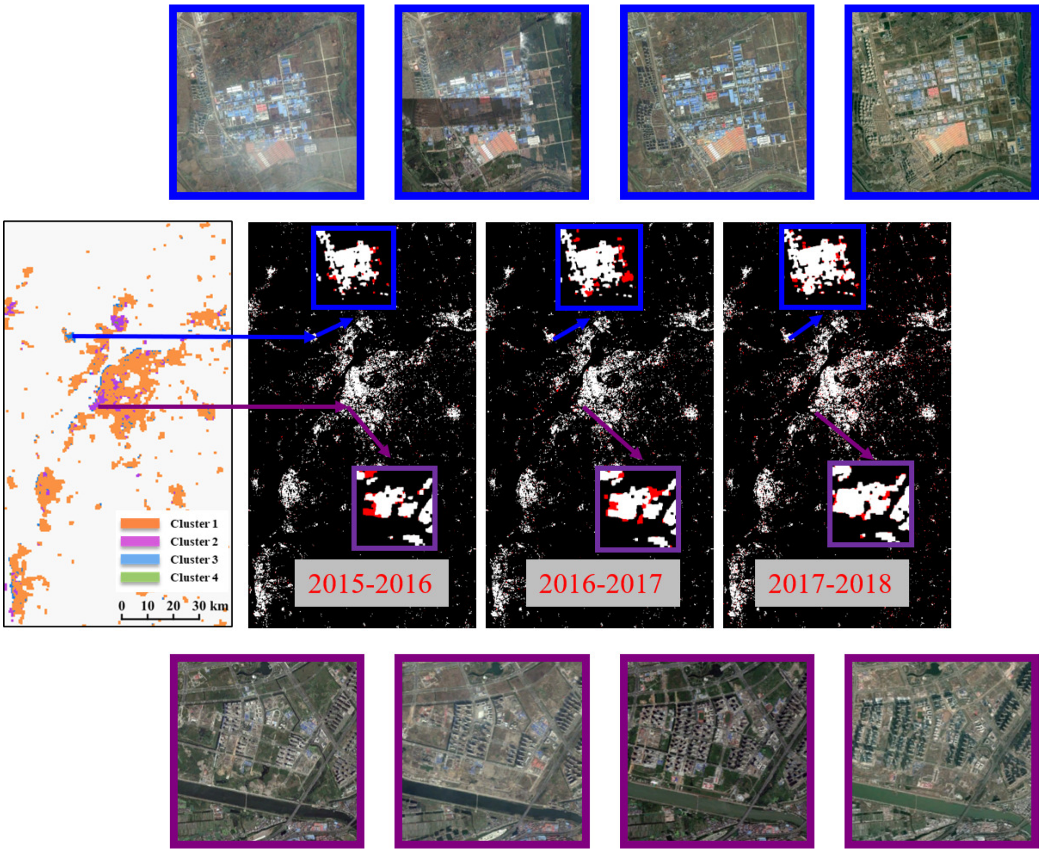

Figure 4.5: Temporal analysis with a time step of one year for the Nanjing urban area using S-1 and nighttime light for volumetric analysis (left) and S-1 alone (at about 20 m spatial resolution) for urban extent growth (center row, changed areas appear in red). The top and bottom row display VHR images (from Google Earth) of two locations selected using the joint nighttime/S-1 clustering and whose different temporal change pattern is captured by the S-1 change maps.

map. The idea is to show that the use of S-1 data, with its fine spatial resolution, allows us to classify these patterns, allowing us to recognize that the top one happens gradually in time, whereas the bottom one is a more abrupt change, between 2016 and 2017. The sequence of optical VHR images reported in the figure visually validate the findings.

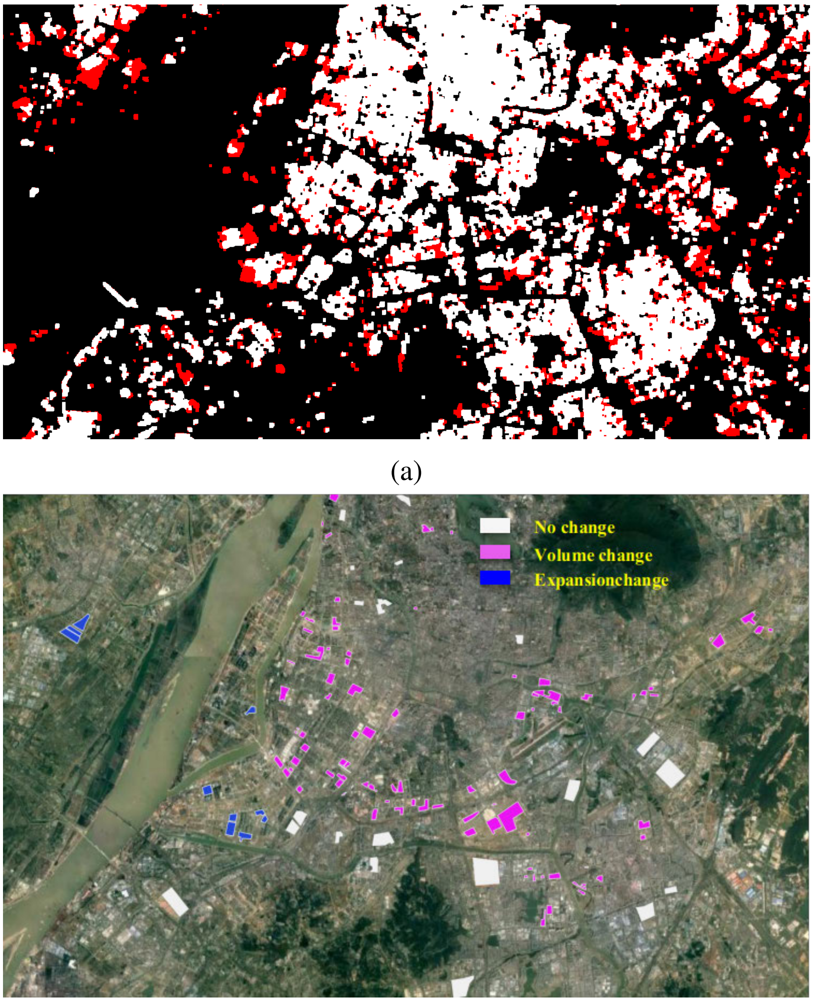

(a)

(b)

Figure 4.6: Ground truths for the subregion identified by a rectangle in Fig. 4.2(c): (a) changes at 10-m pixel spacing used to validate urban extent changes extracted from S-1 data (in red); (b) volumetric and expansion changes used to validate the blue and purple clusters, as well as no changes in white, all obtained by manual inspection.

4.3 Experimental results : Change detection using Sentinel-1 SAR and nighttime lights

The proposed approach has been tested on many different locations, and here we start by reporting its results for the Greater Saigon area, in Vietnam. The results graphically reported in Fig. 4.7, are consistent with those in the recent work of Balk et al. [202]. The joint clustering of S-1 and nighttime data shows an increase of activity in the city center, mostly related in the three years from 2015 to 2018 to an increase in nighttime lights, and only moderately due to an increase in backscatter. Therefore, it is confirmed that the area currently experiencing changes due to higher economic activity (as found by the study in [202]) is the city center. The change analysis using S-1 data at about 20-m resolution in Fig. 4.6b, similarly, shows that the urban expansion is still happening in the areas to the North and East of the major urban core. Specifically, the circle and the rectangle in Fig. 4.7(a) and (b) identify two locations that belong to the purple and green clusters, i.e., areas with a significant change in the nighttime lights. Still, only the area inside the red rectangle in Fig. 4.7(b) actually corresponds to a change of urban extent because of new constructions.

More clearly, the temporal evolution in these two areas is shown in Fig. 4.8, and visually confirms the results of the previous analysis. It can be seen that the change in the area highlighted by the circle corresponds to the construction of taller buildings in place of existing ones, hence no change in the urban extent has occurred. Instead, the area within the rectangle is an actual enlargement of the built-up area in 2015 due to new constructions. Finally, in Fig. 4.9(a), the 2-D changes at 10-m spatial resolution for the Greater Saigon area between 2016 and 2018 (in red) are superimposed to the 500-m spatial resolution changes obtained by clustering nighttime lights and the SAR backscattering coefficient (in purple and green, see Fig. 4.7). Apart for the obvious consideration that the 10-m spatial data provide finer details, it is interesting to note that green pixels are usually associated with red ones, showing that the pixels belonging to the green cluster correspond to changes due to an increase/decrease of the built-up. Instead, pixels in purple very seldom occur in area with red dots, supporting the idea that this cluster corresponds to changes due to volumetric/activity changes without relevant increase/decrease of the built-up.

Like for Nanjing, these results have been validated in two ways. First, by comparison with a map of locations manually selected and corresponding to areas that experienced no change, volumetric change, or urban extension change, respectively, reported in Fig. 4.9(b). Second, by manually checking 30 locations that are marked as red dots [reported in Fig. 4.9(c)] to understand whether they correspond to real changes of the urban extents or

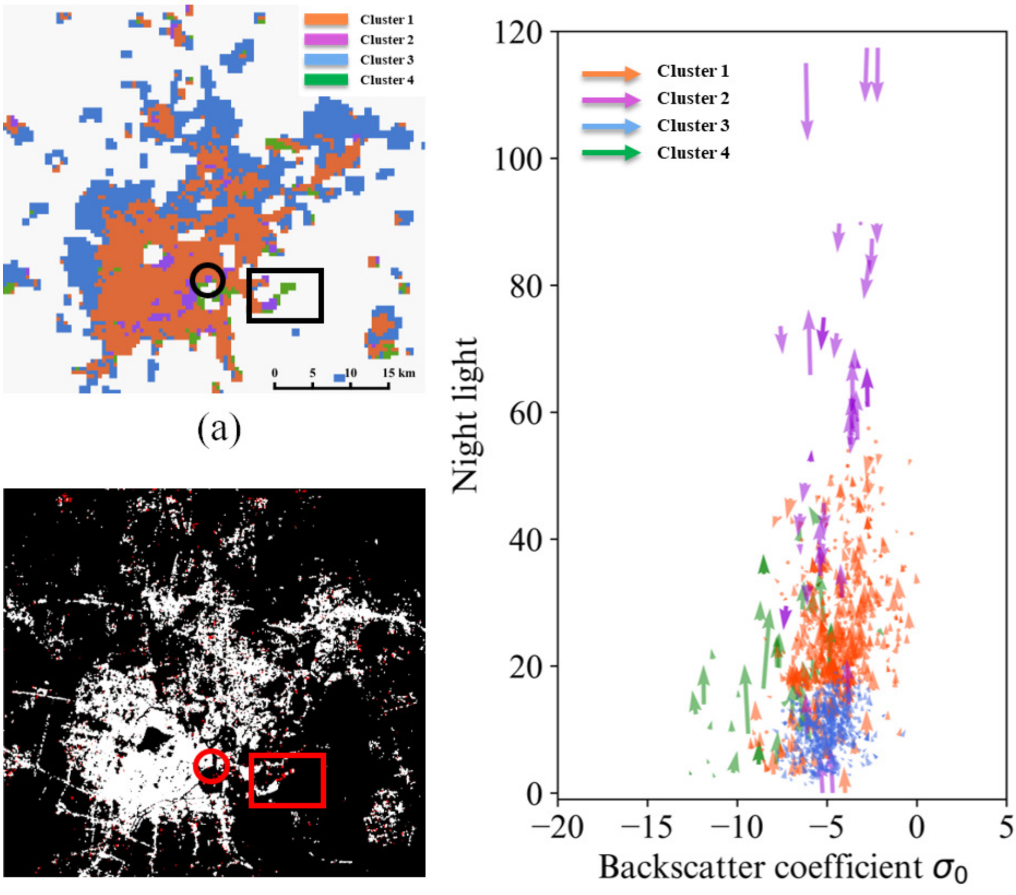

(a)

(b)

(c)

Figure 4.7: Experimental results for the Greater Saigon test area: (a) clustering maps using S-1 and nighttime data; (b) two-dimensional change detection for urban extents at 10 m spatial resolution using S-1 urban extent maps in 2015 and 2018; (c) graphical representation of these clusters in the $\Delta\ NT, \Delta\sigma_0$ domain.

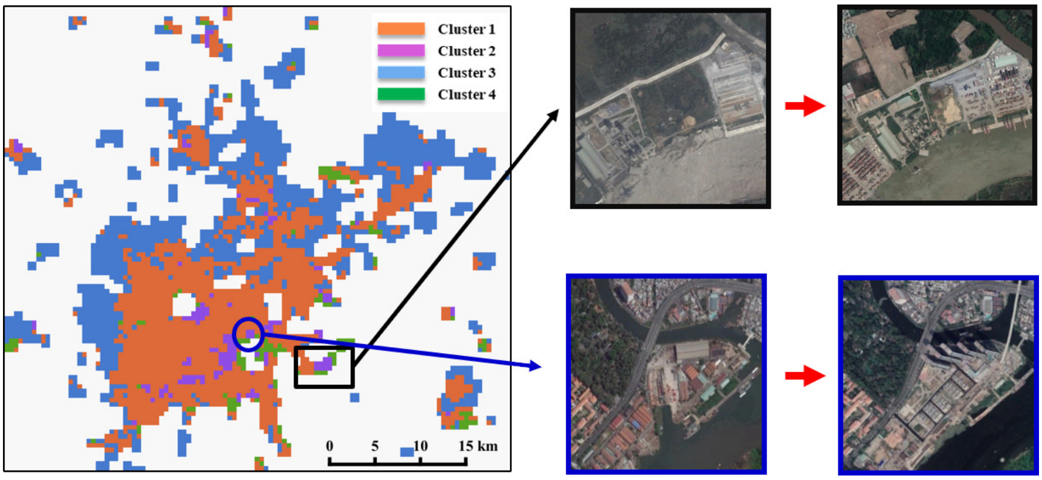

Figure 4.8: Visual analysis of the temporal evolution of the areas highlighted in Fig.4.7 for the Greater Saigon urban area, and corresponding to (top row) a volumetric change as opposed to (bottom row) a built-up area extension.

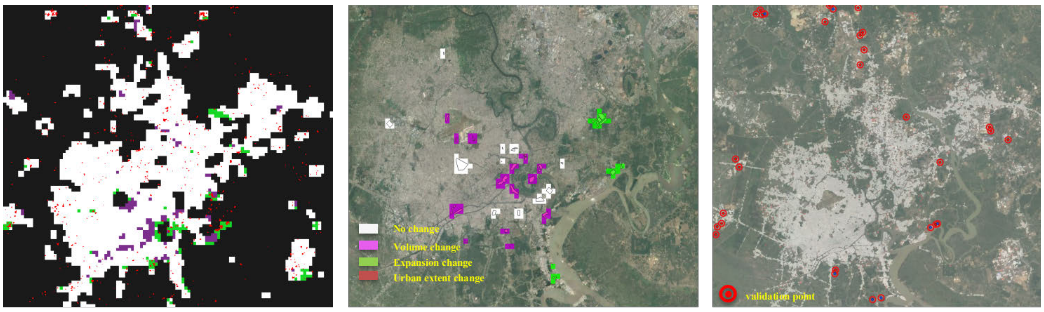

(a) (b) (c)

Figure 4.9: (a) Different changed pixels identified for the Greater Saigon urban area (see Fig. 4.7): in red changes at 10-m pixel spacing, recognized by comparing urban extents extracted from S-1 data, in green and purple changes at 500-m spatial resolution obtained by clustering the changes in nighttime lights and SAR backscatter coefficients and corresponding to volumetric and area extension changes, respectively (see Fig. 4.8), and finally in white pixels recognized as "unchanged." (b) Ground truth for the white, purple, and green classes, obtained by manually digitizing areas that experienced no change, volumetric changes, and urban extension changes, respectively. (c) Selection of 30 locations marked with red dots in (a) and checked for urban extent changes.

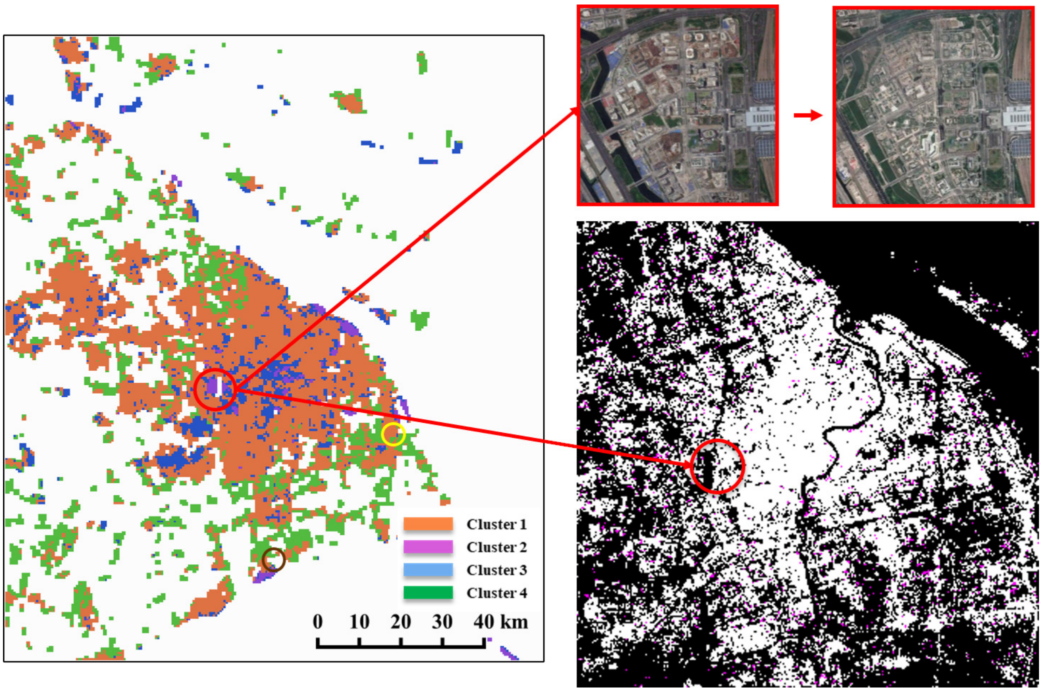

Figure 4.10: Clustering results for Shanghai, and visual assessment for the area highlighted by the yellow circle, an area that is picked as changed with respect to backscattering coefficient and nighttime light, but that in reality experienced a limited change in both the built-up extents and their volume.

Table 4.2: Confusion matrix for the validation of Fig. 4.9(a) with respect to Fig. 4.9(b)

Class		Ground truth		
		Green	Purple	White
Predicted	Green	27	11	27
	Purple	18	26	7
	White	0	1	38

not. The results of the first analysis are reported in Table 4.2, which shows that although the overall accuracy considering three classes is low (59%), such as in the Nanjing test site, the same value for change versus no change increases to 77%, whereas the ability to discriminate between volumetric and extension changes is quantified by a 65% overall accuracy. The results for the second analysis, instead, validate the changes at finer spatial resolution, because a visual check revealed that 23 of the 30 randomly selected locations indeed identify a change in the urban extents.

Another test area analyzed by means of the proposed procedure is the city of Shanghai, whose results are shown in Fig. 4.10. Even in this test case, the changed portions are depicted in purple after the clustering step is applied. The area that is highlighted and whose change is visually assessed by considering VHR optical data is an area with a large difference in the amount of activity (hence nighttime lights) in 2015 and 2018, but where 2-D and 3-D changes were very limited (although not null).

Finally, we report the results for Guangzhou, one of the fastest-growing cities in China, and Vientiane, in Laos. The clustering results for change detection are reported in Fig. 4.11 with a few examples of the changes occurring in the selected locations. The results for these two cities are provided to show that the approach works irrespectively of the size of the urban area under analysis because the urban extents extracted from S-1 data constrain the clustering procedure within the area relevant to the research.

It is important to note that all the 2-D changes detected in Shanghai, Guangzhou, and Vientiane are in line with what is reported in [206], although on a smaller scale, since the temporal interval that is considered here is only three years, from 2015 to 2018. Changes due to an increase/decrease of the built-up volumes and/or of the socio-economic activity level are invisible to a research based on impervious surface mapping, such as the one mentioned before. Instead, the joint analysis of the change patterns obtained via S-1 and nighttime clustering and the urban extent change maps from S-1 provides more information and allows detecting different types of changes.

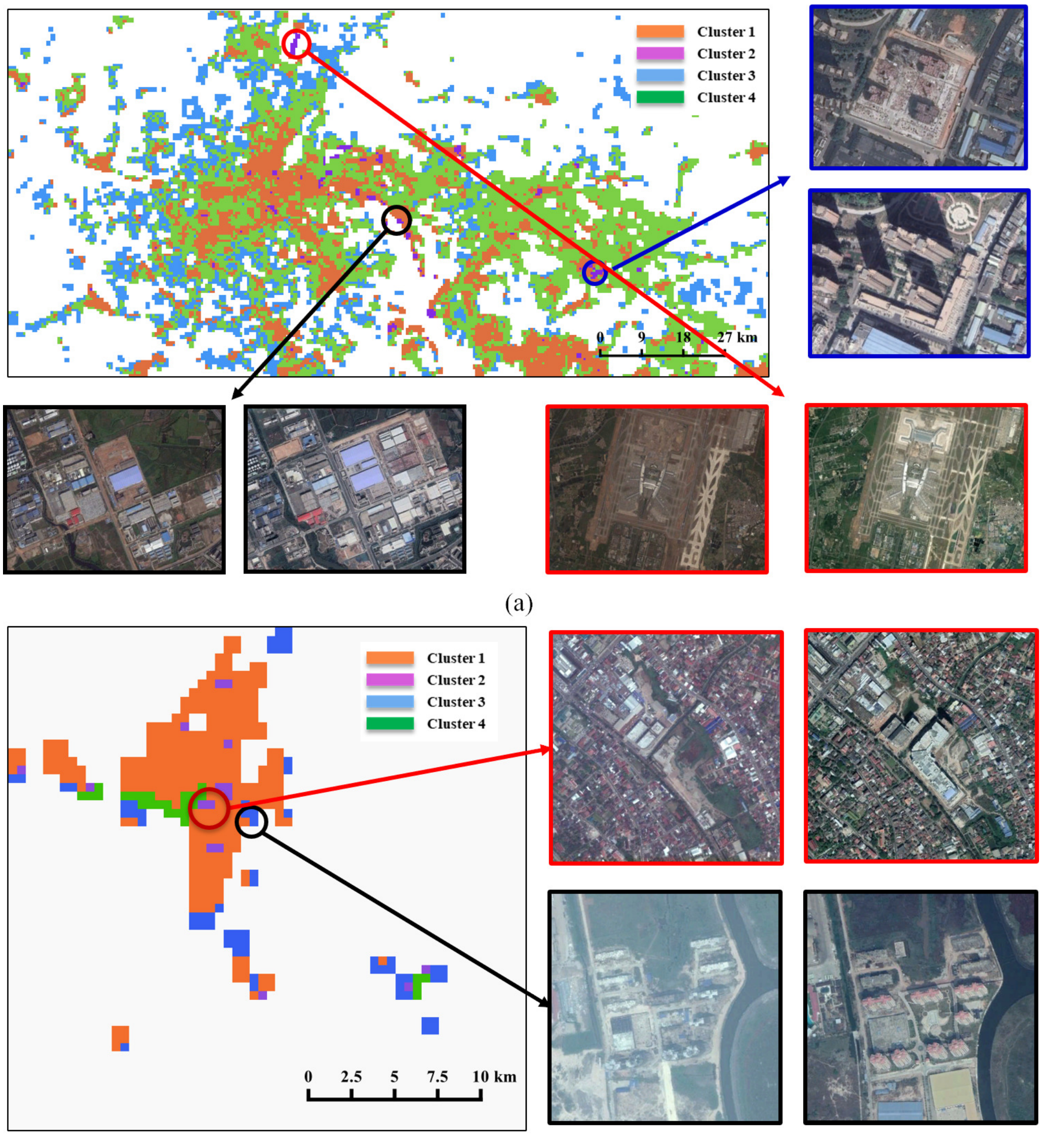

(a)

(b)

Figure 4.11: Clustering results for Guangzhou (China) and Vientiane (Laos), with a few examples of temporal patterns that have been extracted and can be recognized.

4.4 Conclusions

In this chapter, an automatic procedure to extract urban extent changes and volumetric pattern changes in urban areas has been proposed. The input data to the procedure are S-1 images and nighttime data. Exploiting the spatial resolution of S-1 data to focus the change vector analysis to the built-up area and the correlation between the radar backscatter and the structural variations in two and three dimensions within the human's settlement, it is possible to automatically look for intra-urban patterns of change and recognize different temporal behaviors, to be subsequently identified by visual analysis of VHR images. The main contribution of this chapter is, therefore, the design of a novel procedure to detect and characterize 2-D and 3-D changes inside urban areas by combining S-1 and nighttime data in an automatic way. Experimental results in five different urban areas allow validating the proposed framework by showing that the detected patterns actually correspond to peculiar changes in the 2-D/3-D structure of urban blocks.

By using this approach, thanks to the increasing amount of data from S-1 sensors, it will be possible to analyze yearly changes at the intra-urban level even for small human settlements, providing more and more information to monitor the growth in all three dimensions of human settlements over time.

Future research steps will be devoted to an automatic approach for the recognition of the different temporal patterns that are grouped into the same cluster, and to the automatic selection of the number of clusters. In fact, at the moment, the recognition of the temporal pattern is not performed, but, as shown in the previous examples, the approach provides the information that is needed to discriminate volumetric and 2-D changes. Still, more sophisticated recognition procedures need to be designed to single out different types of change, for instance, related to socio-economic activities in the urban area and not to any change in its structure.

Chapter 5

Change pattern exploration at the megacity/urban cluster level

In this chapter, to generalize from cities to megacities, megalopolis, urban clusters or large urban aggregations, a few areas in different geographical locations are analyzed in both the space and the time domain. Exploiting the approaches presented in the previous chapter, improved by means of a novel hierarchical clustering technique, urban changes are mapped in terms of multiple spatiotemporal patterns, generated by vectorized change descriptors exploiting the combination of SAR and multispectral data.

5.1 Introduction

In the last ten years, the harmonization of rapid urbanization and increased economic activity in and around urban areas with air quality and urban land use has been the most important concern for the urban development policy in many different countries, e.g., in P.R. China [207] [208]. Accordingly, an urgent and challenging task is to improve the knowledge and understanding of change patterns in human settlements, especially for fast-urbanized urban aggregations in Africa, South America, as well as South and East Asia. Thanks to the availability of time-series of heterogeneous remote sensing data, it is now possible to explore these changes decoupling those due to urban expansion and those due to increasing economic activities [163]. To this aim, in this work we combine multi-temporal Sentinel-1 Synthetic Aperture Radar (SAR) C-band sensor and Visible Infrared Imaging Radiometer Suite (VIIRS) nighttime sensor (also called the Day/Night Band, or DNB) to explore urban change patterns at the geographical scale of a so-called “megacities” or “megalopolis”. The joint use of heterogeneous sensors allows discovering more spatial-temporal features and deeper relationships between urban constructions and nighttime-

Table 5.1: the remotely sensed measurements (also called features) considered in this work

Features	Description
Base VV σ_0	Backscattering coefficient σ_0 for the VV polarization of the SAR image at the starting date of the considered time period
Base VH σ_0	Backscattering coefficient σ_0 for the VH polarization of the SAR image at the starting date of the considered time period
Base NL τ	Nighttime light data at the starting date of the considered time period
Difference VV $\Delta\sigma_0$	Change of the backscattering coefficient σ_0 (VV polarization) in the considered time period
Difference VH $\Delta\sigma_0$	Change of the backscattering coefficient σ_0 (VH polarization) in the considered time period
Difference NL $\Delta\tau$	Change of the backscattering coefficient σ_0 (VH polarization) in the considered time period

based changes, which indirectly reflect the connections between urbanization and economic development.

5.2 Change pattern exploration with hierarchical clustering

The procedure used in this work relies on the processing chain described in [209]. First of all, Sentinel-1 SAR is used to extract urban extents. This step ensures that the focus of the analysis is in built-up areas at the finest spatial resolution for freely available data sets. To handle big-size data over each megalopolis, that includes a cluster of geographically adjacent metropolitan areas which may be somewhat separated or may merge into a continuous urban region, the critical preprocessing steps and computations are performed in Google Earth Engine (GEE) [210]. Then, data-driven unsupervised classification is used to explore change patterns according to a feature space joining the base and the change images. In this way, both the initial state and the temporal change pattern are considered.

To extract the urban change patterns for these areas, we exploit the same data sets considered in [209], i.e., SAR and Nighttime lights data. In this chapter, the monthly temporal averaging product of Version 1 VIIRS Day/Night Band Nighttime Lights is used with a resolution of about 500 m, and the Sentinel-1 SAR of Level-1 Ground Range Detected (GRD) is selected as SAR input. Specifically, the initial and difference data by SAR and nighttime light sensors, listed in Table 5.1, are considered. They are combined and analyzed according to the procedure described in the next Section.

The peculiar step introduced in this work is a more effective unsupervised clustering as opposed to [209], which include the joint exploitation of four different algorithms: K-means, GMM (Gaussian mixed model with EM algorithm) [211], and ByGMM (Variational Bayesian Gaussian Mixture) [212]. These four techniques are adaptively applied to the same feature space. Following this step, the procedure in [209] is resumed, and a 2-dimensional change vector analysis is applied to interpret the clustering results. Considering the resolution difference between the Nighttime light sensor and Sentinel-1 SAR, upscaling is applied to the SAR images to match VIIRS images at 500-meter resolution. However, in this paper, due to the wide geographical area of analysis, and the fact that it contains several metropolitan regions that are spatially disconnected, this vector analysis is performed at the object level. The object extraction is based on each class image generated by clustering via connected component analysis. While more details about most of these steps are available in [209], the heterogeneous clustering procedure is the novel part proposed in this paper, and will be described in detail in the following subsection.

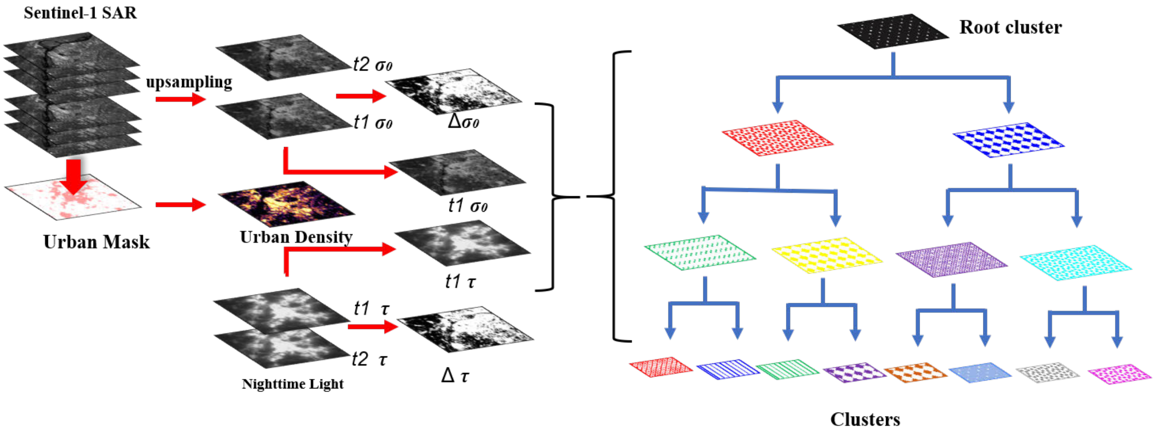

Figure 5.1: Workflow of the urban change pattern exploration procedure used in this chapter.

5.2.1 Hierarchical clustering

The performance of unsupervised classifiers depends on the data geometrical distribution in the feature space, as well as on the clustering principle they exploit. Accordingly, clustering applied to (very) heterogeneous data from different sources poses challenging issues with respect to the recognition of reliable clusters. Specifically, it may happen that a few observations often receive ambiguous class or cluster labels when multiple classifiers are applied to the same feature space. This is especially true for outliers or noisy measurements. In turn, this issue may mask patterns of urban changes interesting for our research. In this paper, a hierarchical 2-component clustering approach is applied to more reliably extract change patterns in urban built-up areas. The clustering begins from what we call the root clustering result, obtained by applying binary clustering by means of multiple algorithms (the above-mentioned k-means, GMM, ByGMM), retaining only "reliable" clustering results and excluding "ambiguous" ones. By the term "reliable" here we consider (see Fig. 5.2a) results that are consistently labeled as belonging to the same cluster, identified by its mean representative point. Next step is a further refinement of the binary clustering restricted to the reliable clustering results, once again looking for stability in the assignment to clusters by multiple algorithms. The procedure, schematically represented in Fig. 5.2b, eventually ends after a few iterations (three, in this paper), providing reliable and unreliable clusters of data points. Further analysis is therefore focused on reliable clusters only, reducing possible issues and misinterpretations.

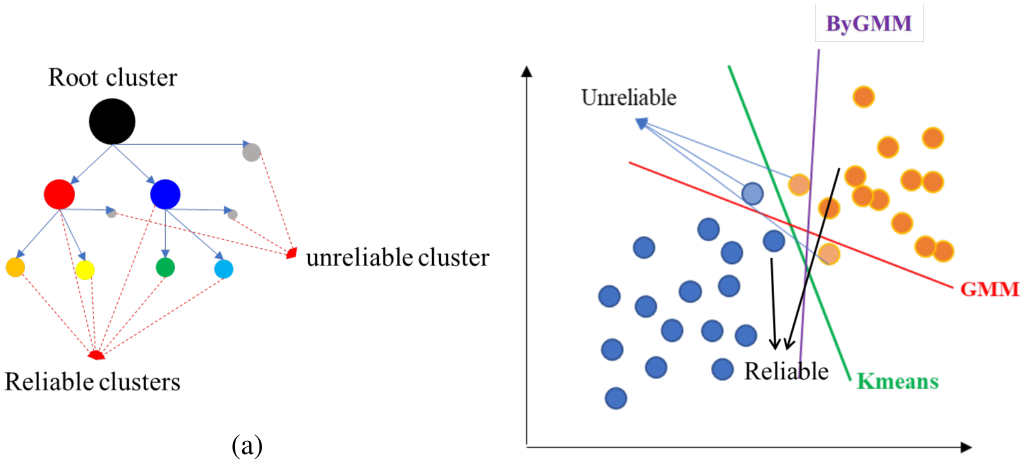

(a)

(b)

Figure 5.2: Graphical representation of the hierarchical multi-scale unsupervised clustering.

5.3 Experimental results

More formally, and following [213], a "megalopolis" is a cluster of multiple urban areas where usually the government policy aims at knitting the area together more tightly and promoting development through transportation and communication links . In this paper, we focus first on two megalopolis in China, namely the Jingjinji (JJJ) and the Yangtze River Delta (YRD), which correspond to the currently most developed and the most densely populated portions in P.R.China. These cities have boomed in population and economics for decades and are in the path to become the largest megalopolises in the world.

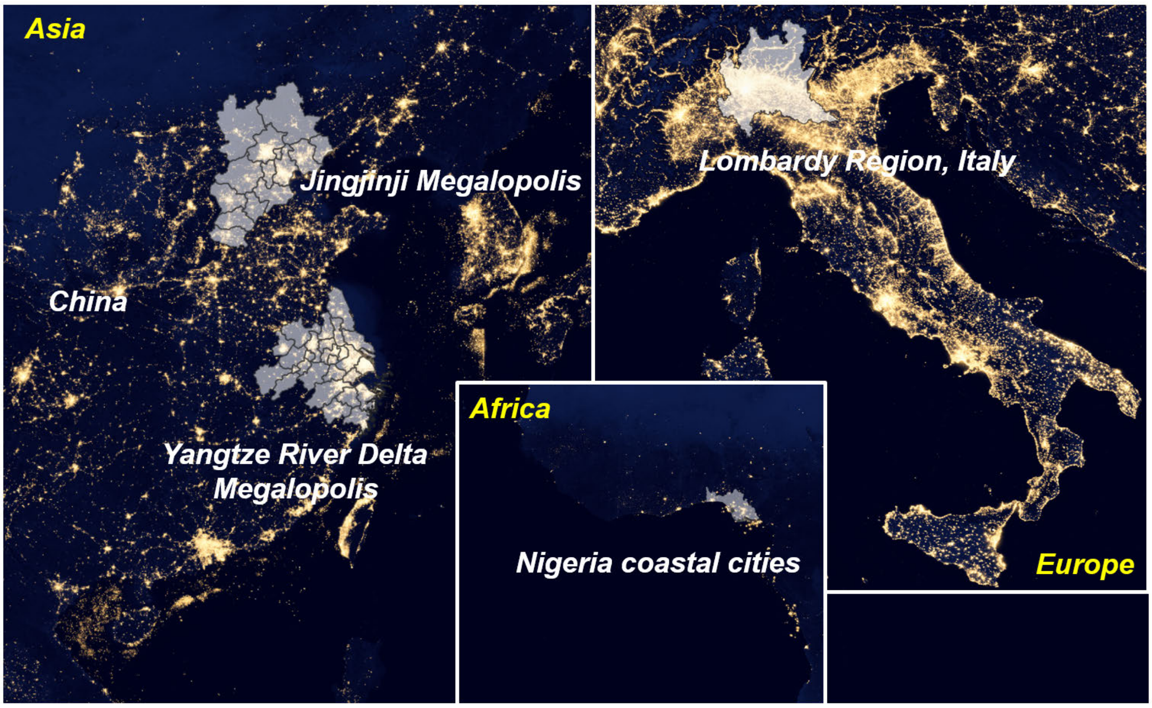

Figure 5.3: Geolocation of the studied areas.

In addition to these areas, we also select other two comparative study areas: the urban cluster of the Lombardy region in Italy, and the urban clusters of the coastal cities along the Gulf of Guinea. The rationale for this selection is that the former is one of the most developed urban area in Europe and the latter one is one of the fastest and most populous developing urban area in Africa. More specifically, in the Lombardy region the Milan metropolitan area, known as Greater Milan, is the largest metropolitan areas in Italy. It includes the provinces of Milan, Bergamo, Como, Lecco, Lodi, Monza and Brianza, Pavia, Varese and the Piedmontese Province of Novara, while some scholars also include the Province of Cremona and Brescia in Lombardy and the Emilian Province of Piacenza [214]. The overall population under the narrowest definition is about 8.2 million over an area of about 13,000 km2 [214].

As for the above mentioned African cluster of coastal cities, Nigeria is the most populous country and the largest economy of 2018 in Africa [215]. In this work, we focus on Lagos, Ibadan, Port Harcourt to understand its urbanization trend and its relationship with economic activities.

5.3.1 Case 1: Megalopolis in P.R.China

The first layer of the hierarchical clustering procedure generates two clusters, and the scatterplots for every possible feature pair of features for the Jingjinji megalopolis are shown in Fig.5.4a and the corresponding geographic area geographical is visualized in Fig. 5.4b. Specifically, Fig. 5.4a represents the projection of the retrieved two (red and blue) clusters in every possible 2-dimensional sub-spaces of the base data. It is clear that the red and blue clusters correspond to different urban temporal patterns, and this is consistent with the spatial structure of these clusters for Beijing in Fig. 5.4b. The area in the red cluster has high building density at the starting date (base VV σ_0 and base VH σ_0) and a small change in any difference feature space (difference VV $\Delta\sigma_0$, difference VH $\Delta\sigma_0$, and difference NL $\Delta\tau$). Therefore, the red cluster may be interpreted as the core urban area, that (in average) does not change much during the considered time period. Instead, the blue cluster expands corresponds to low building density undergoing big changes, and may be interpreted as the urban fringe subject to fast urban expansion.

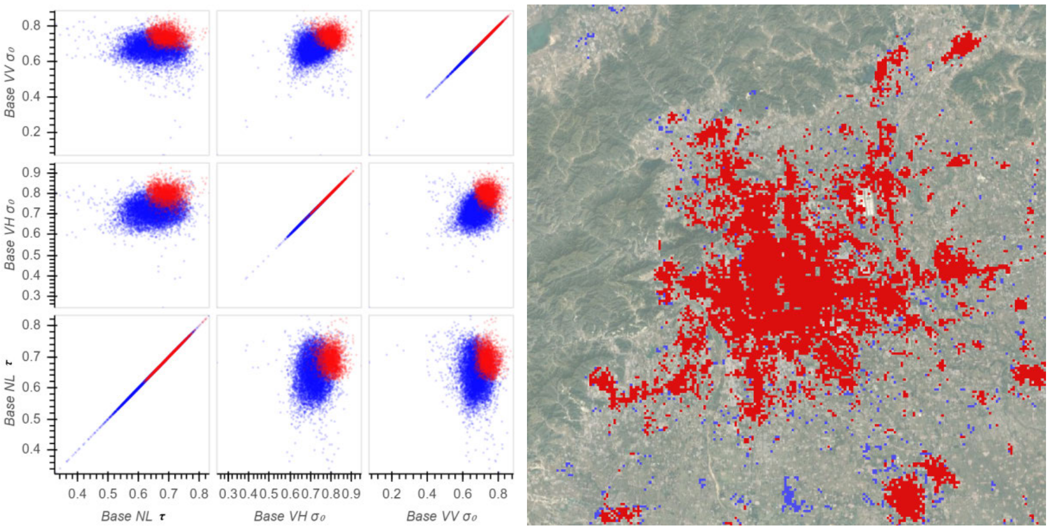

(a) (b)

Figure 5.4: Beijing: (a) bi-dimensional scatterplots of the clusters extracted in the first layer of the hierarchical clustering procedure; (b) corresponding spatial extents of these two clusters.

In the second layer of the hierarchical clustering system, new clusters are obtained by separating the “parent clusters” and more detailed change patterns are revealed (see Fig. 5.5). The red and green clusters obtained from the red cluster in the upper layer represent a further subdivision of the core area into its more stable part and the transition areas towards the fast developing urban fringe, and are consistent with the well-known urban circle structure of Beijing, and its pattern of urban outward expansion.

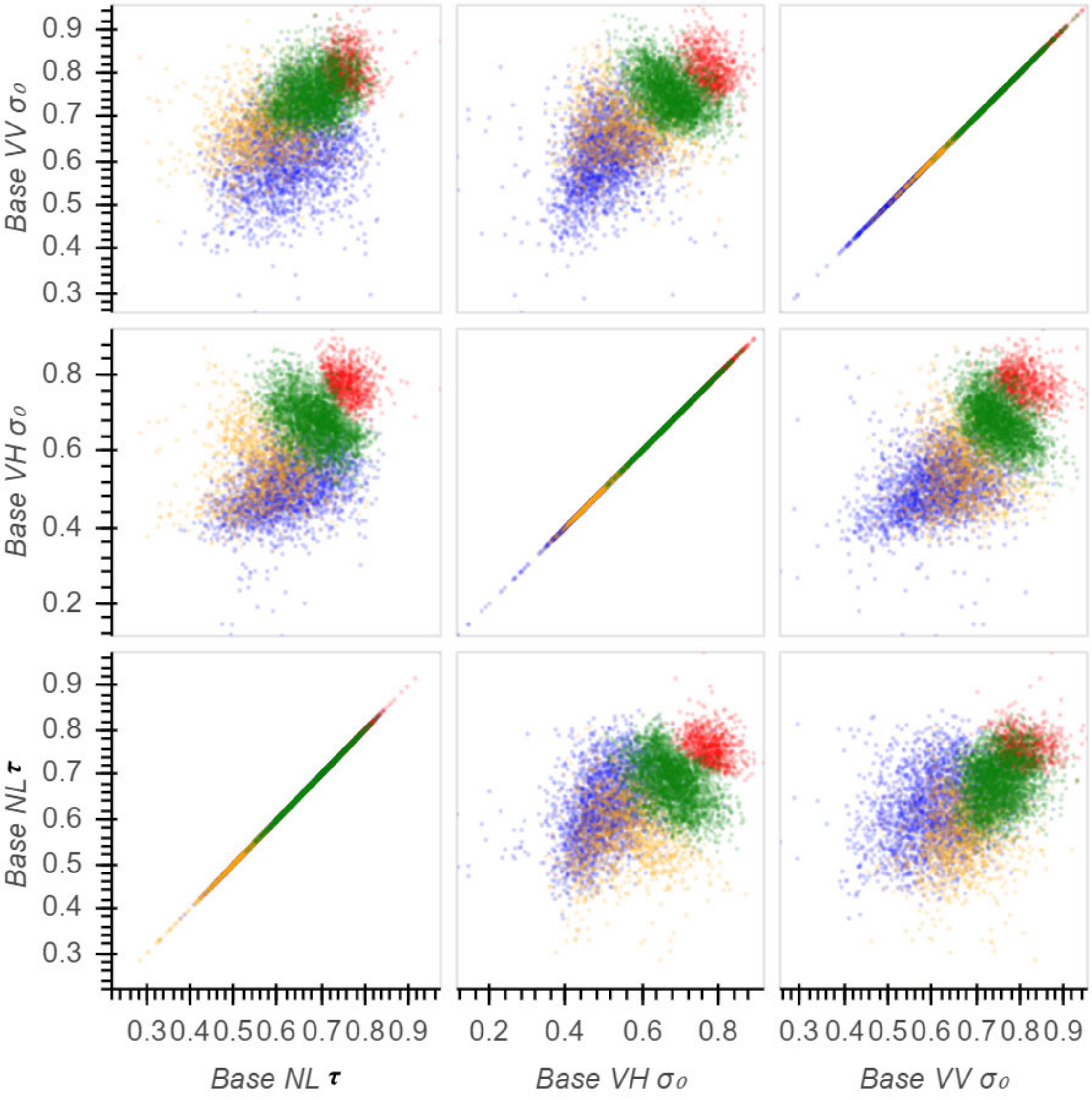

Figure 5.5: Jingjinji: bi-dimensional scatterplots of the clusters extracted in the second layer of the hierarchical clustering procedure.

Within a relative short time-interval (in this work we are considering the interval from 2015 to 2018), however, the expansion is limited. More obvious changes occur in villages and towns surrounding the main built-up area, which correspond to the yellow and blue clusters in Fig. 5.5 and 5.6, obtained from further clustering applied to the blue cluster in Fig. 5.4.

The 4-component clusters allow recognizing more urban expansion patterns. Indeed, the blue and yellow clusters are discriminated thanks to different change directions for the backscattering coefficient (i.e., the change in built-up structures). As shown in Fig. 5.7, the new constructions recognized as elements of the blue cluster commonly and frequently occur beyond the suburban area, and often accompany demolitions (recognized as elements of the yellow cluster).

Looking in more detail to the urban change patterns extracted by this technique, it is possible to appreciate that they are different depending on the urban size. For instance, among the three considered Chinese megalopolises, the expansion of cities with population over 8 million people, like Beijing, Tianjin, Shanghai, Nanjing, Guangzhou and Shenzhen, is spatially discontinuous and starts from towns away from main built-up area. Cities like Xingtai, Wuhu and Qingyuan, which are smaller, spread randomly in all directions and more continuously in space.

Patterns are even more complex and rich of information when considering 8-components clustering. The above-mentioned core urban areas (the red cluster in 4 components) are further separated into purple and red clusters. Both clusters correspond to almost no changes for the Jingjinji and Yangtze River Delta megalopolis, because of the highly developed infrastructure supporting a variety of entertainment and commercial activities. The suburban areas (subdivided into green and olive clusters), corresponds to areas with lower building density and more low-rise buildings, with lighting facilities utilized to support the public transportation rather than entertainment and commercial activities.

As for the external and fast-changing areas, the 8-components clustering helps to single out different changes in terms of feature magnitude and direction (increase or decrease). For instance, the blue cluster in Fig.5.5 shows a 10-20% increase in VV σ_0 but no change in NL τ and VH σ_0, which means no change in volume scattering and no spatial overflow and saturation of light, and this can be explained with construction activities of low density and low-rise building away from urban area. More detailed investigation can be found in table 5.2 and 5.3 for Yangtze River Delta and Jingjinji megalopolis.

Comparing the spatial location of these changes (Fig. 5.9), it becomes apparent that most construction activities has occurred far away from core urban areas, in airports, factories, ports and villa districts.

5.3.2 Case 2: Lombardy Region, Italy

Applying now the same procedure to the Lombardy urban cluster, it is possible to appreciate (see Fig. 5.12) that built-up zones in the Milan metropolitan area are spatially compact and homogeneous. There is no clear distinction between Varese, Como, Milan, Bergamo and Brescia. This suggests that the urbanization of Great Milan is mature, with a high urbanization level, above 70%. The very low growth rate results in few changes in both

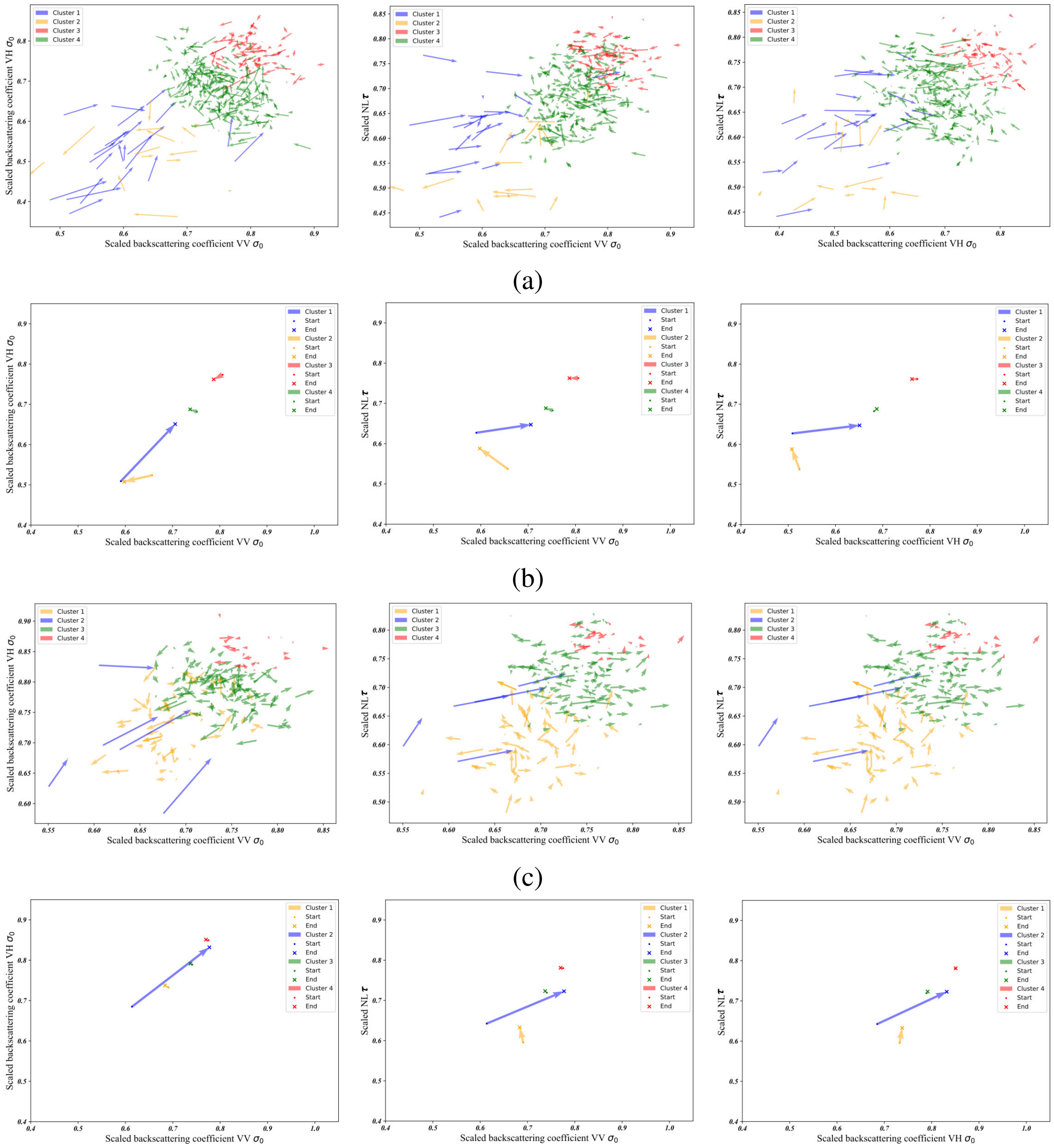

(a)

(b)

(c)

(d)

Figure 5.6: Vector analysis for 4-component clusters applied to the Jingjinji and Yangtze River Delta megalopolis: (a, c) plotting a subset of points; (b, d) plotting only cluster centers.

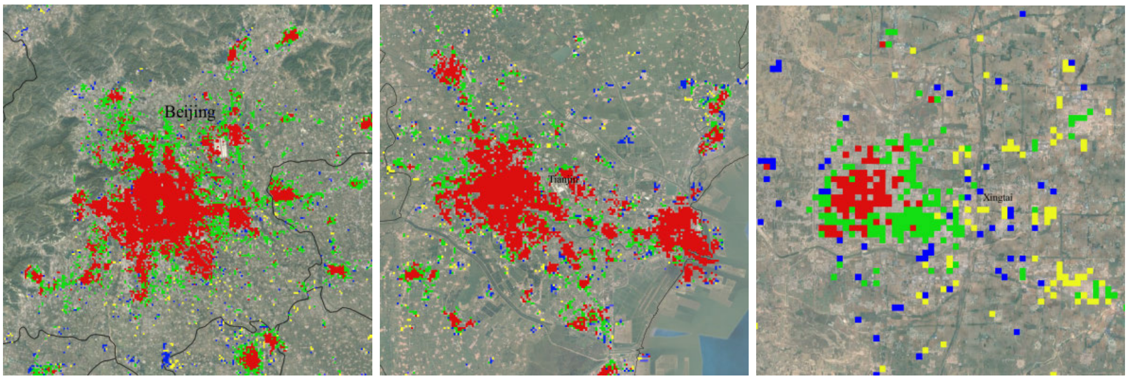

(a) Beijing (b) Tianjin (c) Xingtai

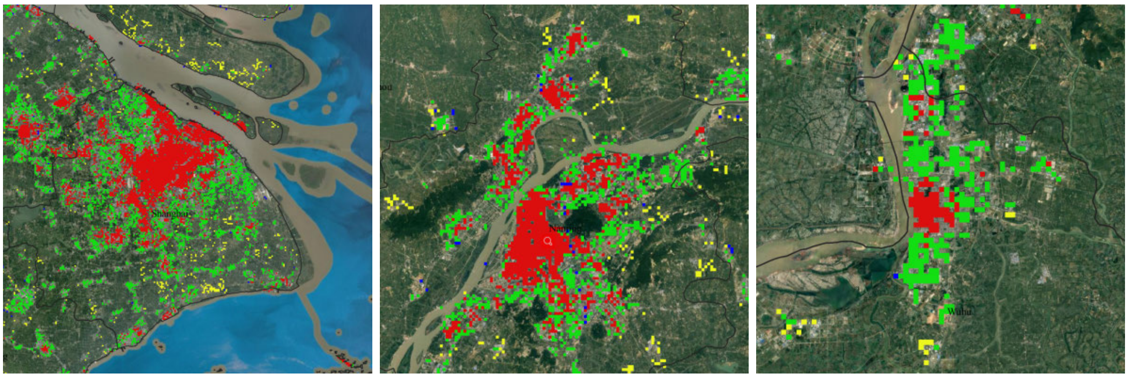

(d) Shanghai (e) Nanjing (f) Wuhu

Figure 5.7: 4-component clusters for multiple cities in the Jingjinji megalopolis.

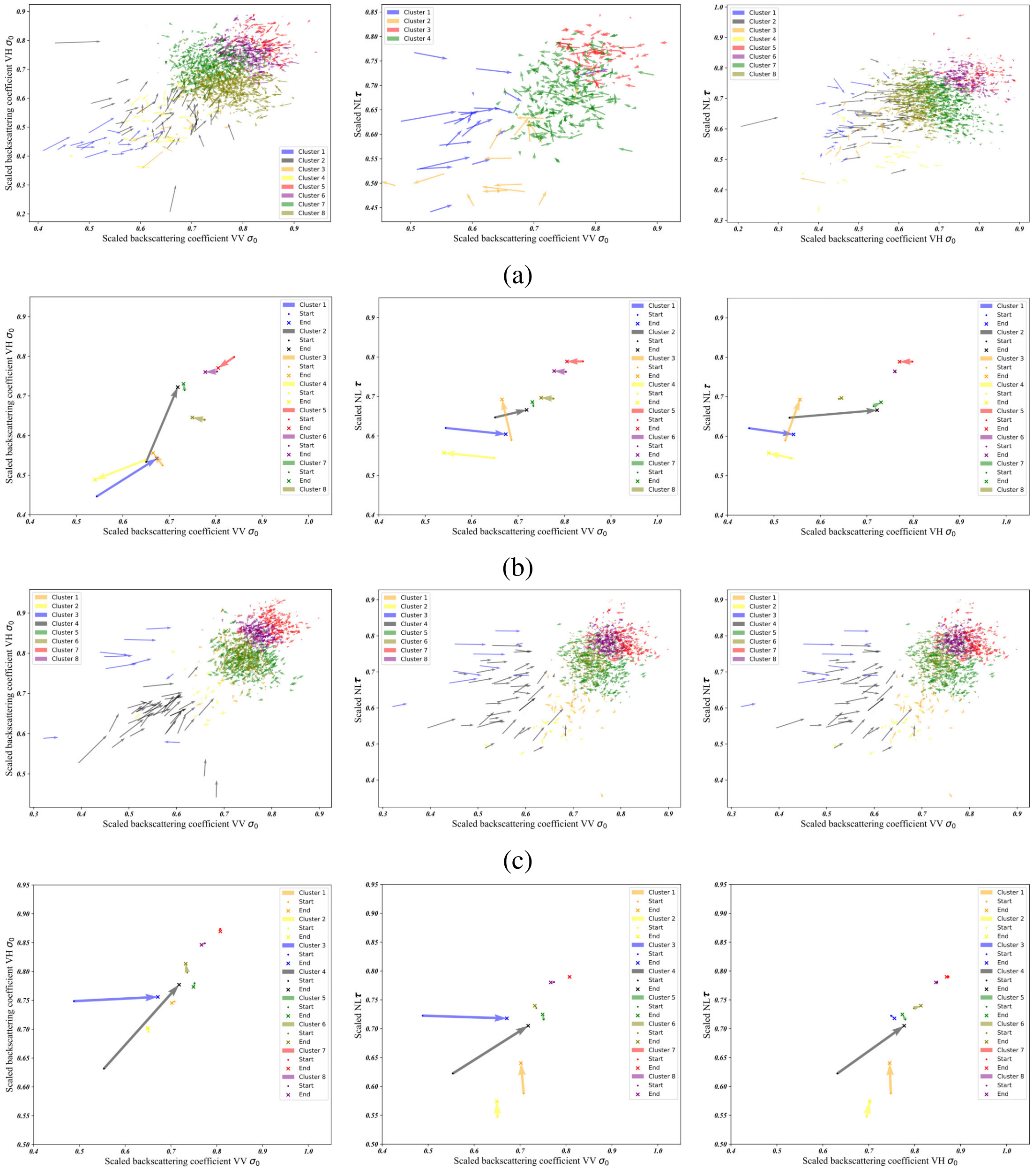

(a)

(b)

(c)

(d)

Figure 5.8: Vector analysis for 8-component clusters for the Jingjinji and Yangtze River Delta megalopolis: (a, c) using a subset of points; (b, d) using only cluster centers.

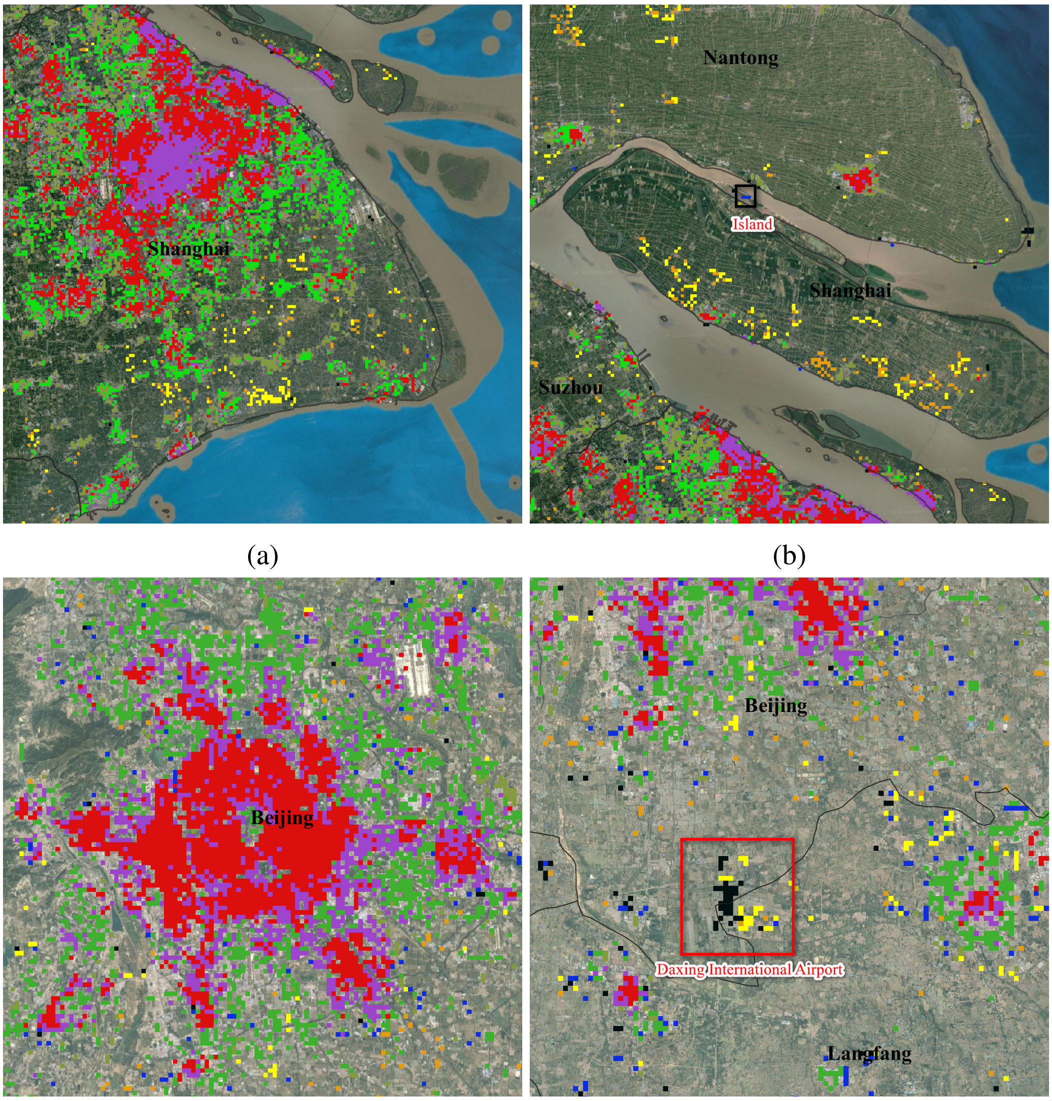

(a) (b)

(c) (d)

Figure 5.9: The spatial location of changes inside and outside urban areas: (a) the 8-component clustering map of (a) the main urban area of Shanghai; (b) small settlements far from it in the island in Yangtze River Delta; (c) the main urban area of Beijing; (d) small settlements far it (the black patch inside the red rectangle is the construction site of Beijing Daxing International Airport).

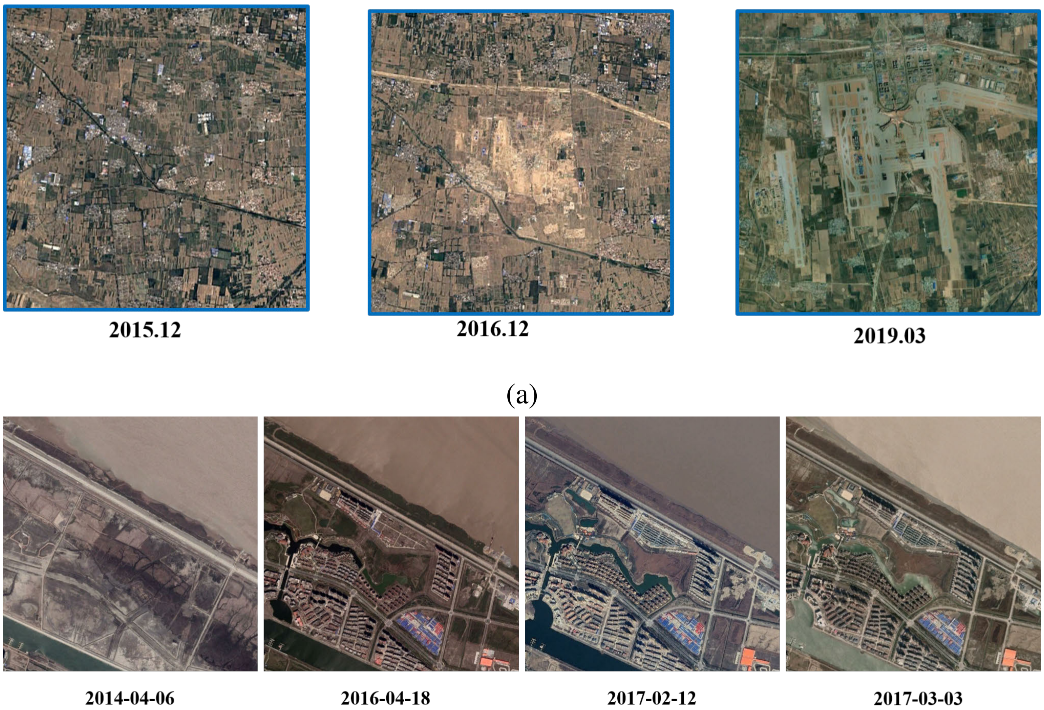

(a)

(b)

Figure 5.10: Validating changes with Google Earth History Images:(a) Gogle Earth History Images of Beijing Daxing International Airport in Fig. 5.9d; (b) Google Earth History Images of the island in the Yangtze River Delta in Fig. 5.9b.

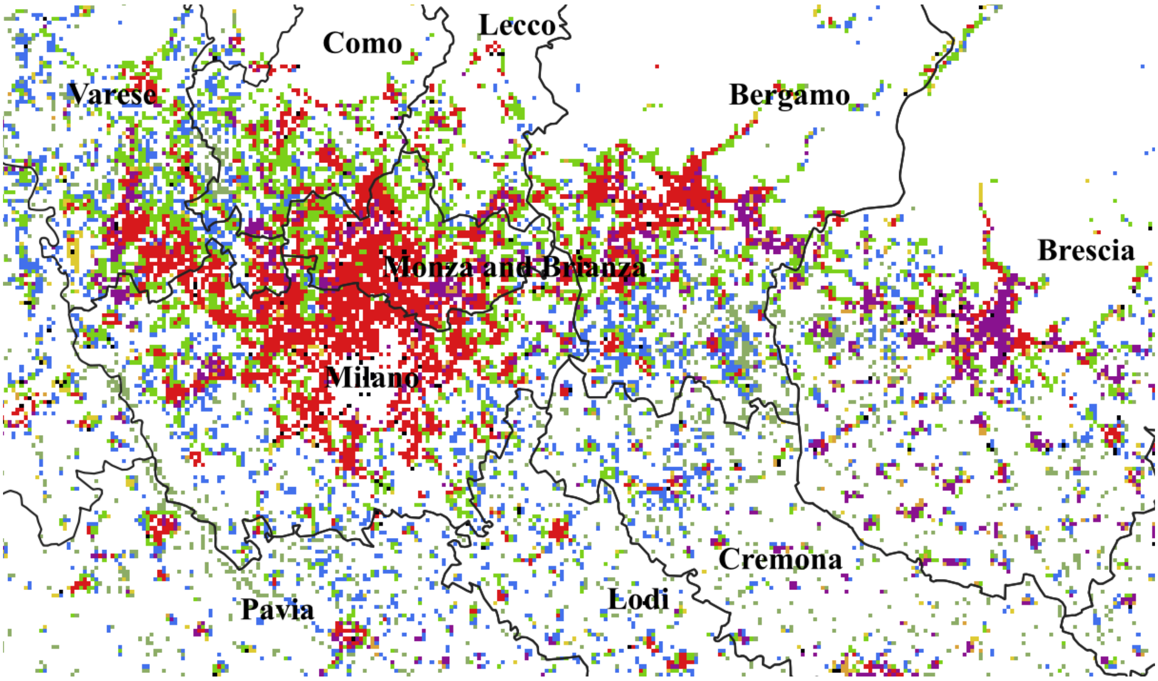

Figure 5.11: The 8-components change pattern of the urban cluster in the Lombardy region of Italy

Table 5.2: Interpretation of change patterns in the Yangtze River Delta

Cluster	Initial state	Change description	Spatial description	Interpretation
Blue	High value in NL τ, low in backscattering power σ_0	10-20% increase in VV σ_0 Almost no change in NL τ and VH σ_0	Far away from urban area/river side/container terminal	Near complete construction of building blocks
Black	Median value in NL τ and backscattering powerσ_0	About 10-20% increase in VV σ_0 and VH σ_0 ,and 5-10% increase in NL τ	Sea side Seaside villas/ container terminal/ urban-rural fringe area	Construction of multi-storey and medium height houses
Orange	Medium or larger value in NL τ,medium or larger value in backscattering powerσ_0	About 1-5% increase NLτ, and almost no change in VV $\sigma_0$and VH σ_0	Rural areas	Relative high density of low-rise residential building blocks
Yellow	Medium value in NL τ and or medium value in backscattering powerσ_0	About 1-5% increase NL τ, and almost no change in VVσ_0 and VH σ_0	Rural areas	Relative low density of low-rise residential building blocks

the SAR backscattering σ_0 and the nighttime light intensity (Fig. 5.13). Nevertheless, the black clustering still shows some minor changes caused by single building construction and maintenance (see Fig. 5.15).

5.3.3 Case 3: Nigeria and its coastal cities

As for Nigeria, the 8-clustering results in this area show peculiar building density and spatial configurations of these changes, different, as expected, from those for Chinese megalopolis.

In this geographical area, the backscattered coefficient in core urban areas, represented by purple and red clusters, is below a relative value of 0.7, much smaller than the corresponding values for the cities in Chinese megalopolis. These low values possibly indicate difference in building density. For instance, in China more high-rise buildings are built than in other parts of the world, and this leads to larger backscattering coefficients.

The change vectors of the black cluster, increasing in VV and VH backscattering power in figure 5.13 and 5.15, indicate frequent urban construction activities. However, the wide-range value of the scattering intensity and relatively high in value of NL at the starting date suggests that the changes may have possibly happened inside urban core built-up areas

Table 5.3: Interpretation of change patterns in the Jingjinji megalopolis

Cluster	Initial state	Change description	Spatial description	Interpretation
Blue	Medium value in NL τ,low in backscattering power σ_0	About 10-15% increase in VVσ_0 and VH σ_0 ,and 1-5% decrease in NL τ and VH σ_0	urban-rural fringe area or away from urban areas	Change from low-rise to high rise/residential extensions
Black	Medium or larger value in NLτ,medium or larger value in backscattering powerσ_0	About 10-20% increase in VVσ_0 and more in VH σ_0 ,and 1-5% increase in NLτ	Sea side and away from urban areas	New construction, such as factories and the new Beijing Daxing international airport
Orange	Medium value in NLτ and in backscattering powerσ_0	About 1-5% decrease in VVσ_0 and increase in VH σ_0 ,and 10% increase in NLτ	Rural residents in countryside	Towns without obvious construction activities
Yellow	Medium or lower value in NLτ,medium value in backscattering powerσ_0	About 5-10% decrease in VVσ_0 and more in VH σ_0, and almost no change in NLτ	Away from urban areas	Construction of airfield runways/new towns

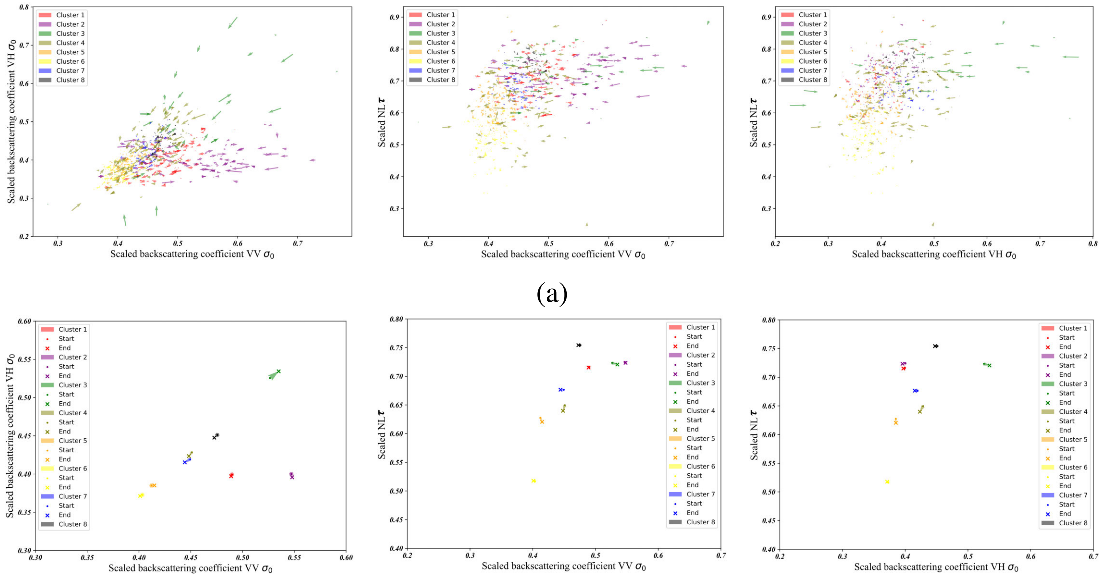

(a)

(b)

Figure 5.12: Vector analysis for 8-component clusters for Milan metropolitan area: (a) using a subset of points; (b) using only cluster centers.

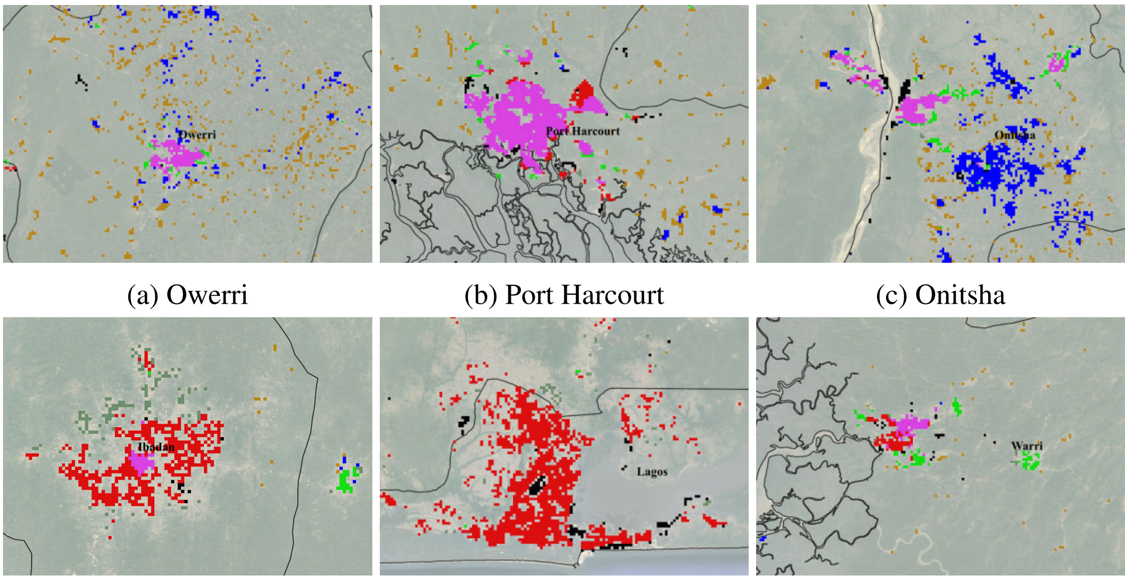

(a) Owerri (b) Port Harcourt (c) Onitsha

(d) Ibadan (e) Lagos (f) Warri

Figure 5.13: The 8-components change patterns for coastal cities in Nigeria.

and suburban built-up areas (as confirmed in Fig. 5.14b) rather than outside the urban fringes as urban expansion, as typical in China. There are oil wells and refinery facilities, recognizable as black points far away from cities, with burning gas, singled out because of their very intense lights. The clustered pattern of blue and yellow vectors is recognized as rural areas and small towns (5.14c) with great numerical fluctuation in NL. Although these large rural areas are continuous spatially and can be easily recognized as urban area, but lighting infrastructure is very backward.

Aiming at validating the extraction of urban extents implemented on Google Earth Engine (GEE), a few urban polygons, referring to buildings and streets, and some non-urban polygons, referring to forests, farmlands etc., were collected, exploiting the open source map collection in OpenStreetMap. The mapping accuracy values for the extracted megalopolis extents with respect to these ground truth are shown in table 5.4. Additionally, 30 change polygons referring to building constructions or demolitions were also collected in the different test sites, and compared with the areas belonging to clusters recognized as changes. To verify each of these ground truth patches, a visual interpretation was performed by means of Google Earth historical images. Finally, to validate the changes detected by the proposed approach, the ratio of correctly detected areas to the total number of samples (30) was computed. The results show that the proposed unsupervised approach is reasonably effective. However, the final detection accuracy may greatly depend on the urban extents extracted in the initial processing step.

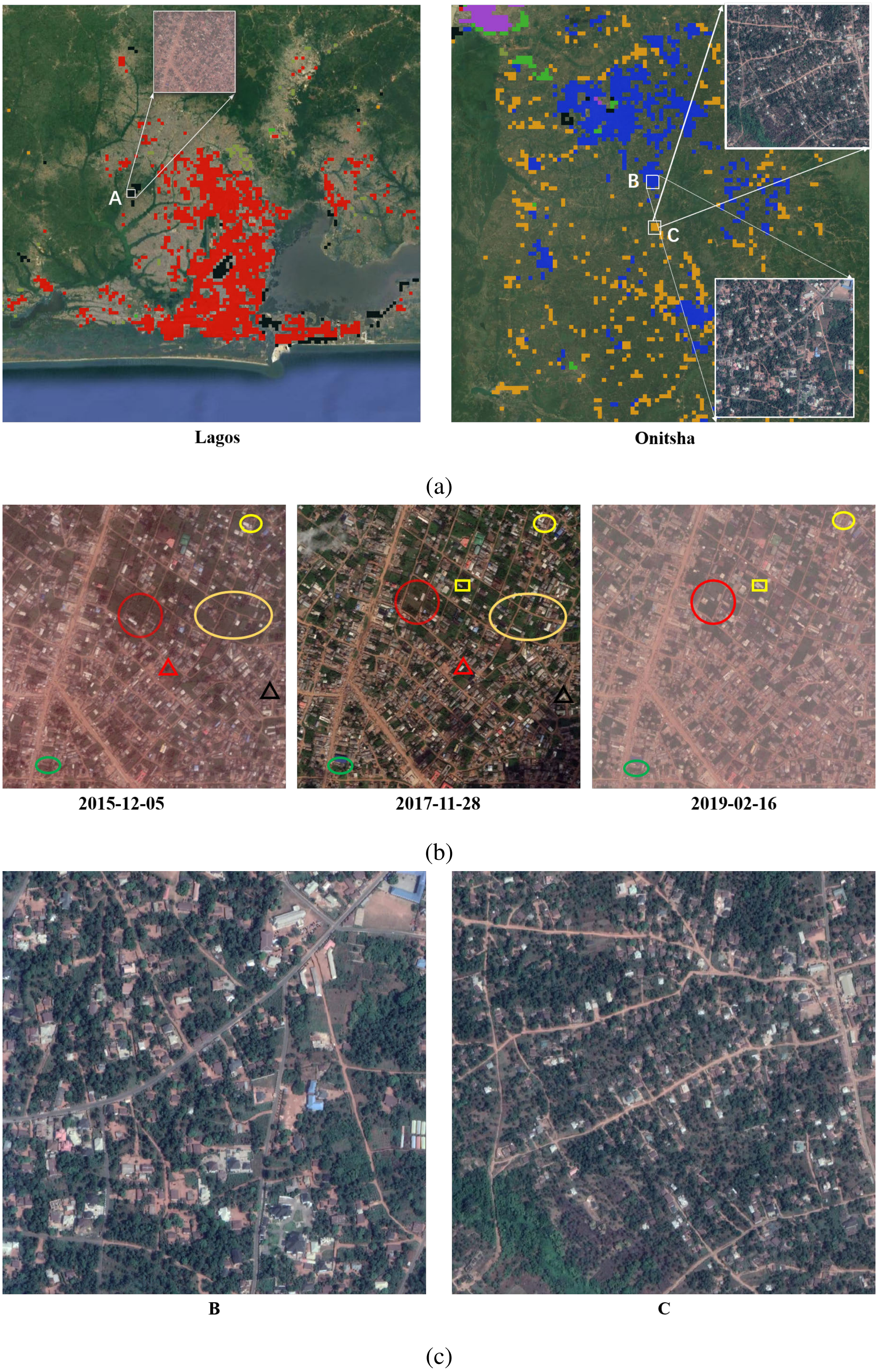

Lagos **Onitsha**

(a)

2015-12-05 **2017-11-28** **2019-02-16**

(b)

B **C**

(c)

Figure 5.14: Google Earth images of selected patches in Nigeria: (a) location of selected patches; (b) The density change of buildings visualized by Google Earth Images. (c) Google Earth Images of patches B and C.

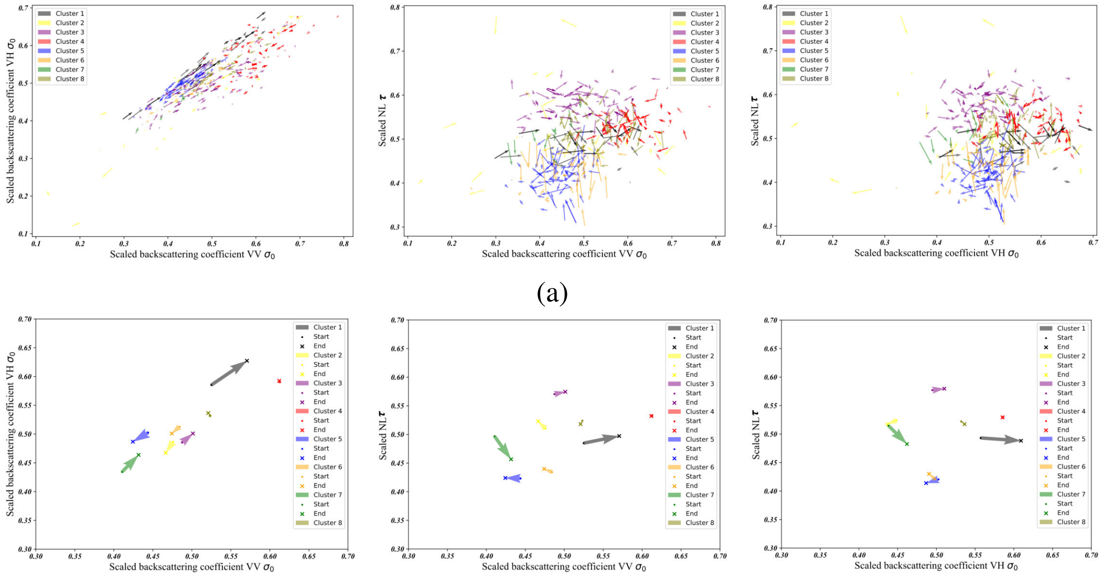

(a)

(b)

Figure 5.15: Vector analysis for 8-component clusters for cities in Nigeria: (a) using a subset of points; (b) using only cluster centers.

Table 5.4: Quantitative validation indexes for the urban extents and the detected change clusters.

	Urban extents		Change detection	
Megalopolis	OA(/100%)	$Kappa$	Cluster	Detected Rate (/100%)
YRD	98.61	0.9289	3/4	86.67
J J J	96.51	0.8645	1/2/4	83.33
Nigeria	88.06	0.7632	1	76.67
Lombardy	95.51	0.9078	-	-

5.4 Conclusions

In this work, the object-oriented vector analysis according to the extracted clusters by hierarchical bi-clustering shows that the clusters generated by the proposed approach are interpretable as meaningful temporal and spatial patterns. We tested the approach over fast-developing, like cities in China and Nigeria, and developed cities, Lombardy Region in Italy, using multi-polarization SAR and Nighttime light data. The results show the effectiveness of proposed method in mapping multi-pattern change using remote sensing data of heterogeneous sources, even without determining the number of clusters.

1. The implemented hierarchical bi-clustering producer leads to more reliable clusters and highlights interesting urban change patterns referring to both construction/demolition of built-up structures and changes in the economic activity, indicated by the nighttime lights.

2. Due to the consideration of the initial states of the temporal change, detected patterns are clearly differentiated among core urban and suburban areas, as well as with respect to the areas beyond urban outskirts. Specifically, very new development city zones are singled out and clearly recognized.

3. There exists a high correlation between VV and VH polarization when downscaling Sentinel-1 SAR data to the nighttime light spatial resolution, suggesting that polarization is critical for analyses at the finest resolution, but not at the megacity scale.

4. Building density and infrastructure constructions are the main differences between highly-urbanized areas (e.g., Milan), median-urbanized areas (e.g., Nanjing and inner cities in china), and less-urbanized areas (e.g., Onitsha and coastal cities in Nigeria).

Chapter 6

Conclusion

This chapter provides a comprehensive review of the research carried out in these years and concludes the thesis by summarizing the novel achievements and highlighting possible future research paths.

6.1 Contributions and discussions

This thesis introduced novel approaches for the representation and analysis of intra-urban multi-pattern changes by focusing on multi-temporal fully or dual polarized SAR images, as well as their combination with nighttime light data. SAR images inherently represent precious information about urban structures, both in the horizontal and vertical dimensions, since the SAR side-looking imaging mode produces surface-scattering double-scattering, and volume-scattering phenomena. Therefore, multi-temporal SAR images are used in this thesis to detect various structural changes of buildings and artificial targets. Simultaneously, the proposed approaches are employed to map and further investigate temporal patterns of those changes, discriminating among building constructions, reconstructions, demolitions and more. Apart from the traditional comparison of the amplitude of SAR images, temporal correlation of complex values is also used to explore more sensitive changes, like building renovations. Additionally, but still In the perspective of mapping and understanding the complex phenomena related to urbanization, heterogeneous data are combined to discover spatial and temporal change patters in urban areas as a result of physical changes, but also of socio-economic activities.

From the methodological point of view, the contributions of this thesis can be listed as follows and pertain to the domain of SAR intra-urban change detection and monitoring,

- **A more efficient wide-area (intra-)urban change mapping.** Speckle noise always challenges wide-area application of SAR images, especially when considering long-term series of data. Traditional spatial-based and temporal domain denoising and pixel-wise operation consume an enormous amount of time and computing resources. The superpixel-based change method proposed in this work significantly improves the efficiency of change mapping by clustering similar pixels as a single basic object. The analysis of change images at the superpixel level is promising in mapping large-scale dynamic changes, e.g., global and regional intr-urban changes.

- **Extraction of multi-temporal patterns in urban change mapping.** Unlike previous binary-change detection and/or 2D urban change mapping studies in the last decades, in this thesis multi-temporal change patterns are extracted using multi-temporal SAR images series. These changes indicate various phenomena, such as new building constructions, reconstructions, demolitions and more. It is challenging to detect and visualize these multiple changes in an unsupervised way. This thesis achieves this goal with three strategies. 1) SAR polarimetry: full-polarization channels enable to apply polarimetric decomposition to separate double-bounce scattering and volume-scattering from scattering matrix. As a result, meaningful positive and negative changes are mapped. 2) Change patterns in the time domain: a series of temporal coherence/correlation data between subsequent SAR images is classified into several clusters, which are interpreted by analyzing time trend and fluctuation of both coherence and amplitude data. 3) Fusion of SAR and nighttime light data: changes in multi-temporal SAR images represent the physical or geometrical change of an urban entity due to urban construction and update of real estates. Changes in nighttime lights indicate socioeconomic activities. The fusion of these two sensors allows the combination of two kinds of changes and detects patterns that reflect dynamic differences inside urban areas in both the time and space domains.

- **Change-pattern mining with hierarchical bi-clustering and visualization** The challenges of fusing heterogeneous source data on wide geographical areas are a) to determine the number of change patterns explicitly and b) to visualize and illustrate the characteristics of the detected changes. In this thesis, a hierarchical bi-clustering approach is selected, implemented and validated to detect multiple changes. The approach is effective in mining multiple change patterns, and proved to be scalable to fuse data of heterogeneous sensors. A change vector visualization following the clustering explicitly illustrates multi-pattern changes, so that they can be more easily interpreted.

From the point of view of the applications, the proposed approaches have been effectively applied to monitoring urbanization for test sites in Asia, Africa, and Europe. Urban areas with different urbanization levels, climate environment, size and history have been selected and compared. The results show highly-speed urban expanding rates in developing Asian counties, like China, Vietnam, and Laos, as well as in African developing countries, like Nigeria. The also show that, simultaneously to urban expansion, intra-urban reconstruction activities occur. More specifically, results show that China's real estate development is accompanied by a large number of demolition activities. These change patterns are different according to the urban spatial structure in urban cores, suburban areas, and urban-rural fringes. As for highly-urbanized cities in Europe, instead, almost no full building blocks and mostly single-building constructions happen and are detected.

From the point of view of the performances, the superpixel-based change detection and time-series change analysis were implemented on a computing platform with four-core Intel Processor i7-6700HQ at 2.6GHz, and 32Gb RAM. The use of superpixels greatly improves the training velocity, and makes it possible to apply the proposed approach to wide geographical areas, even with HR data. The time-series change analysis is based on computing adjacent coherence maps, and this step is more demanding, but it consumes less resources than performing a full SAR Interferometry analysis. Finally, the combined utilization of S-1 and NL data has implemented on the Google Earth Engine cloud platform, which allows on-line analyses of huge amounts of data, at the expense of a less performing computational velocity.

6.2 Future developments

First of all, apart from the urban applications mentioned in this thesis, the proposed approaches can also be transferred in mapping change of other land class.

Moreover, and according to results in this thesis, there still exist challenges in practicality and applicability of the proposed methods. For instance, in this thesis only two adjacent PolSAR images are used to produce a superpixel change image, but approaches with temporal series at the superpixel level could also be considered. Additionally, more urban areas and different environments (e.g., areas with complicated topography, mountain or country towns) should be considered to check the applicability of these methods.

Another important point when evaluating the use of SAR and nighttime lights is that the current single scale fusion of heterogeneous data causes partial degradation of the image information as a result of upscaling to the coarser spatial resolution of nighttime light data. Multi-scale representation and fusion approaches should be developed in the future to maintain the full information available in the original data.

From the point of view of the classification, unsupervised or semi-automatic change detection is a promising approach. However, its validation so far depends on visual interpretation, hence from the availability of reference VHR optical imagery and user's prior knowledge. Therefore, to objectively evaluate the performance of the method, simulated data and more reference data should be looked for.

Appendix A

SAR polarimetry

For Quad-PolSAR images, the polarimetric scattering target vectors k_3 and Ω_3 are constructed from the classical 2x2 coherent Sinclair matrix **S**

$$\mathbf{S} = \begin{bmatrix} S_{hh} & S_{hv} \\ S_{vh} & S_{vv} \end{bmatrix} \tag{A.1}$$

$$\Omega_3 = \frac{1}{\sqrt{2}} \begin{bmatrix} S_{hh} & \sqrt{2} S_{hv} & S_{vv} \end{bmatrix}^T \tag{A.2}$$

$$k_3 = \frac{1}{\sqrt{2}} \begin{bmatrix} S_{hh} + S_{vv} & S_{hh} - S_{vv} & 2S_{hv} \end{bmatrix}^T \tag{A.3}$$

The coherency matrix $T3$ and covariance $C3$ are caculated as,

$$\begin{aligned} T3 &= k_3 * k_3^{*T} \\ &= \frac{1}{2} \begin{bmatrix} \langle | S_{hh} + S_{vv} |^2 \rangle & \langle (S_{hh} + S_{vv})(S_{hh} + S_{vv})^* \rangle & 2\langle (S_{hh} + S_{vv}) S_{hv}^* \rangle \\ \langle (S_{hh} - S_{vv})(S_{hh} + S_{vv})^* \rangle & \langle | S_{hh} - S_{vv} |^2 \rangle & 2\langle (S_{hh} - S_{vv}) S_{hv}^* \rangle \\ 2\langle S_{hv} (S_{hh} + S_{vv})^* \rangle & 2\langle S_{hv} (S_{hh} - S_{vv})^* \rangle & 4\langle | S_{hv} |^2 \rangle \end{bmatrix} \end{aligned} \tag{A.4}$$

$$C3 = \Omega_3 * \Omega_3^{*T} = \begin{bmatrix} \langle | S_{hh} |^2 \rangle & \sqrt{2}\langle S_{hh} S_{hv}^* \rangle & \langle S_{hh} S_{vv}^* \rangle \\ \sqrt{2}\langle S_{hv} S_{hh}^* \rangle & 2\langle | S_{hv} |^2 \rangle & \sqrt{2}\langle S_{hv} S_{vv}^* \rangle \\ \langle S_{vv} S_{hh}^* \rangle & \sqrt{2}\langle S_{vv} S_{hv}^* \rangle & \langle | S_{vv} |^2 \rangle \end{bmatrix} \tag{A.5}$$

The denosing is based on coherency or covariance matrix.

For Dual-PolSAR images(Sentinel-1 SAR), the the polarimetric scattering target vectors k_2 and Ω_2 are

$$\Omega_2 = \begin{bmatrix} S_{vv} & S_{hv} \end{bmatrix}^T \tag{A.6}$$

$$k_2 = \begin{bmatrix} S_{vv} + S_{vh} & S_{vv} - S_{vh} \end{bmatrix}^T \tag{A.7}$$

and corresponding coherency $T2$ or covariance matrix $C2$ are,

$$\begin{aligned} T2 &= k_2 * k_2^{*T} \\ &= \begin{bmatrix} \langle \mid S_{vv} + S_{vh} \mid^2 \rangle & \langle (S_{vv} + S_{vh})(S_{vv} - S_{vh})^* \rangle \\ \langle (S_{vv} - S_{vh})(S_{vv} + S_{vh})^* \rangle & \langle \mid S_{vv} - S_{vh} \mid^2 \rangle \end{bmatrix} \end{aligned} \tag{A.8}$$

$$C2 = \Omega_2 * \Omega_2^{*T} = \begin{bmatrix} \langle \mid S_{vv} \mid^2 \rangle & \langle S_{vv} S_{vh}^* \rangle \\ \langle S_{vv}^* S_{vh} \rangle & \langle \mid S_{vh} \mid^2 \rangle \end{bmatrix} \tag{A.9}$$

References

[1] H. Taubenböck, T. Esch, A. Felbier, M. Wiesner, A. Roth, and S. Dech, “Monitoring urbanization in mega cities from space,” *Remote sensing of Environment*, vol. 117, pp. 162–176, 2012.

[2] K. C. Seto, C. Woodcock, C. Song, X. Huang, J. Lu, and R. Kaufmann, “Monitoring land-use change in the Pearl River Delta using Landsat TM,” *International Journal of Remote Sensing*, vol. 23, no. 10, pp. 1985–2004, 2002.

[3] D. Mage, G. Ozolins, P. Peterson, A. Webster, R. Orthofer, V. Vandeweerd, and M. Gwynne, “Urban air pollution in megacities of the world,” *Atmospheric Environment*, vol. 30, no. 5, pp. 681–686, 1996.

[4] S. Phinn, M. Stanford, P. Scarth, A. Murray, and P. Shyy, “Monitoring the composition of urban environments based on the vegetation-impervious surface-soil (VIS) model by subpixel analysis techniques,” *International Journal of Remote Sensing*, vol. 23, no. 20, pp. 4131–4153, 2002.

[5] Y.-y. Li, H. Zhang, and W. Kainz, “Monitoring patterns of urban heat islands of the fast-growing Shanghai metropolis, China: Using time-series of Landsat TM/ETM+ data,” *International Journal of Applied Earth Observation and Geoinformation*, vol. 19, pp. 127–138, 2012.

[6] T. Ramachandra, A. Bharath, and M. Sowmyashree, “Monitoring urbanization and its implications in a mega city from space: Spatiotemporal patterns and its indicators,” *Journal of environmental management*, vol. 148, pp. 67–81, 2015.

[7] D. Lu, E. Moran, and S. Hetrick, “Detection of impervious surface change with multitemporal Landsat images in an urban–rural frontier,” *ISPRS Journal of Photogrammetry and Remote Sensing*, vol. 66, no. 3, pp. 298–306, 2011.

[8] M. E. Bauer, N. J. Heinert, J. K. Doyle, and F. Yuan, “Impervious surface mapping and change monitoring using Landsat remote sensing,” in *ASPRS annual conference*

proceedings, vol. 10, American Society for Photogrammetry and Remote Sensing Bethesda, MD, 2004.

[9] J. O. Sexton, X.-P. Song, C. Huang, S. Channan, M. E. Baker, and J. R. Townshend, "Urban growth of the Washington, DC–Baltimore, MD metropolitan region from 1984 to 2010 by annual, Landsat-based estimates of impervious cover," *Remote Sensing of Environment*, vol. 129, pp. 42–53, 2013.

[10] H. Letu, M. Hara, G. Tana, and F. Nishio, "A saturated light correction method for DMSP/OLS nighttime satellite imagery," *IEEE Transactions on Geoscience and Remote Sensing*, vol. 50, no. 2, pp. 389–396, 2011.

[11] X. Li, X. Chen, Y. Zhao, J. Xu, F. Chen, and H. Li, "Automatic intercalibration of night-time light imagery using robust regression," *Remote sensing letters*, vol. 4, no. 1, pp. 45–54, 2013.

[12] T. A. Croft, "Nighttime images of the earth from space," *Scientific American*, vol. 239, no. 1, pp. 86–101, 1978.

[13] C. H. Doll, J.-P. Muller, and C. D. Elvidge, "Night-time imagery as a tool for global mapping of socioeconomic parameters and greenhouse gas emissions," *AMBIO: a Journal of the Human Environment*, vol. 29, no. 3, pp. 157–163, 2000.

[14] H. J. Kramer, *Observation of the Earth and its Environment: Survey of Missions and Sensors*. Springer Science & Business Media, 2002.

[15] J. Wu, Z. Wang, W. Li, and J. Peng, "Exploring factors affecting the relationship between light consumption and GDP based on DMSP/OLS nighttime satellite imagery," *Remote Sensing of Environment*, vol. 134, pp. 111–119, 2013.

[16] C. D. Elvidge, K. E. Baugh, E. A. Kihn, H. W. Kroehl, E. R. Davis, and C. W. Davis, "Relation between satellite observed visible-near infrared emissions, population, economic activity and electric power consumption," *International Journal of Remote Sensing*, vol. 18, no. 6, pp. 1373–1379, 1997.

[17] K. Shi, B. Yu, Y. Huang, Y. Hu, B. Yin, Z. Chen, L. Chen, and J. Wu, "Evaluating the ability of NPP-VIIRS nighttime light data to estimate the gross domestic product and the electric power consumption of China at multiple scales: A comparison with DMSP-OLS data," *Remote Sensing*, vol. 6, no. 2, pp. 1705–1724, 2014.

[18] M. M. Bennett and L. C. Smith, "Using multitemporal night-time lights data to compare regional development in Russia and China, 1992–2012," *International Journal of Remote Sensing*, vol. 38, no. 21, pp. 5962–5991, 2017.

[19] Z. Dai, Y. Hu, and G. Zhao, "The suitability of different nighttime light data for GDP estimation at different spatial scales and regional levels," *Sustainability*, vol. 9, no. 2, p. 305, 2017.

[20] C. He, P. Shi, J. Li, J. Chen, Y. Pan, J. Li, L. Zhuo, and T. Ichinose, "Restoring urbanization process in China in the 1990s by using non-radiance-calibrated DMSP/OLS nighttime light imagery and statistical data," *Chinese Science Bulletin*, vol. 51, no. 13, pp. 1614–1620, 2006.

[21] Z. Liu, C. He, Q. Zhang, Q. Huang, and Y. Yang, "Extracting the dynamics of urban expansion in China using DMSP-OLS nighttime light data from 1992 to 2008," *Landscape and Urban Planning*, vol. 106, no. 1, pp. 62–72, 2012.

[22] Y. Yao, D. Chen, L. Chen, H. Wang, and Q. Guan, "A time series of urban extent in China using DSMP/OLS nighttime light data," *PloS one*, vol. 13, no. 5, p. e0198189, 2018.

[23] B. CHAI, P. LI, R. ZHANG, and P. ZHAO, "Urban Expansion Extraction Using Landsat Series Data and DMSP/OLS Nighttime Light Data: A Case Study of Tianjin Area," *Acta Scientiarum Naturalium Universitatis Pekinensis*, no. 3, p. 11, 2016.

[24] J. C. Duque, N. Lozano-Gracia, J. E. Patino, P. Restrepo, and W. A. Velasquez, *Spatio-Temporal Dynamics of Urban Growth in Latin American Cities: An Analysis Using Nighttime Lights Imagery*. The World Bank, 2019.

[25] Y. Ju, I. Dronova, Q. Ma, and X. Zhang, "Analysis of urbanization dynamics in mainland China using pixel-based night-time light trajectories from 1992 to 2013," *International Journal of Remote Sensing*, vol. 38, no. 21, pp. 6047–6072, 2017.

[26] T. Ma, Y. Zhou, C. Zhou, S. Haynie, T. Pei, and T. Xu, "Night-time light derived estimation of spatio-temporal characteristics of urbanization dynamics using DMSP/OLS satellite data," *Remote Sensing of Environment*, vol. 158, pp. 453–464, 2015.

[27] Q. Zheng, R. Jiang, K. Wang, L. Huang, Z. Ye, M. Gan, and B. Ji, “Monitoring the trajectory of urban nighttime light hotspots using a Gaussian volume model,” *International journal of applied earth observation and geoinformation*, vol. 65, pp. 24–34, 2018.

[28] B. Pandey, P. Joshi, and K. C. Seto, “Monitoring urbanization dynamics in India using DMSP/OLS night time lights and SPOT-VGT data,” *International Journal of Applied Earth Observation and Geoinformation*, vol. 23, pp. 49–61, 2013.

[29] R. Welch, “Monitoring urban population and energy utilization patterns from satellite data,” *Remote sensing of Environment*, vol. 9, no. 1, pp. 1–9, 1980.

[30] Y. Xie and Q. Weng, “Spatiotemporally enhancing time-series DMSP/OLS nighttime light imagery for assessing large-scale urban dynamics,” *ISPRS Journal of Photogrammetry and Remote Sensing*, vol. 128, pp. 1–15, 2017.

[31] Y. Xie, Q. Weng, and P. Fu, “Temporal variations of artificial nighttime lights and their implications for urbanization in the conterminous United States, 2013–2017,” *Remote Sensing of Environment*, vol. 225, pp. 160–174, 2019.

[32] X. Li, L. Ge, and X. Chen, “Detecting Zimbabwe’s decadal economic decline using nighttime light imagery,” *Remote Sensing*, vol. 5, no. 9, pp. 4551–4570, 2013.

[33] Q. Zheng, J. Deng, R. Jiang, K. Wang, X. Xue, Y. Lin, Z. Huang, Z. Shen, J. Li, and A. R. Shahtahmassebi, “Monitoring and assessing “ghost cities” in Northeast China from the view of nighttime light remote sensing data,” *Habitat International*, vol. 70, pp. 34–42, 2017.

[34] H. Lu, C. Zhang, G. Liu, X. Ye, and C. Miao, “Mapping China’s Ghost Cities through the Combination of Nighttime Satellite Data and Daytime Satellite Data,” *Remote Sensing*, vol. 10, no. 7, p. 1037, 2018.

[35] Y. Liu, Y. Wang, J. Peng, Y. Du, X. Liu, S. Li, and D. Zhang, “Correlations between urbanization and vegetation degradation across the world’s metropolises using DMSP/OLS nighttime light data,” *Remote Sensing*, vol. 7, no. 2, pp. 2067–2088, 2015.

[36] S. Pok, B. Matsushita, and T. Fukushima, “An easily implemented method to estimate impervious surface area on a large scale from MODIS time-series and improved DMSP-OLS nighttime light data,” *ISPRS journal of photogrammetry and remote sensing*, vol. 133, pp. 104–115, 2017.

[37] S. Keola, M. Andersson, and O. Hall, "Monitoring economic development from space: using nighttime light and land cover data to measure economic growth," *World Development*, vol. 66, pp. 322–334, 2015.

[38] R. D. Johnson and E. Kasischke, "Change vector analysis: A technique for the multispectral monitoring of land cover and condition," *International Journal of Remote Sensing*, vol. 19, no. 3, pp. 411–426, 1998.

[39] X.-P. Song, J. O. Sexton, C. Huang, S. Channan, and J. R. Townshend, "Characterizing the magnitude, timing and duration of urban growth from time series of Landsat-based estimates of impervious cover," *Remote Sensing of Environment*, vol. 175, pp. 1–13, 2016.

[40] J. Quan, W. Zhan, Y. Chen, M. Wang, and J. Wang, "Time series decomposition of remotely sensed land surface temperature and investigation of trends and seasonal variations in surface urban heat islands," *Journal of Geophysical Research: Atmospheres*, vol. 121, no. 6, pp. 2638–2657, 2016.

[41] P. Fu and Q. Weng, "A time series analysis of urbanization induced land use and land cover change and its impact on land surface temperature with Landsat imagery," *Remote Sensing of Environment*, vol. 175, pp. 205–214, 2016.

[42] Q. Li, L. Lu, Q. Weng, Y. Xie, and H. Guo, "Monitoring urban dynamics in the southeast USA using time-series DMSP/OLS nightlight imagery," *Remote Sensing*, vol. 8, no. 7, p. 578, 2016.

[43] E. S. Krayenhoff and J. A. Voogt, "A microscale three-dimensional urban energy balance model for studying surface temperatures," *Boundary-Layer Meteorology*, vol. 123, no. 3, pp. 433–461, 2007.

[44] P. P.-J. Yang, S. Y. Putra, and W. Li, "Viewsphere: a GIS-based 3D visibility analysis for urban design evaluation," *Environment and Planning B: Planning and Design*, vol. 34, no. 6, pp. 971–992, 2007.

[45] S. Wang, Y. Tian, Y. Zhou, W. Liu, and C. Lin, "Fine-scale population estimation by 3D reconstruction of urban residential buildings," *Sensors*, vol. 16, no. 10, p. 1755, 2016.

[46] B. Leng, Z. Xiong, and X. Fu, "A 3D shape retrieval framework for 3D smart cities," *Frontiers of Computer Science in China*, vol. 4, no. 3, pp. 394–404, 2010.

[47] D. Poli, F. Remondino, E. Angiuli, and G. Agugiaro, “Radiometric and geometric evaluation of GeoEye-1, WorldView-2 and Pléiades-1A stereo images for 3D information extraction,” *ISPRS Journal of Photogrammetry and Remote Sensing*, vol. 100, pp. 35–47, 2015.

[48] A. El Garouani, A. Alobeid, and S. El Garouani, “Digital surface model based on aerial image stereo pairs for 3D building,” *International Journal of Sustainable Built Environment*, vol. 3, no. 1, pp. 119–126, 2014.

[49] R. Wang, “3D building modeling using images and LiDAR: A review,” *International Journal of Image and Data Fusion*, vol. 4, no. 4, pp. 273–292, 2013.

[50] M. Baldo, C. Bicocchi, U. Chiocchini, D. Giordan, and G. Lollino, “LIDAR monitoring of mass wasting processes: The Radicofani landslide, Province of Siena, Central Italy,” *Geomorphology*, vol. 105, no. 3-4, pp. 193–201, 2009.

[51] P. Hobbs, A. Gibson, L. Jones, C. Pennington, G. Jenkins, S. Pearson, and K. Freeborough, “Monitoring coastal change using terrestrial LiDAR,” *Geological Society, London, Special Publications*, vol. 345, no. 1, pp. 117–127, 2010.

[52] T.-A. Teo and T.-Y. Shih, “Lidar-based change detection and change-type determination in urban areas,” *International journal of remote sensing*, vol. 34, no. 3, pp. 968–981, 2013.

[53] T. T. Vu, M. Matsuoka, and F. Yamazaki, “LIDAR-based change detection of buildings in dense urban areas,” in *IGARSS 2004. 2004 IEEE International Geoscience and Remote Sensing Symposium*, vol. 5, pp. 3413–3416, IEEE, 2004.

[54] B. Yang and C. Chen, “Automatic registration of UAV-borne sequent images and LiDAR data,” *ISPRS Journal of Photogrammetry and Remote Sensing*, vol. 101, pp. 262–274, 2015.

[55] C. Armenakis, Y. Gao, and G. Sohn, “Co-registration of lidar and photogrammetric data for updating building databases,” *ISPRS Arch., Haifa, Israel*, vol. 38, pp. 96–100, 2010.

[56] T. Butkiewicz, R. Chang, Z. Wartell, and W. Ribarsky, “Visual analysis and semantic exploration of urban lidar change detection,” in *Computer Graphics Forum*, vol. 27, pp. 903–910, Wiley Online Library, 2008.

[57] J. Tian and P. Reinartz, "Multitemporal 3D change detection in urban areas using stereo information from different sensors," in *2011 International Symposium on Image and Data Fusion*, pp. 1–4, IEEE, 2011.

[58] H. Chaabouni-Chouayakh, T. Krauss, P. d'Angelo, and P. Reinartz, "3D change detection inside urban areas using different digital surface models," *International Archives of Photogrammetry, Remote Sensing and Spatial Information Sciences*, vol. 38, pp. 86–91, 2010.

[59] R. Qin, J. Tian, and P. Reinartz, "3D change detection–approaches and applications," *ISPRS Journal of Photogrammetry and Remote Sensing*, vol. 122, pp. 41–56, 2016.

[60] X. Niu and Y. Ban, "Multi-temporal RADARSAT-2 polarimetric SAR data for urban land-cover classification using an object-based support vector machine and a rule-based approach," *International journal of remote sensing*, vol. 34, no. 1, pp. 1–26, 2013.

[61] T. Esch, H. Taubenböck, A. Felbier, W. Heldens, M. Wiesner, and S. Dech, "Monitoring of global urbanization-time series analyses for mega cities based on optical and SAR data," in *2012 Second International Workshop on Earth Observation and Remote Sensing Applications*, pp. 21–25, IEEE, 2012.

[62] L. Gomez-Chova, D. Fernández-Prieto, J. Calpe, E. Soria, J. Vila, and G. Camps-Valls, "Urban monitoring using multi-temporal SAR and multi-spectral data," *Pattern Recognition Letters*, vol. 27, no. 4, pp. 234–243, 2006.

[63] D. Brunner, G. Lemoine, L. Bruzzone, and H. Greidanus, "Building height retrieval from VHR SAR imagery based on an iterative simulation and matching technique," *IEEE Transactions on Geoscience and Remote Sensing*, vol. 48, no. 3, pp. 1487–1504, 2009.

[64] R. Guida, G. Franceschetti, A. Iodice, D. Riccio, and G. Ruello, "Accuracy of building height estimation from SAR images," in *Proceedings of the IEEE International Geoscience and Remote Sensing Symposium'06*, pp. 3647–3650, 2007.

[65] G. Franceschetti, R. Guida, A. Iodice, D. Riccio, and G. Ruello, "Building Height Retrieval From Radiometric Parameters On SAR Images," 2005.

[66] F. Tupin, "Extraction of 3D information using overlay detection on SAR images," in *2003 2nd GRSS/ISPRS Joint Workshop on Remote Sensing and Data Fusion over Urban Areas*, pp. 72–76, IEEE, 2003.

[67] M. Jahangir, D. Blacknell, C. Moate, and R. Hill, “Extracting information from shadows in SAR imagery,” in *2007 International Conference on Machine Vision*, pp. 107–112, IEEE, 2007.

[68] D. Brunner, G. Lemoine, L. Bruzzone, and H. Greidanus, “Building height retrieval from VHR SAR imagery based on an iterative simulation and matching technique,” *IEEE Transactions on Geoscience and Remote Sensing*, vol. 48, no. 3, pp. 1487–1504, 2010.

[69] A. Ferro, D. Brunner, and L. Bruzzone, “Automatic detection and reconstruction of building radar footprints from single VHR SAR images,” *IEEE Transactions on Geoscience and Remote Sensing*, vol. 51, no. 2, pp. 935–952, 2012.

[70] S. R. Cloude and E. Pottier, “A review of target decomposition theorems in radar polarimetry,” *IEEE transactions on geoscience and remote sensing*, vol. 34, no. 2, pp. 498–518, 1996.

[71] K. Tang, K. Chen, L. Wang, W. Xiong, M. Jiang, and H. Wang, “A knowledge-based 3-D building reconstruction from single very high resolution SAR images,” in *2012 IEEE International Geoscience and Remote Sensing Symposium*, pp. 3604–3607, IEEE, 2012.

[72] R. Guida, A. Iodice, and D. Riccio, “Height retrieval of isolated buildings from single high-resolution SAR images,” *IEEE Transactions on Geoscience and Remote Sensing*, vol. 48, no. 7, pp. 2967–2979, 2010.

[73] L.-b. Jiang, Z. Wang, and W.-x. Yu, “Model based building height retrieval from single SAR images,” in *2011 6th IEEE Joint International Information Technology and Artificial Intelligence Conference*, vol. 1, pp. 379–384, IEEE, 2011.

[74] D. Brunner, G. Lemoine, and L. Bruzzone, “Height estimation of man made structures using hybrid VHR optical and SAR imagery,” in *Proc. EARSeL Joint Workshop, Remote Sens.—New Challenges of High Resolution*, pp. 186–193, 2008.

[75] A. Ferro, D. Brunner, L. Bruzzone, and G. Lemoine, “On the relationship between double bounce and the orientation of buildings in VHR SAR images,” *IEEE Geoscience and Remote Sensing Letters*, vol. 8, no. 4, pp. 612–616, 2011.

[76] K. Iribe and M. Sato, “Analysis of polarization orientation angle shifts by artificial structures,” *IEEE Transactions on Geoscience and remote sensing*, vol. 45, no. 11, pp. 3417–3425, 2007.

[77] H. Kimura, “Radar polarization orientation shifts in built-up areas,” *IEEE Geoscience and remote sensing letters*, vol. 5, no. 2, pp. 217–221, 2008.

[78] S. Iwasa and J. Susaki, “Classification of building area using azimuth angle and density indices derived from polarimetric SAR,” in *2011 Joint Urban Remote Sensing Event*, pp. 269–272, IEEE, 2011.

[79] M. Kajimoto and J. Susaki, “Urban density estimation from polarimetric SAR images based on a POA correction method,” *IEEE Journal of Selected Topics in Applied Earth Observations and Remote Sensing*, vol. 6, no. 3, pp. 1418–1429, 2013.

[80] J.-S. Lee and E. Pottier, *Polarimetric radar imaging: from basics to applications*. CRC press, 2009.

[81] J. R. Huynen, “Phenomenological theory of radar targets,” 1970.

[82] R. Barnes, “Roll-invariant decompositions for the polarization covariance matrix,” in *Proceedings of the Polarimetry Technology Workshop, Redstone Arsenal, AL, USA*, vol. 1618, 1988.

[83] W. Holm, “On radar polarization mixed state decomposition theorems,” in *Proc. USA National Radar Conf., April 1988*, 1988.

[84] J. J. van Zyl, “Application of Cloude’s target decomposition theorem to polarimetric imaging radar data,” in *Radar polarimetry*, vol. 1748, pp. 184–191, International Society for Optics and Photonics, 1993.

[85] R. Touzi, “Target scattering decomposition of one-look and multi-look SAR data using a new coherent scattering model: The TSVM,” in *IGARSS 2004. 2004 IEEE International Geoscience and Remote Sensing Symposium*, vol. 4, pp. 2491–2494, IEEE, 2004.

[86] A. Freeman, “Fitting a two-component scattering model to polarimetric SAR data from forests,” *IEEE Transactions on Geoscience and Remote Sensing*, vol. 45, no. 8, pp. 2583–2592, 2007.

[87] A. Freeman and S. L. Durden, “Three-component scattering model to describe polarimetric SAR data,” in *Radar Polarimetry*, vol. 1748, pp. 213–224, International Society for Optics and Photonics, 1993.

[88] Y. Yamaguchi, T. Moriyama, M. Ishido, and H. Yamada, "Four-component scattering model for polarimetric SAR image decomposition," *IEEE Transactions on Geoscience and Remote Sensing*, vol. 43, no. 8, pp. 1699–1706, 2005.

[89] E. Krogager, "New decomposition of the radar target scattering matrix," *Electronics Letters*, vol. 26, no. 18, pp. 1525–1527, 1990.

[90] W. L. Cameron and H. Rais, "Conservative polarimetric scatterers and their role in incorrect extensions of the Cameron decomposition," *IEEE transactions on Geoscience and Remote Sensing*, vol. 44, no. 12, pp. 3506–3516, 2006.

[91] S.-W. Chen, X.-S. Wang, and M. Sato, "Urban damage level mapping based on scattering mechanism investigation using fully polarimetric SAR data for the 3.11 East Japan earthquake," *IEEE Transactions on Geoscience and Remote Sensing*, vol. 54, no. 12, pp. 6919–6929, 2016.

[92] R. Z. Schneider, K. P. Papathanassiou, I. Hajnsek, and A. Moreira, "Polarimetric and interferometric characterization of coherent scatterers in urban areas," *IEEE Transactions on Geoscience and Remote Sensing*, vol. 44, no. 4, pp. 971–984, 2006.

[93] D. Xiang, T. Tang, Y. Ban, Y. Su, and G. Kuang, "Unsupervised polarimetric SAR urban area classification based on model-based decomposition with cross scattering," *ISPRS Journal of Photogrammetry and Remote Sensing*, vol. 116, pp. 86–100, 2016.

[94] E. Dai, Y.-Q. Jin, T. Hamasaki, and M. Sato, "Three-dimensional stereo reconstruction of buildings using polarimetric SAR images acquired in opposite directions," *IEEE Geoscience and Remote Sensing Letters*, vol. 5, no. 2, pp. 236–240, 2008.

[95] E. Michaelsen, U. Soergel, and U. Thoennessen, "Potential of building extraction from multi-aspect high resolution amplitude SAR data," *CMRT05, IAPRS*, pp. 149–154, 2005.

[96] F. Xu and Y.-Q. Jin, "Automatic reconstruction of building objects from multiaspect meter-resolution SAR images," *IEEE Transactions on Geoscience and Remote Sensing*, vol. 45, no. 7, pp. 2336–2353, 2007.

[97] A. Thiele, E. Cadario, K. Schulz, U. Thonnessen, and U. Soergel, "Building recognition from multi-aspect high-resolution InSAR data in urban areas," *IEEE Transactions on Geoscience and Remote Sensing*, vol. 45, no. 11, pp. 3583–3593, 2007.

[98] A. Hooper, D. Bekaert, K. Spaans, and M. Arıkan, “Recent advances in SAR interferometry time series analysis for measuring crustal deformation,” *Tectonophysics*, vol. 514, pp. 1–13, 2012.

[99] S. Gernhardt, N. Adam, M. Eineder, and R. Bamler, “Potential of very high resolution SAR for persistent scatterer interferometry in urban areas,” *Annals of GIS*, vol. 16, no. 2, pp. 103–111, 2010.

[100] I. Parcharidis, S. Kokkalas, I. Fountoulis, and M. Foumelis, “Detection and monitoring of active faults in urban environments: time series interferometry on the cities of Patras and Pyrgos (Peloponnese, Greece),” *Remote Sensing*, vol. 1, no. 4, pp. 676–696, 2009.

[101] A. Ferretti, C. Prati, and F. Rocca, “Permanent scatterers in SAR interferometry,” *IEEE Transactions on geoscience and remote sensing*, vol. 39, no. 1, pp. 8–20, 2001.

[102] R. Lanari, F. Casu, M. Manzo, G. Zeni, P. Berardino, M. Manunta, and A. Pepe, “An overview of the small baseline subset algorithm: A DInSAR technique for surface deformation analysis,” in *Deformation and Gravity Change: Indicators of Isostasy, Tectonics, Volcanism, and Climate Change*, pp. 637–661, Springer, 2007.

[103] X. Zhu, Y. Wang, S. Montazeri, and N. Ge, “A review of ten-year advances of multi-baseline SAR interferometry using TerraSAR-X data,” *Remote Sensing*, vol. 10, no. 9, p. 1374, 2018.

[104] T. Balz, L. Wei, M. Jendryke, D. Perissin, and M. Liao, “Tomosar and PS-InSAR analysis of high-rise buildings in Berlin,” in *2012 IEEE International Geoscience and Remote Sensing Symposium*, pp. 447–450, IEEE, 2012.

[105] X. X. Zhu and R. Bamler, “Superresolving SAR tomography for multidimensional imaging of urban areas: Compressive sensing-based TomoSAR inversion,” *IEEE Signal Processing Magazine*, vol. 31, no. 4, pp. 51–58, 2014.

[106] G. Fornaro, F. Lombardini, and F. Serafino, “Three-dimensional multipass SAR focusing: Experiments with long-term spaceborne data,” *IEEE Transactions on Geoscience and Remote Sensing*, vol. 43, no. 4, pp. 702–714, 2005.

[107] C. Dubois, A. Thiele, and S. Hinz, “Building detection and building parameter retrieval in InSAR phase images,” *ISPRS Journal of Photogrammetry and Remote Sensing*, vol. 114, pp. 228–241, 2016.

[108] U. Stilla, U. Soergel, and U. Thoennessen, “Potential and limits of InSAR data for building reconstruction in built-up areas,” *ISPRS Journal of photogrammetry and remote sensing*, vol. 58, no. 1-2, pp. 113–123, 2003.

[109] L. Denis, F. Tupin, J. Darbon, and M. Sigelle, “Joint regularization of phase and amplitude of InSAR data: Application to 3-D reconstruction,” *IEEE Transactions on Geoscience and Remote Sensing*, vol. 47, no. 11, pp. 3774–3785, 2009.

[110] S. Gernhardt and R. Bamler, “Deformation monitoring of single buildings using meter-resolution SAR data in PSI,” *ISPRS journal of photogrammetry and remote sensing*, vol. 73, pp. 68–79, 2012.

[111] G. Fornaro, F. Lombardini, A. Pauciullo, D. Reale, and F. Viviani, “Tomographic processing of interferometric SAR data: Developments, applications, and future research perspectives,” *IEEE Signal Processing Magazine*, vol. 31, no. 4, pp. 41–50, 2014.

[112] M. Schmitt, “Three-dimensional reconstruction of urban areas by multi-aspect TomoSAR data fusion,” in *2015 Joint Urban Remote Sensing Event (JURSE)*, pp. 1–4, IEEE, 2015.

[113] B. Brisco, F. Ulaby, and M. Dobson, “Spaceborne SAR data for land-cover classification and change detection,” 1983.

[114] M. Gong, H. Yang, and P. Zhang, “Feature learning and change feature classification based on deep learning for ternary change detection in SAR images,” *ISPRS Journal of Photogrammetry and Remote Sensing*, vol. 129, pp. 212–225, 2017.

[115] J.-S. Lee, J.-H. Wen, T. L. Ainsworth, K.-S. Chen, and A. J. Chen, “Improved sigma filter for speckle filtering of SAR imagery,” *IEEE Transactions on Geoscience and Remote Sensing*, vol. 47, no. 1, pp. 202–213, 2008.

[116] C.-A. Deledalle, L. Denis, F. Tupin, A. Reigber, and M. Jäger, “NL-SAR: A unified nonlocal framework for resolution-preserving (Pol)(In) SAR denoising,” *IEEE Transactions on Geoscience and Remote Sensing*, vol. 53, no. 4, pp. 2021–2038, 2014.

[117] E. J. Rignot and J. J. Van Zyl, “Change detection techniques for ERS-1 SAR data,” *IEEE transactions on geoscience and remote sensing*, vol. 31, no. 4, pp. 896–906, 1993.

[118] H. Sofiane and C. Ferdaous, “Comparison of change detection indicators in SAR images,” in *8th European Conference on Synthetic Aperture Radar*, pp. 1–4, VDE, 2010.

[119] Z. Sun and J. Du, “Log-Cumulant Parameter Estimator of Log-Normal Distribution,” in *International Conference on Intelligent Computing*, pp. 668–674, Springer, 2014.

[120] S. Cui, G. Schwarz, and M. Datcu, “A benchmark evaluation of similarity measures for multitemporal SAR image change detection,” *IEEE Journal of Selected Topics in Applied Earth Observations and Remote Sensing*, vol. 9, no. 3, pp. 1101–1118, 2015.

[121] J. M. Joyce, “Kullback-leibler divergence,” *International encyclopedia of statistical science*, pp. 720–722, 2011.

[122] K. Conradsen, A. A. Nielsen, J. Schou, and H. Skriver, “Change detection in polarimetric SAR data and the complex Wishart distribution,” in *IGARSS 2001. Scanning the Present and Resolving the Future. Proceedings. IEEE 2001 International Geoscience and Remote Sensing Symposium (Cat. No. 01CH37217)*, vol. 6, pp. 2628–2630, IEEE, 2001.

[123] F. Chatelain, J.-Y. Tourneret, and J. Inglada, “Change detection in multisensor SAR images using bivariate gamma distributions,” *IEEE Transactions on Image Processing*, vol. 17, no. 3, pp. 249–258, 2008.

[124] V. Alberga, “Similarity measures of remotely sensed multi-sensor images for change detection applications,” *Remote Sensing*, vol. 1, no. 3, pp. 122–143, 2009.

[125] L. Gueguen and M. Datcu, “Mixed information measure: Application to change detection in earth observation,” in *MultiTemp 2009: 5h Int. Workshop Analysis of Multi-temporal Remote Sensing Images*, 2009.

[126] M. Gong, Y. Cao, and Q. Wu, “A neighborhood-based ratio approach for change detection in SAR images,” *IEEE Geoscience and Remote Sensing Letters*, vol. 9, no. 2, pp. 307–311, 2011.

[127] B. Xiong, Q. Chen, Y. Jiang, and G. Kuang, “A threshold selection method using two SAR change detection measures based on the Markov random field model,” *IEEE Geoscience and Remote Sensing Letters*, vol. 9, no. 2, pp. 287–291, 2011.

[128] D. Solarna, G. Moser, and S. Serpico, "A Markovian Approach to Unsupervised Change Detection with Multiresolution and Multimodality SAR Data," *Remote Sensing*, vol. 10, no. 11, p. 1671, 2018.

[129] L. Zhou, G. Cao, Y. Li, and Y. Shang, "Change detection based on conditional random field with region connection constraints in high-resolution remote sensing images," *IEEE Journal of Selected Topics in Applied Earth Observations and Remote Sensing*, vol. 9, no. 8, pp. 3478–3488, 2016.

[130] T. T. Lê, A. M. Atto, E. Trouvé, and J.-M. Nicolas, "Adaptive multitemporal SAR image filtering based on the change detection matrix," *IEEE Geoscience and Remote Sensing Letters*, vol. 11, no. 10, pp. 1826–1830, 2014.

[131] S. Wang, L. Jiao, and S. Yang, "SAR images change detection based on spatial coding and nonlocal similarity pooling," *IEEE Journal of Selected Topics in Applied Earth Observations and Remote Sensing*, vol. 9, no. 8, pp. 3452–3466, 2016.

[132] R. Touati and M. Mignotte, "An energy-based model encoding nonlocal pairwise pixel interactions for multisensor change detection," *IEEE Transactions on Geoscience and Remote Sensing*, vol. 56, no. 2, pp. 1046–1058, 2017.

[133] L. Su, M. Gong, and B. Sun, "Change detection in synthetic aperture radar images based on non-local means with ratio similarity measurement," *International journal of remote sensing*, vol. 35, no. 22, pp. 7673–7690, 2014.

[134] J. Inglada and G. Mercier, "A new statistical similarity measure for change detection in multitemporal SAR images and its extension to multiscale change analysis," *IEEE transactions on geoscience and remote sensing*, vol. 45, no. 5, pp. 1432–1445, 2007.

[135] E. Erten, A. Reigber, L. Ferro-Famil, and O. Hellwich, "A new coherent similarity measure for temporal multichannel scene characterization," *IEEE Transactions on Geoscience and Remote Sensing*, vol. 50, no. 7, pp. 2839–2851, 2011.

[136] V. Akbari, S. N. Anfinsen, A. P. Doulgeris, T. Eltoft, G. Moser, and S. B. Serpico, "Polarimetric SAR change detection with the complex Hotelling–Lawley trace statistic," *IEEE Transactions on Geoscience and Remote Sensing*, vol. 54, no. 7, pp. 3953–3966, 2016.

[137] V. Akbari, S. N. Anfinsen, A. P. Doulgeris, and T. Eltoft, “A change detector for polarimetric SAR data based on the relaxed Wishart distribution,” in *2015 IEEE International Geoscience and Remote Sensing Symposium (IGARSS)*, pp. 3806–3809, IEEE, 2015.

[138] K. Conradsen, A. A. Nielsen, J. Schou, and H. Skriver, “A test statistic in the complex Wishart distribution and its application to change detection in polarimetric SAR data,” *IEEE Transactions on Geoscience and Remote Sensing*, vol. 41, no. 1, pp. 4–19, 2003.

[139] F. Bovolo and L. Bruzzone, “A detail-preserving scale-driven approach to change detection in multitemporal SAR images,” *IEEE Transactions on Geoscience and Remote Sensing*, vol. 43, no. 12, pp. 2963–2972, 2005.

[140] G. Moser and S. B. Serpico, “Unsupervised change detection with very high-resolution SAR images by multiscale analysis and Markov random fields,” in *2010 IEEE International Geoscience and Remote Sensing Symposium*, pp. 3082–3085, IEEE, 2010.

[141] O. Ajadi, F. Meyer, and P. Webley, “Change detection in synthetic aperture radar images using a multiscale-driven approach,” *Remote Sensing*, vol. 8, no. 6, p. 482, 2016.

[142] T. Celik, “Multiscale change detection in multitemporal satellite images,” *IEEE Geoscience and Remote Sensing Letters*, vol. 6, no. 4, pp. 820–824, 2009.

[143] W. Yang, H. Song, X. Huang, X. Xu, and M. Liao, “Change detection in high-resolution SAR images based on Jensen–Shannon divergence and hierarchical Markov model,” *IEEE Journal of Selected Topics in Applied Earth Observations and Remote Sensing*, vol. 7, no. 8, pp. 3318–3327, 2014.

[144] R. Jin, J. Yin, W. Zhou, and J. Yang, “Improved multiscale edge detection method for polarimetric SAR images,” *IEEE Geoscience and Remote Sensing Letters*, vol. 13, no. 8, pp. 1104–1108, 2016.

[145] Y. Bazi, L. Bruzzone, and F. Melgani, “An unsupervised approach based on the generalized Gaussian model to automatic change detection in multitemporal SAR images,” *IEEE Transactions on Geoscience and Remote Sensing*, vol. 43, no. 4, pp. 874–887, 2005.

[146] G. Moser and S. B. Serpico, "Generalized minimum-error thresholding for unsupervised change detection from SAR amplitude imagery," *IEEE Transactions on Geoscience and Remote sensing*, vol. 44, no. 10, pp. 2972–2982, 2006.

[147] C. Bi, H. Wang, and R. Bao, "SAR image change detection using regularized dictionary learning and fuzzy clustering," in *2014 IEEE 3rd International Conference on Cloud Computing and Intelligence Systems*, pp. 327–330, IEEE, 2014.

[148] M. Newey, G. Benitz, and S. Kogon, "A generalized likelihood ratio test for SAR CCD," in *2012 Conference Record of the Forty Sixth Asilomar Conference on Signals, Systems and Computers (ASILOMAR)*, pp. 1727–1730, IEEE, 2012.

[149] M. M. Horta, N. D. Mascarenhas, H. Sportouche, N. Seichepine, F. Tupin, and J.-M. Nicolas, "Change detection in multitemporal HR SAR images: A hypothesis test-based approach," in *2012 IEEE International Geoscience and Remote Sensing Symposium*, pp. 374–377, IEEE, 2012.

[150] J. Barber, "A generalized likelihood ratio test for coherent change detection in polarimetric SAR," *IEEE Geoscience and Remote Sensing Letters*, vol. 12, no. 9, pp. 1873–1877, 2015.

[151] V. T. Vu, N. R. Gomes, M. I. Pettersson, P. Dammert, and H. Hellsten, "Bivariate gamma distribution for wavelength-resolution SAR change detection," *IEEE Transactions on Geoscience and Remote Sensing*, vol. 57, no. 1, pp. 473–481, 2018.

[152] T. Balz, "SAR simulation based change detection with high-resolution SAR images in urban environments," *IAPRS Vol. 35, Part B*, 2004.

[153] J. Tao and S. Auer, "Simulation-based building change detection from multiangle SAR images and digital surface models," *IEEE Journal of Selected Topics in Applied Earth Observations and Remote Sensing*, vol. 9, no. 8, pp. 3777–3791, 2015.

[154] G. Moser and S. B. Serpico, "Unsupervised change detection with high-resolution SAR images by edge-preserving Markov random fields and graph-cuts," in *2012 IEEE International Geoscience and Remote Sensing Symposium*, pp. 1984–1987, IEEE, 2012.

[155] S.-E. Park, Y. Yamaguchi, and D.-j. Kim, "Polarimetric SAR remote sensing of the 2011 Tohoku earthquake using ALOS/PALSAR," *Remote sensing of Environment*, vol. 132, pp. 212–220, 2013.

[156] Y. Dong, Q. Li, A. Dou, and X. Wang, “Extracting damages caused by the 2008 Ms 8.0 Wenchuan earthquake from SAR remote sensing data,” *Journal of Asian Earth Sciences*, vol. 40, no. 4, pp. 907–914, 2011.

[157] M. Matsuoka and F. Yamazaki, “Building damage mapping of the 2003 Bam, Iran, earthquake using Envisat/ASAR intensity imagery,” *Earthquake Spectra*, vol. 21, no. S1, pp. 285–294, 2005.

[158] M. Matsuoka and F. Yamazaki, “Building damage detection using satellite SAR intensity images for the 2003 Algeria and Iran earthquakes,” in *IGARSS 2004. 2004 IEEE International Geoscience and Remote Sensing Symposium*, vol. 2, pp. 1099–1102, IEEE, 2004.

[159] Y. Bai, B. Adriano, E. Mas, and S. Koshimura, “Building Damage Assessment in the 2015 Gorkha, Nepal, Earthquake Using Only Post-Event Dual Polarization Synthetic Aperture Radar Imagery,” *Earthquake Spectra*, vol. 33, no. S1, pp. S185–S195, 2017.

[160] M. Chini, R. Pelich, L. Pulvirenti, N. Pierdicca, R. Hostache, and P. Matgen, “Sentinel-1 insar coherence to detect floodwater in urban areas: Houston and hurricane harvey as a test case,” *Remote Sensing*, vol. 11, no. 2, p. 107, 2019.

[161] P. Washaya, T. Balz, and B. Mohamadi, “Coherence change-detection with sentinel-1 for natural and anthropogenic disaster monitoring in urban areas,” *Remote Sensing*, vol. 10, no. 7, p. 1026, 2018.

[162] S. Schlaffer, P. Matgen, M. Hollaus, and W. Wagner, “Flood detection from multi-temporal SAR data using harmonic analysis and change detection,” *International Journal of Applied Earth Observation and Geoinformation*, vol. 38, pp. 15–24, 2015.

[163] S. Frolking, T. Milliman, K. C. Seto, and M. A. Friedl, “A global fingerprint of macro-scale changes in urban structure from 1999 to 2009,” *Environmental Research Letters*, vol. 8, no. 2, p. 024004, 2013.

[164] S. Nghiem, D. Balk, E. Rodriguez, G. Neumann, A. Sorichetta, C. Small, and C. Elvidge, “Observations of urban and suburban environments with global satellite scatterometer data,” *ISPRS Journal of Photogrammetry and Remote Sensing*, vol. 64, no. 4, pp. 367–380, 2009.

[165] L. H. Nguyen, S. V. Nghiem, and G. M. Henebry, “Expansion of major urban areas in the US Great Plains from 2000 to 2009 using satellite scatterometer data,” *Remote Sensing of Environment*, vol. 204, pp. 524–533, 2018.

[166] Y. Ban, A. Jacob, and P. Gamba, “Spaceborne SAR data for global urban mapping at 30 m resolution using a robust urban extractor,” *ISPRS Journal of Photogrammetry and Remote Sensing*, vol. 103, pp. 28–37, 2015.

[167] P. Gamba and G. Lisini, “Fast and efficient urban extent extraction using ASAR wide swath mode data,” *IEEE Journal of Selected Topics in Applied Earth Observations and Remote Sensing*, vol. 6, no. 5, pp. 2184–2195, 2013.

[168] L. Bruzzone and D. F. Prieto, “Automatic analysis of the difference image for unsupervised change detection,” *IEEE Transactions on Geoscience and Remote sensing*, vol. 38, no. 3, pp. 1171–1182, 2000.

[169] R. Achanta, A. Shaji, K. Smith, A. Lucchi, P. Fua, and S. Süsstrunk, “Slic superpixels compared to state-of-the-art superpixel methods,” *IEEE transactions on pattern analysis and machine intelligence*, vol. 34, no. 11, pp. 2274–2282, 2012.

[170] X. Huang, W. Yang, G.-S. Xia, and M. Liao, “Superpixel-based change detection in high resolution sar images using region covariance features,” in *2015 8th International Workshop on the Analysis of Multitemporal Remote Sensing Images (Multi-Temp)*, pp. 1–4, IEEE, 2015.

[171] L. Xie, H. Zhang, C. Wang, M. Liu, and B. Zhang, “Superpixel-based polsar images change detection,” in *2015 IEEE 5th Asia-Pacific Conference on Synthetic Aperture Radar (APSAR)*, pp. 792–796, IEEE, 2015.

[172] R. Achanta, A. Shaji, K. Smith, A. Lucchi, P. Fua, and S. Süsstrunk, “SLIC superpixels compared to state-of-the-art superpixel methods,” *IEEE transactions on pattern analysis and machine intelligence*, vol. 34, no. 11, pp. 2274–2282, 2012.

[173] R. Achanta, A. Shaji, K. Smith, A. Lucchi, P. Fua, and S. Süsstrunk, “Slic superpixels,” 2010.

[174] X. Huang, W. Yang, G.-S. Xia, and M. Liao, “Superpixel-based change detection in high resolution SAR images using region covariance features,” in *Analysis of Multitemporal Remote Sensing Images (Multi-Temp), 2015 8th International Workshop on the*, pp. 1–4, IEEE, 2015.

[175] J.-S. Lee, M. R. Grunes, T. L. Ainsworth, L.-J. Du, D. L. Schuler, and S. R. Cloude, “Unsupervised classification using polarimetric decomposition and the complex Wishart classifier,” *IEEE Transactions on Geoscience and Remote Sensing*, vol. 37, no. 5, pp. 2249–2258, 1999.

[176] Y. Bazi, L. Bruzzone, and F. Melgani, “An unsupervised approach based on the generalized Gaussian model to automatic change detection in multitemporal SAR images,” *IEEE Transactions on Geoscience and Remote Sensing*, vol. 43, no. 4, pp. 874–887, 2005.

[177] A. S. Yommy, R. Liu, and S. Wu, “SAR image despeckling using refined Lee filter,” in *2015 7th International Conference on Intelligent Human-Machine Systems and Cybernetics*, vol. 2, pp. 260–265, IEEE, 2015.

[178] S. Cloude, “The dual polarization entropy/alpha decomposition: A PALSAR case study,” in *Science and Applications of SAR Polarimetry and Polarimetric Interferometry*, vol. 644, 2007.

[179] M. Che, P. Du, and P. Gamba, “2-and 3-d urban change detection with quad-polsar data,” *IEEE Geoscience and Remote Sensing Letters*, vol. 15, no. 1, pp. 68–72, 2017.

[180] X. Huang, H. Liu, and L. Zhang, “Spatiotemporal detection and analysis of urban villages in mega city regions of China using high-resolution remotely sensed imagery,” *IEEE Transactions on Geoscience and Remote Sensing*, vol. 53, no. 7, pp. 3639–3657, 2015.

[181] B. Huang, C. Xie, and R. Tay, “Support vector machines for urban growth modeling,” *Geoinformatica*, vol. 14, no. 1, p. 83, 2010.

[182] Q. Zhang and K. C. Seto, “Mapping urbanization dynamics at regional and global scales using multi-temporal DMSP/OLS nighttime light data,” *Remote Sensing of Environment*, vol. 115, no. 9, pp. 2320–2329, 2011.

[183] S. Kaya, “Multitemporal analysis of rapid urban growth in Istanbul using remotely sensed data,” *Environmental Engineering Science*, vol. 24, no. 2, pp. 228–233, 2007.

[184] C. G. O’Hara, J. S. King, J. H. Cartwright, and R. L. King, “Multitemporal land use and land cover classification of urbanized areas within sensitive coastal environments,” *IEEE Transactions on Geoscience and Remote Sensing*, vol. 41, no. 9, pp. 2005–2014, 2003.

[185] H. Taubenböck, M. Wegmann, A. Roth, H. Mehl, and S. Dech, “Urbanization in India–Spatiotemporal analysis using remote sensing data,” *Computers, environment and urban systems*, vol. 33, no. 3, pp. 179–188, 2009.

[186] G. Lisini, A. Salentinig, P. Du, and P. Gamba, “SAR-based urban extents extraction: from ENVISAT to Sentinel-1,” *IEEE Journal of Selected Topics in Applied Earth Observations and Remote Sensing*, vol. 11, no. 8, pp. 2683–2691, 2017.

[187] S. Usai and R. Klees, “SAR interferometry on a very long time scale: a study of the interferometric characteristics of man-made features,” *IEEE Transactions on Geoscience and Remote Sensing*, vol. 37, no. 4, pp. 2118–2123, 1999.

[188] G. A. Arciniegas, W. Bijker, N. Kerle, and V. A. Tolpekin, “Coherence-and amplitude-based analysis of seismogenic damage in Bam, Iran, using ENVISAT ASAR data,” *IEEE Transactions on Geoscience and Remote Sensing*, vol. 45, no. 6, pp. 1571–1581, 2007.

[189] H. A. Zebker and J. Villasenor, “Decorrelation in interferometric radar echoes,” *IEEE Transactions on geoscience and remote sensing*, vol. 30, no. 5, pp. 950–959, 1992.

[190] A. Zimek, E. Schubert, and H.-P. Kriegel, “A survey on unsupervised outlier detection in high-dimensional numerical data,” *Statistical Analysis and Data Mining: The ASA Data Science Journal*, vol. 5, no. 5, pp. 363–387, 2012.

[191] S. Ma, X. Li, and Y. Cai, “Delimiting the urban growth boundaries with a modified ant colony optimization model,” *Computers, Environment and Urban Systems*, vol. 62, pp. 146–155, 2017.

[192] F. Canaslan and A. Ustun, “Impact of perpendicular and temporal baseline characteristics on InSAR coherence maps,” in *Proc. FIG Working Week*, 2012.

[193] L. Li, D. Lu, and W. Kuang, “Examining urban impervious surface distribution and its dynamic change in Hangzhou metropolis,” *Remote Sensing*, vol. 8, no. 3, p. 265, 2016.

[194] M. Melchiorri, A. Florczyk, S. Freire, M. Schiavina, M. Pesaresi, and T. Kemper, “Unveiling 25 years of planetary urbanization with remote sensing: Perspectives from the global human settlement layer,” *Remote Sensing*, vol. 10, no. 5, p. 768, 2018.

[195] C. Corbane, M. Pesaresi, P. Politis, V. Syrris, A. J. Florczyk, P. Soille, L. Maffenini, A. Burger, V. Vasilev, D. Rodriguez, *et al.*, “Big earth data analytics on sentinel-1 and landsat imagery in support to global human settlements mapping,” *Big Earth Data*, vol. 1, no. 1-2, pp. 118–144, 2017.

[196] T. Esch, W. Heldens, A. Hirner, M. Keil, M. Marconcini, A. Roth, J. Zeidler, S. Dech, and E. Strano, “Breaking new ground in mapping human settlements from space–the global urban footprint,” *ISPRS Journal of Photogrammetry and Remote Sensing*, vol. 134, pp. 30–42, 2017.

[197] Q. Zhang and K. C. Seto, “Mapping urbanization dynamics at regional and global scales using multi-temporal DMSP/OLS nighttime light data,” *Remote Sensing of Environment*, vol. 115, no. 9, pp. 2320–2329, 2011.

[198] G. C. Iannelli and P. Gamba, “Jointly exploiting sentinel-1 and sentinel-2 for urban mapping,” in *IGARSS 2018-2018 IEEE International Geoscience and Remote Sensing Symposium*, pp. 8209–8212, IEEE, 2018.

[199] S. Nghiem, D. Balk, E. Rodriguez, G. Neumann, A. Sorichetta, C. Small, and C. Elvidge, “Observations of urban and suburban environments with global satellite scatterometer data,” *ISPRS Journal of Photogrammetry and Remote Sensing*, vol. 64, no. 4, pp. 367–380, 2009.

[200] L. H. Nguyen, S. V. Nghiem, and G. M. Henebry, “Expansion of major urban areas in the US Great Plains from 2000 to 2009 using satellite scatterometer data,” *Remote Sensing of Environment*, vol. 204, pp. 524–533, 2018.

[201] S. Frolking, T. Milliman, K. C. Seto, and M. A. Friedl, “A global fingerprint of macro-scale changes in urban structure from 1999 to 2009,” *Environmental Research Letters*, vol. 8, no. 2, p. 024004, 2013.

[202] D. L. Balk, S. V. Nghiem, B. R. Jones, Z. Liu, and G. Dunn, “Up and out: A multifaceted approach to characterizing urbanization in Greater Saigon, 2000–2009,” *Landscape and Urban Planning*, vol. 187, pp. 199–209, 2019.

[203] M. Che and P. Gamba, “Possibilities and limits of urban change detection using polarimetric SAR data,” in *IGARSS 2018-2018 IEEE International Geoscience and Remote Sensing Symposium*, pp. 6079–6082, IEEE, 2018.

[204] G. Lisini, A. Salentinig, P. Du, and P. Gamba, “SAR-based urban extents extraction: from ENVISAT to Sentinel-1,” *IEEE Journal of Selected Topics in Applied Earth Observations and Remote Sensing*, vol. 11, no. 8, pp. 2683–2691, 2017.

[205] EUMETSAT, “ASCAT GDS Level 1 Sigma0 at Full Sensor Resolution,” 2009.

[206] D. Lu, L. Li, G. Li, P. Fan, Z. Ouyang, and E. Moran, “Examining spatial patterns of urban distribution and impacts of physical conditions on urbanization in coastal and inland metropoles,” *Remote Sensing*, vol. 10, no. 7, p. 1101, 2018.

[207] S. Wang, J. Xing, B. Zhao, C. Jang, and J. Hao, “Effectiveness of national air pollution control policies on the air quality in metropolitan areas of China,” *Journal of Environmental Sciences*, vol. 26, no. 1, pp. 13–22, 2014.

[208] Y. Wu, S. Li, and S. Yu, “Monitoring urban expansion and its effects on land use and land cover changes in Guangzhou city, China,” *Environmental monitoring and assessment*, vol. 188, no. 1, p. 54, 2016.

[209] M. Che and P. Gamba, “Intra-urban change analysis using Sentinel-1 and Nighttime Light Data,” *IEEE Journal of Selected Topics in Applied Earth Observations and Remote Sensing*, vol. 12, no. 4, pp. 1134–1142, 2019.

[210] J. Rutkowski, M. J. Canty, and A. A. Nielsen, “Site monitoring with sentinel-1 dual polarization sar imagery using google earth engine,” *Journal of Nuclear Materials Management*, vol. 46, no. 3, pp. 48–59, 2018.

[211] F. Pernkopf and D. Bouchaffra, “Genetic-based EM algorithm for learning Gaussian mixture models,” *IEEE Transactions on Pattern Analysis and Machine Intelligence*, vol. 27, no. 8, pp. 1344–1348, 2005.

[212] D. M. Blei, A. Kucukelbir, and J. D. McAuliffe, “Variational inference: A review for statisticians,” *Journal of the American Statistical Association*, vol. 112, no. 518, pp. 859–877, 2017.

[213] B. Wang and J. Zheng, “Research on the evaluation of land intensive utilization in megalopolis of China,” *J. Univ. Sci. Technol. Beijing (Soc. Sci. Ed.)*, vol. 22, pp. 24–28, 2006.

[214] Wikipedia contributors, “Milan metropolitan area — Wikipedia, the free encyclopedia,” 2019. [Online; accessed 10-September-2019].

[215] Wikipedia contributors, “Economy of nigeria — Wikipedia, the free encyclopedia,” 2019. [Online; accessed 10-September-2019].